Dublin City University
School of Physical Sciences

Surface and interface characterization studies of germanium and indium arsenide substrates

Rajesh Kumar Chellappan

Doctor of Philosophy

July 2013

Supervised by Professor Greg Hughes

Dedications and Acknowledgements

First and foremost I would like to thank my supervisor Prof. Greg Hughes for his guidance, support and encouragement throughout my time in DCU. I can't thank him enough for the research opportunities provided for me during the course of study.

A special thanks to Dr. Paul Hurley (Tyndall National Institute) and Prof. Navakanta Bhat (Indian Institute of Science) for their help and guidance on this study and allowing me to use their lab facilities.

Many thanks to my group at DCU: Lalit, Kumar, Justin, Anthony, Lee and Paddy for their extremely helpful discussions. I owe a big thanks to our collaborators whom I worked during this study: Dr. David McNeill (QUB), Suman Gupta (IISc) and Zheshen Li (AU), and Pat Wogan for all his technical help at DCU.

This acknowledgement would be incomplete without thanking my lovable family.

Last but not least my countless thanks to "GOD". I dedicate this study to the lotus feet of Ayya Vaikundar who blessed me with the courage and power to complete it.

Declaration

I hereby certify that this material, which I now submit for assessment on the programme of study leading to the award of doctor of Philosophy is entirely my own work, that I have exercised reasonable care to ensure that the work is original, and does not to the best of my knowledge breach any law of copyright, and has not been taken from the work of others save and to the extent that such work has been cited and acknowledged within the text of my work.

Signed: _____ (Candidate)

ID No.: 10102434

Date: _____

Abstract

This thesis investigates the surface cleaning procedures, passivation and interface formation following high-κ deposition on Ge(100) and InAs(100) substrates using soft x-ray photoemission spectroscopy (SXPS). A comparison study between the thermal cleaning of the native oxide covered InAs(100) surface and atomic hydrogen cleaned surface indicated that thermal annealing to 450^{o}C is not sufficient to produce an oxide and carbon free surface whereas atomic hydrogen cleaning at 360^{o}C resulted in the removal of both native oxides and surface carbon contamination to produce a clean In rich surface.

The selenium passivation of this atomically clean InAs showed evidence of arsenic replacement in the near surface region. Subsequent MgO deposition resulted in interface oxidation indicating that the selenium treatment has not been successful in passivating the InAs surface. In a similar study on the atomically clean Ge(100) surface, interface oxide formation was observed following MgO deposition while on the selenium passivated surface, no interface oxides were observed.

Wet chemical sulphur treatments of both the Ge(100) and InAs(100) surfaces showed that the sulphur passivation layer was stable up to 500^{o}C and 600^{o}C, respectively. Subsequent studies involving the atomic layer deposition of ultra thin high-κ dielectric layers on these surfaces showed that thermal annealing was effective at reducing the interfacial oxides without altering the dielectric material's stoichiometry.

The high pressure post oxygen annealing treatment of Al_2O_3/Ge structures were chemically characterised using SXPS and x-ray photoelectron spectroscopy (XPS), and electrically tested

after fabricating MOS capacitor structures. The density of interface states (D_{it}) was significantly decreased when the Ge(100) surface was subjected to wet chemical based sulphur treatments prior to dielectric deposition. Finally, the concentrations of germanium sulphide formation on the Ge(100) surface achieved by diluting ammonium sulphide in various alcohols was studied using SXPS and the electrical impact on the CV measurements of MOS structures on these surfaces was investigated.

Publications arising from this work

Synchrotron radiation photoemission study of the thermal annealing and atomic hydrogen cleaning of native oxide covered InAs(1 0 0) surfaces

Rajesh Kumar Chellappan, Zheshen Li and Greg Hughes
Applied Surface Science Volume 276 Pages 609–612 (2013).

High-resolution photoemission comparison study of interface formation between MgO and the atomically clean and Se-passivated Ge(100) surfaces

Rajesh Kumar Chellappan and Greg Hughes
Phyisca Status Solidi Rapid Research Letters 7 No.8 590-592 (2013).

High resolution photoemission study of interface formation between MgO and the selenium passivated InAs (100) surface

Rajesh Kumar Chellappan, Zheshen Li and Greg Hughes
Applied Surface Science (Accepted)

Optimisation and scaling of interfacial GeO_2 layers for high-κ gate stacks on germanium and extraction of dielectric constant of GeO_2

S.N.A.Murad, P.T.Baine, D.W.McNeill, S.J.N.Mitchell, B.M.Armstrong, M.Modreanu, G.Hughes and **R.K.Chellappan** Solid-State Electronics Volume 78, Pages 136–140(2012)

Soft x-ray photoemission study of the thermal stability of the Al_2O_3/Ge (100) interface as a function of surface preparation

Rajesh Kumar Chellappan, Durga Rao Gajula, David Mc Neill and Greg Hughes
Journal of Applied Physics (Accepted)

High temperature thermal stability of the HfO_2/Ge (100) interface as a function of surface preparation studied by synchrotron radiation core level photoemission

Rajesh Kumar Chellappan, Durga Rao Gajula, David Mc Neill and Greg Hughes
Applied Surface Science (In review)

High temperature thermal stability study of 1nm Al_2O_3 deposited on InAs surfaces investigated by synchrotron radiation based photoemission spectroscopy

Rajesh Kumar Chellappan, Durga Rao Gajula, David Mc Neill and Greg Hughes
Journal of Applied Physics (In review)

Electrical and chemical properties of Al_2O_3/S/Ge: A systematic study of sulphur passivation with different pre-cleaning methods

Rajesh Kumar Chellappan, Suman Gupta, Piyush Jaiswal, Navakanta Bhat, S. A. Shivashankar, Greg Hughes (Manuscript in preparation)

Investigation of alcohol based sulphur passivation treatments on the electrical properties of Germanium MOS capacitors

Rajesh Kumar Chellappan, Suman Gupta, Piyush Jaiswal, Navakanta Bhat, S. A. Shivashankar, Greg Hughes (Manuscript in preparation)

Conferences

R. K. Chellappan and G. Hughes "Interface studies of High-k dielectric growth on Ge (100) surfaces" Intel European Research & Innovation Conference 2011, Lexilip, Ireland (Oct 12-14,2011)**.**

Rajesh Kumar Chellappan and Greg Hughes "High resolution photoemission comparison study of interface formation between MgO and the atomically clean and selenium passivated Ge (100) surfaces" 42nd IEEE Semiconductor Interface Specialist conference (SISC), Arlington,VA, USA (Dec 1-3,2011).

S. N. Ali Murad, D. W. McNeill, S. J. N. Mitchell, B. M. Armstrong, M. Modreanu, G. Hughes, and **R.K.Chellappan** "Optimisation and scaling of interfacial GeO_2 layers for high-k gate stacks on germanium" 13th International conference on the formation of semiconductor interfaces (ICFSI), Prague, Czeck republic (July 3-8,2011).

S. N. Ali Murad, D. W. McNeill, S. J. N. Mitchell, B. M. Armstrong, M. Modreanu,, G. Hughes, and **R.K.Chellappan** "Optimisation and scaling of interfacial GeO_2 layers for high-κ gate stacks on germanium and extraction of dielectric constant of GeO_2" International Semiconductor Device Research Symposium (ISDRS), University of Maryland, MD,USA(Dec 7-9,2011)**.**

Rajesh Kumar Chellappan and Greg Hughes "Photoemission studies of interface formation between high-k dielectric materials and high mobility semiconductor substrates for future device integration" BOC poster competition 2013, DCU.

Table of Contents

Table of figures

1 Introduction

This chapter introduces the main ideas behind the introduction of high-κ gate dielectric materials and high mobility substrates for the future development of complementary metal oxide semiconductor (CMOS) technology. It also provides a short literature review of surface preparation procedures suitable for the semiconductor substrates investigated in this thesis, germanium and indium arsenide, and concludes with an outline of the thesis layout.

1.1 Device scaling-Moore's law

For the past few decades, silicon and silicon dioxide have been the leading substrate and dielectric material for (CMOS) device fabrication which has underpinned the development of computer technology. The ability to accurately control the silicon doping density and form high quality electrical interfaces between silicon and silicon dioxide are the main reasons for the development of silicon based electronic devices which dominate the microelectronics industry.

The metal oxide semiconductor field effect transistor (MOSFET) is the basic building block for microprocessor fabrication in that it allows logic operations to be carried out in an efficient manner. Increasing device performances while decreasing size is the key driver to meet the continuous demands such as higher packing density, lower power dissipation and higher circuit speed set by International Technology Roadmap for semiconductors (ITRS) [1]. In 1960's, Gordon Moore co-founder of Intel, predicted that the number of transistors in integrated circuits would double every two years [2]. The increasing trend of FET density as a function of year of fabrication is shown in figure 1.1. Due to downscaling, a MOSFET made of silicon and silicon dioxide materials were scale down to 45 nm gate length in 2008 from its original 10 μm gate length in 1971 [2]. Ideally further device scaling can be achieved

by continuing to reduce device dimensions and operating voltages while maintaining constant a electric field across the gate dielectric.

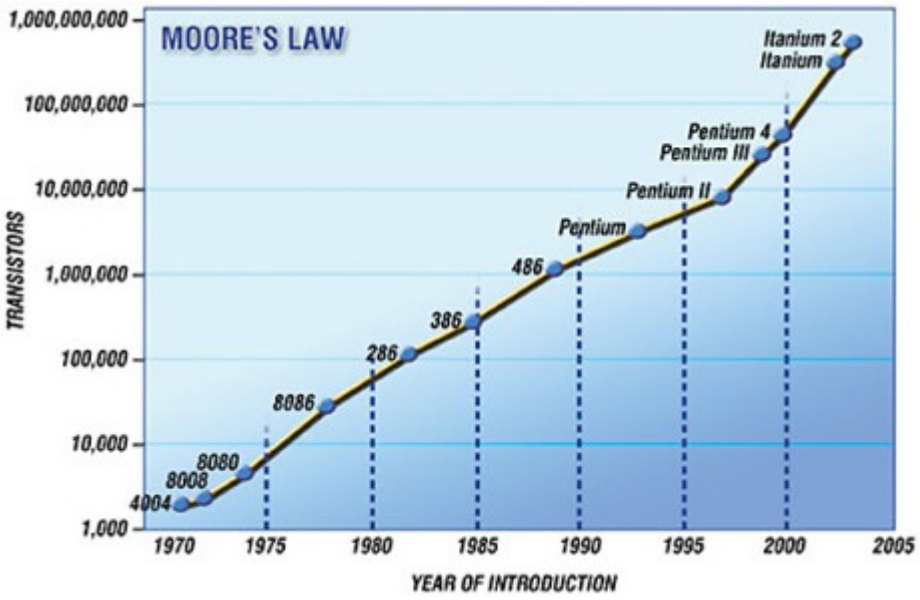

Figure 1.1: Number of transistors integrated per chip versus year of introduction (Intel).

However, in practice, the device dimensions and operating voltages cannot be continually reduced due to fundamental limits dictated by quantum mechanics.

1.2 Why high-κ material?

The continuous scaling has thinned the SiO_2 gate dielectric layer to 1.1 nm (for 0.1 μm technology node). At this thickness, direct electron tunnelling across the gate dielectric is the main concern as it contributes to a dramatic increase in junction leakage current which degrades the electrical performance [3]. Replacement of SiO_2 with a higher permittivity (high-κ) material allows an increase in the physical thickness of oxide to reduce the gate leakage current while maintaining or decreasing the oxide capacitance (C_{ox}). The C_{ox} is defined as

$$C_{ox} = \frac{\varepsilon_o}{t_{ox}} \kappa . A \qquad 1.1$$

Where ε_o is the permittivity of free space (8.854×10^{-12} F/m), κ is the permittivity of the gate dielectric material (SiO_2 ~ 3.9), A is the area of capacitor and t_{ox} is the thickness of the dielectric layer. C_{ox} of a particular gate dielectric material is proportional to the ratio of dielectric constant to physical thickness of the oxide, therefore as t_{ox} decreases, the capacitance increases.

The oxide capacitance can be maintained by using a material whose dielectric constant is higher than SiO_2 while increasing the thickness of the dielectric layer thereby reducing the tunnel current. Materials whose dielectric constant is higher than SiO_2 are called high-κ materials. The equation 1.1 can be rewritten in terms of equivalent oxide thickness (EOT) or theoretical thickness of SiO_2 as

$$t_{ox} = \text{EOT} = \left({}^{3.9}/_{K}\right)t_{HiK} \qquad 1.2$$

Where t_{HiK} and κ are the physical thickness and the dielectric constant of the high-κ dielectric layer, respectively. The schematic representation of equation 1.2 is shown in figure 1.2, which illustrates that the introduction of a high-κ layer increases the physical thickness of the dielectric while maintaining the same capacitance.

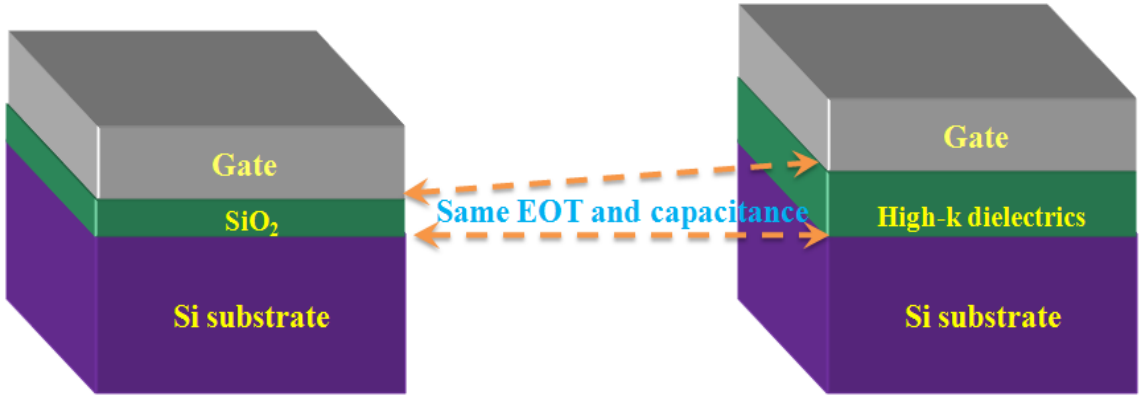

Figure 1.2: A schematic showing replacement of thin SiO_2 with thicker high-κ dielectrics results same EOT and capacitance.

1.3 Guidelines for choosing alternate high-κ dielectrics

An ideal high-kappa dielectric material would conform with the requirements listed by Robertson [4] for the continued development of MOSFET device performance with future scaling.

1. The κ value must be high enough so that gate dielectric can be scaled for reasonable number of device generations.
2. The oxide and substrate interface must be thermodynamically stable so that interfacial layer formation can be avoided. For example, high temperature vacuum anneal of Al_2O_3/III-V structure results in the formation of indium hydroxide at the interface which can degrade the electrical properties [5].
3. The introduction of a new chemical layer at the interface by the interaction of oxide and substrate material could increase the EOT and might degrade the electrical properties.
4. The dielectric material must be kinetically stable and compatible with the processing temperatures up to 1000^{o}C for 5 mins. The thermal dopant activation of source/drain implantations requires processing at high temperatures hence the dielectric properties must not be affected during at these processing temperatures.
5. The dielectric material must have energy band offsets with the substrate of more than 1 eV to inhibit carrier injection. Figure 1.3 shows that band gap of dielectric materials and the dielectric constant kappa are inversely proportional [6].
6. The dielectric must form a good electrical interface with the substrate with a low density of defect states. For example, elemental arsenic present at the Al_2O_3/III-V interface gives rise to defect states in the band gap of semiconductor which pin the Fermi level [7].

7. The dielectric must have few electrically active bulk defects. These defects can be formed due to excess or deficiency of oxygen or other impurities. The presence of these defects could trap charge and shift the threshold voltage (operating voltage) of a device. The mobility degradation and breakdown of oxide are also possible due to the presence of these trapped charges.

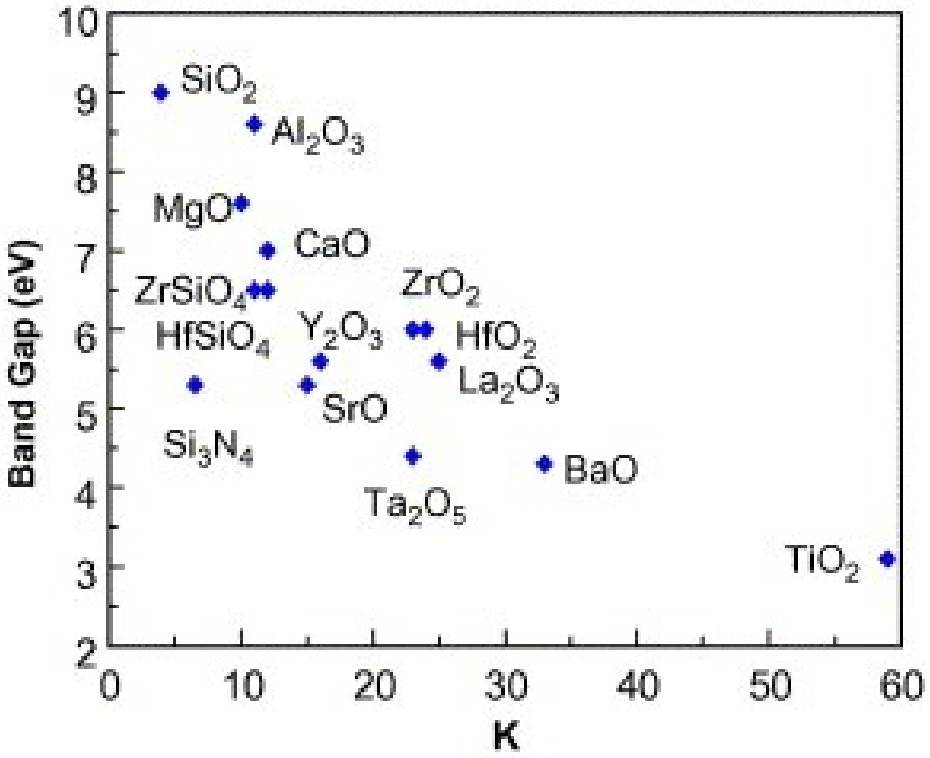

Figure 1.3: Band gap of various dielectric materials and its dielectric constant [4].

1.4 Integration of high-κ dielectrics and high mobility substrates for Si CMOS

In 2005, IBM researchers proposed the idea of integrating high mobility and high-κ materials, into the development of future generation of Si CMOS technologies as shown in figure 1.4 [8].

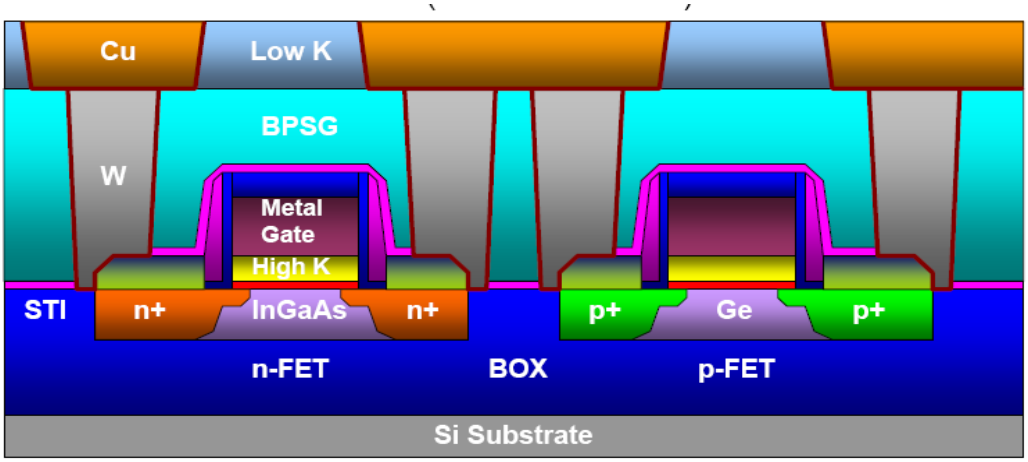

Figure 1.4: Integration of high mobility substrates for CMOS devices [8].

Germanium and III-V materials (especially InGaAs) were proposed as suitable high mobility candidates for PMOS and NMOS devices because of their higher hole and electron mobility than silicon. These materials have been previously investigated as to their suitability for device integration in the in the 1940's when the first bipolar junction transistor was fabricated using germanium [9] and in the 1960's early attempts to develop III-V substrate based MOSFET [10] were initiated. However the poor quality of the native oxides which form on these substrates displayed higher interfacial defect state densities than SiO_2/Si interface. In addition, the thermal stability and good insulating properties of SiO_2 are significantly better than for the native oxides on germanium and III-V substrates. The integration of high-κ dielectric materials onto these materials would enable further scaling of CMOS technology and has therefore been the subject of extensive investigation. However problems associated with the interface property of high-κ/Ge and III-V substrates are still a major concern. The surface cleaning and passivation of these high mobility materials has become a much studied research field in attempts to avoid an undesirable growth of interfacial oxides prior to or during high-κ deposition.

1.4.1 Surface preparation of Germanium and III-V surfaces

As mentioned previously, the poor electrical quality of the native oxides on III-V and germanium surfaces makes difficult to realise the advantages of higher electron and hole mobility than silicon [11] shown in table 1.1.

Material / Property	Si	Ge	GaAs	InAs	InGaAs
Electron mobility	1600	3900	9200	40000	7000
Hole mobility	430	1900	400	500	250
Bandgap (eV)	1.12	0.66	1.424	0.36	0.75

Table 1.1: Material property of various semiconductors [11].

Therefore strategies for the preparation of clean surfaces and controlling interface formation to limit interface defect state densities are critically important for device applications such as metal oxide semiconductor (MOS) structures which is the fundamental building block of the field effect transistor (FET). Ideally, a common surface cleaning treatment needs to be developed for both germanium and III-V substrates in an attempt to simplify the fabrication process of CMOS devices. However, the chemical reactivity of the native oxides which form on both surfaces are different. For example germanium oxide (GeO_2) is water soluble whereas the native oxides in InAs are not. Thus finding a common solution for both substrates is one of the challenges faced by the semiconductor industry. There are several surface treatments reported for the preparation of oxide free germanium and III-V surfaces [12-14]. However preserving the elemental stoichiometry during the cleaning process is

particularly important for III-V substrates. The atomic hydrogen treatment on III-V surfaces is reported to produce clean surfaces however prolonged exposure results in indium loss [15, 16]. In-situ treatments like argon ion bombardment are reported to result in oxide free surfaces however this treatment can damage the surface [13,14]. The wet chemical cleaning procedures followed by annealing treatments have also been reported to produce clean surfaces [17-19]. The subsequent necessary step following successful surface cleaning is the passivation of the surface prior to dielectric deposition in order to control interface oxidation.

1.4.2 Why surface passivation?

The surface passivation of semiconductors aims to achieve two objectives, chemical and electronic stability of the semiconductor surfaces. The chemical passivation is designed to make the cleaned surface inert towards both ambient contamination, mainly oxygen and control interface formation with a high-κ layer. Electronic passivation aims to limit the density of interface state formation between the semiconductor and the dielectric as these states impact on the ability to move the Fermi level across the gap which has direct implications for FET operation.

1.4.3 Passivation of Germanium and III-V surfaces

When clean germanium and III-V surfaces are exposed to air, native oxides readily form within a few minutes. The chemical passivation of germanium and III-V surfaces using methods like chalcogenide treatments, nitridation and halogenation have been reported to inhibit ambient oxidation upon air exposure. Therefore, these treatments have been utilized in controlling interface formation between the substrates and high-k layers and have shown encouraging results. The thermal stability of these passivation layers requires investigation as, particularly for III-V semiconductors, thermal annealing at the temperatures used in device fabrication can impact on the stoichiometry of the semiconductor.

1.4.3.1 Chalcogenide treatments

The elements occupying the 16th column of the periodic table are called chalcogenides and these elements have been widely used in the passivation of semiconductor surface. In-situ treatment using sulphur, selenium and tellurium elements have been reported to passivate germanium and III-V surfaces [19,22-26]. Sulphur and selenium passivation of III-V surfaces are reported to result in arsenic replacement in the near surface region [24,25]. However, the passivation of germanium using elemental sulphur was reported to create defect states in the band gap which is undesirable for MOS devices [27]. Several other approaches have been studied to achieve sulphur passivation on these surfaces to prepare high quality dielectric semiconductor interfaces [20,28,29]. Previous studies report that the wet chemical ammonium sulphide based sulphur treatment is suitable for both germanium and III-V surfaces [30,31]. This treatment is reported to be successful at removing native oxides from both substrates. In addition, the sulphur passivated germanium surface was reported to be more resistant to ambient oxidation than chlorine or hydrogen terminated germanium surfaces [32]. Thathachary et al [33] reported the unpinning of the Fermi level using a sulphur passivation treatment on metal-Ge contacts. Recent studies have shown the possibility of achieving 1nm EOT using sulphur passivated germanium MOS stacks [34]. Selenium, from the same group as sulphur, is also expected to show similar promising chemical and electronic properties. Previous studies suggested that the selenium passivated germanium surface effectively suppresses germanium oxide formation during molecular oxygen treatment and has a lower interfacial defect states density than unpassivated germanium MOS structures [35]. Selenium passivation of III-V surfaces was achieved by using sodium selenide in ammonium hydroxide [36]. As a result of this treatment, three chemical states of selenium were formed on the surface namely, selenates (Se^{4+}) elemental selenium (Se^{0}) and selenides (Se^{2-}). However sodium selenide solution treatment also results

in complete removal of native oxides and coverage of selenium in the form of selenides (As_2Se_3) on III-V surface [37]. Alternate way of removing oxide and selenium termination on III-V surface was also reported using wet chemical based Se/NH_4OH treatments [38].

1.4.3.2 Nitridation

Nitridation of germanium and III-V surfaces have also been reported to successfully suppress native oxide formation [39,40]. A wide range of nitridation approaches using plasma nitridation, wet chemical hydrazine solution [41], thermal NH_3 treatment [42-45] and exposure to $N_2H_2(CH_3)_2$ vapour [46] have been reported to form germanium nitride and III-V nitride on germanium and III-V surfaces. Previously GeO_xN_y and Ge_3N_4 gate dielectrics on germanium surfaces were tested however these dielectrics were not suitable to achieve ultimate scaling due to their low-κ values [47,48]. Hence these dielectric materials are used as a thin passivation layers between high-κ dielectrics and germanium substrates [49]. Nitridation of the germanium surface using gas mixtures such as $H_2/N_2/Ar$ and $H_2/N_2/NH_3/Ar$ allows the tuning of the atomic concentration of N which is integrated into the GeO_xN_y layers [50,51]. Recent study suggests the similar nitridation treatment improves the electrical properties of III-V MOS devices [52]. However, the comparison study of Al_2O_3 on sulphur passivated and nitrided III-V surfaces shows similar origin of interface traps at both interfaces [40]. This suggests that nitridation is also a possible passivation method compatible with substrates similar to ammonium sulphide based sulphur treatments. However sulphur passivation of germanium MOS structures has been shown to result in lower fixed charge and interface state density than nitridation treatment [53].

1.4.3.3 Halogenation

Chlorine and bromine treatments on germanium and III-V surfaces are commonly achieved by HCl and HBr chemical solutions [54-57]. Delabie et al [57] reported that HBr treatment

completely removes germanium oxide whereas traditional hydrogen fluoride (HF) treatment leaves ~ 0.3 nm oxide on the germanium surface. As for III-V and germanium surfaces, the HCl treatment was not effective at completely removing the native oxides [57,58]. The HBr based chemical treatment on III-V surface also shows complete removal of oxides [56,57]. However HBr pre-treatment on germanium surfaces results in higher break down voltage than HCl:H_2O_2 mixture treated sample for the MOS stacks [59]. As already mentioned Cl termination of germanium was not as effective as sulphur passivation in preventing ambient oxidation [32]. However HCl plus sulphur passivation on both substrates shows improvement in the electrical characteristics of the MOS stacks [60,61].

1.5 Thesis organisation

Chapter 2 discusses the principle of surface characterisation tools employed in this study such as x-ray photoelectron spectroscopy (XPS) and soft x-ray photoelectron spectroscopy (SXPS). The detailed explanations of deposition techniques including thermal evaporation and atomic layer deposition are presented. The basic operation of metal oxide semiconductor (MOS) and extraction of various electrical parameters from CV measurements are also described. Chapter 3 presents the effectiveness of selenium passivation layer on both germanium and InAs substrate in preventing growth of interfacial oxides during MgO deposition. In addition, a comparison study between the thermal cleaning of the native oxide covered InAs(100) surface and atomic hydrogen cleaning has also been undertaken using soft x-ray photoemission spectroscopy. Chapter 4 and 5 investigate the thermal stability of high-k materials (Al_2O_3 and HfO_2) deposited on both germanium and InAs surfaces as a function of surface preparations using synchrotron based photoemission spectroscopy. These chapters discuss possible ways to prepare oxide free semiconductor-dielectric interfaces and evaluate and report on the thermal stability of interfacial oxides which form on both substrates during

high-κ deposition. Chapter 6 presents the effect of sulphur passivation in tuning chemical and electrical properties of metal/Al_2O_3/Ge MOS stacks and discusses the electrical and chemical impact of alcohol based sulphur passivation treatments on germanium MOS stacks. The systematic electrical studies of post deposition annealing in oxygen and forming gas ambient are also presented. Chapter 7 discusses the overall conclusions and future suggested works.

1.6 References

[1]. http://www.itrs.net/

[2]. G. E. Moore Electronics, Volume 38, Number 8, April 19, (1965).

[3]. G. D. Wilk, R. M. Wallace, J. M. Anthony, J. Appl. Phys. 89, 5243 (2001).

[4]. J. Robertson, Eur. Phys. J. Appl. Phys. 28, 265–291 (2004).

[5]. E. Martinez, H. Grampeix, O. Desplats, A. Herrera-Gomez, O. Ceballos-Sanchez, J. Guerrero, K. Yckache, F. Martin, Chem. Phys. Lett. 539–540, p139–143, (2012).

[6]. J. Robertson, Solid-State Electronics, 49, 283-293, (2005).

[7]. N. A. Ives, G. W. Stupian, and M. S. Leung, Appl. Phys. Lett. 50, 256-258 (1987).

[8]. D.K. Sadana, IBM, III-V substrate Eng, Dec 4,(2005).

[9]. N. Holonyak, Proceedings of the IEEE, 85, 11(1997).

[10]. K. Heime, InGaAs Field-Effect Transistors, Research Studies Press Ltd, Taunton, United Kingdom (1982).

[11]. http://www.ioffe.ru/SVA/NSM/Semicond/

[12]. T. Deegan and G. Hughes, Appl. Surf. Sci. 123, 66-70 (1998).

[13]. H.E. Farnsworth, R.E. Schlier, T.H. George, and R. M. Burger, J. Appl. Phys. 26, 252 (1955).

[14]. O.E. Tereshchenko, D. Paget, A. C. H. Rowe, V. L. Berkovits, P. Chiaradia, B. P. Doyle, S. Nannarone, Surf. Sci. 603,518–522 (2009).

[15]. C. L. Hinkle, A. M. Sonnet, E. M. Vogel, S. McDonnell, G. J. Hughes, M. Milojevic, B. Lee, F. S. Aguirre-Tostado, K. J. Choi, J. Kim, and R. M. Wallace, Appl. Phys. Lett. 91, 163512 (2007).

[16]. F. S. Aguirre-Tostado, M. Milojevic, C. L. Hinkle, E. M. Vogel, R. M. Wallace, S. McDonnell, and G. J. Hughes, Appl. Phys. Lett. 92, 171906 (2008).

[17]. D. Y. Petrovykh, M. J. Yang, L. J. Whitman, Surf. Sci. 523 231–240(2003).

[18]. T. Maeda, S. Takagi, T. Ohnishi, and M. Lippmaa, Mater. Sci. Semicond. Process. 9,706 (2006).

[19]. J. Roche, P. Ryan, G. J Hughes, Appl. Surf. Sci. 174, p 271-274(2001).

[20]. M. M. Frank, S. J. Koester, M. Copel, J. A. Ott, V. K. Paruchuri, H. Shang and R. Loesing, Appl. Phys .Letts.89, 112905 (2006).

[21]. M. Katayama, M. Aono, H. Oigawa, Y. Nannichi, H. Sugahara and M. Oshima, Jpn. J. Appl. Phys. 30 , p. L786-L789, (1991).

[22]. R.K.Chellappan and G. Hughes, Rapid Research letter (In press).

[23]. N. Takeuchi, Surface science 426, 433-439 (1999).

[24]. L. Chauhan and G. Hughes, J. Appl. Phys. 111, 114512 (2012).

[25]. R.K. Chellappan, Z. Li, G. Hughes (submitted applied surface science).

[26]. S. A. Chambers and V. S. Sundaram, J. Vac. Sci. Technol. B 9, 2256(1991).

[27]. M. Rohlfing, P. Kruger, J. Pollmann, Phys. Rev. B 54, 13759, (1996).

[28]. M. Houssa, D. Nelis, D. Hellin, G. Pourtois, T. Conard, K. Paredis, K. Vanormelingen, A. Vantomme, M. K. VanBael, J. Mullens, M. Caymax, M. Meuris, M. M. Heyns Appl. Phys. Lett. 90, 222105 (2007).

[29]. C. Merckling, Y. C. Chang, C.Y. Lub, J. Penaude, M. El-Kazzif, F. Bellengera, G. Brammertza, M. Hong, J. Kwoc, M. Meuris, J. Dekoster, M.M.Heyns, M.Caymax, Micro. Eng. 88, 399-402 (2011).

[30]. G. K. Dalapati, Y. Tong, W. Y. Loh, H. K. Mun, B. J. Cho, Appl. Phys. Lett. 90 183510 (2007).

[31]. G. K. Dalapati, Y. Tong, W. Y. Loh, H.K Mun, B. J. Cho, IEEE Trans. Electron Devices 54, 1831 (2007).

[32]. D. Bodlaki, H. Yamamoto, D.H. Waldeck, E. Borguet Surface Science, 543,p.63-74 (2003).

[33]. A. V. Thathachary, K. N. Bhat, N. Bhat, M. S. Hegde, Appl. Phys. Lett. 96, 152108 (2010).

[34]. S. Sioncke, H. C. Lin, A. Delabie, T. Conard, H. Struyf, S. DeGendt, M. Caymax, ECS Journal of Solid State Science and Technology, 3, p127-132 (2012).

[35]. D. Tsoutsou , Y. Panayiotatos, S. Galata, A. Sotiropoulos, G. Mavrou, E. Golias and A. Dimoulas, Microelectronic Engineering 88, 407 (2011).

[36]. C. J. Sandroff, M. S. Hegde, L. A. Farrow, R. Bhat, J. P. Harbison, C. C. Chang, J. Appl. Phys. 67, 586(1990).

[37]. B. A. Kuruvill, G. V. Ghaisas, A. Datta, S. Banerjee, S. K. Kulkarni, J. Appl. Phys. 73, 4384(1993).

[38]. K. Tsuchiya, M. Sakata, A. Funyu, H. Ikoma, Jpn.J.Appl.Phys.34, 5926 (1995).

[39]. T. Hoshii, S Lee, R. Suzuki, N.Taoka, M. Yokoyama, H. Yamada, M .Hata, T. Yasuda,M. Takenaka, S. Takagi J.Appl.Phys.112,073702(2012).

[40]. T. Maeda, M. Nishizawa, Y. Morita and S. Takagi Appl. Phys. Lett. 90, 072911 (2007).

[41]. V. L. Berkovits, V. P. Ulin, M. Losurdo, P. Capezzuto, G. Bruno, G. Perna, V. Capozzi, Appl. Phys. Lett. 80, 3739 (2002).

[42]. N. Wu, Q. Zhang, C. Zhu, C. C. Yeo, S. J. Whang ,D.S.H. Chan, M. F. Li and B. J. Cho, Appl. Phys. Lett. 84, 3741 (2004).

[43]. A. Toriumi, T. Tabata, C. H. Lee, T. Nishimura, K. Kita, K. Nagashio, Micro. Eng. 86, 1571 (2009).

[44]. I. Aksenov, Y. Nakada, H. Okomura, Jpn. J. Appl. Phys. 38, 2510 (1999).

[45]. A. Masuda, Y. Yonezawa, A. Morimoto, T. Shimizu, Jpn. J. Appl. Phys, 34, 1075 (1995).

[46]. V. G. Antipov, A. S. Zubrilov, A. V. Merkulov, S. A. Nikishin, A. A. Sitnikova, M. V. Stepanov, S. I. Troshkov, V. P. Ulin, N. N. Faleev, Semicond. 29, 946 (1995).

[47]. C. O. Chui, F.Ito and K. C. Saraswat, IEEE Electron Device Lett. 25, 613 (2004).

[48]. T. Maeda,T. Yasuda, M. Nishizawa, S. Takagi, Appl. Phys. Lett. 85, 3181 (2004).

[49]. E. P. Gusev, H. Shang, M. Copel, M. Gribelyuk, C. D'Emic, P. Kozlowski, T. Zabel, Appl.Phys.Lett.85, 2334 (2004).

[50]. Y. Oshima, Y. Sun, D. Kuzum, T. Sugawara, K. C. Saraswat, P. Pianetta, P. C. McIntyre, J. Electrochem. Soc.155, 304 (2008).

[51]. Y. Oshima, M. Shandalov, Y. Sun, P. Pianetta, P. C. McIntyre, Appl. Phys. Lett. 94, 183102 (2009).

[52]. F. Gao, S. J. Lee, D. Z. Chi, S. Balakumar, D. L. Kwong, Appl. Phys. Lett. 90, 252904 (2007).

[53]. T. Maeda, T. Shinichi, O. Tsuyoshi, L. Mikk , Mater. Sci. Semicond. Proc.9,706-710 (2006).

[54]. J. Kim, J. McVittie, K. Saraswat, Y. Nishi, S. Liu, and S. Tan: ECS Trans.3 1191 (2006).

[55]. Y. Moriyama, N. Hirashita, K. Usuda, S. Nakaharai, N. Sugiyama, E. Toyoda, and S. Takagi, Appl. Surf. Sci. 256, 823 (2009).

[56]. E. Yablonovitch, R. Bhat, C. E. Zah, T. J. Gmitter, M. A. Koza, Appl. Phys. Lett. 60, 371 (1992).

[57]. A. Delabie, D. P. Brunco, T. Conard, P. Favia, H. Bender, A. Franquet, S. Sioncke, W. Vandervorst, S. V. Elshocht, M. Heyns, M. Meuris, E. Kim, P. C. McIntyre, K. C. Saraswat, J. M. LeBeau, J. Cagnon, S. Stemmer, W.Tsaie, J. Electrochemic. Soc, 155, p H937-H944 (2008).

[58]. J. Kim, S. Liu, S. Tan, J. McVittie , K. Saraswat ,Y. Nishi ECS Trans, 3, 1191-1196 (2006).

[59]. O. Bethge, S. Abermann, C. Henkel, E. Bertagnolli ECS Transactions, 16, 365-373 (2008).

[60]. H. Trinh, E. Y. Chang, Y. Wong, C. Yu, C. Chang, Y. Lin, H. Nguyen and B. Tran, Jpn. J. Appl. Phys. 49, 111201 (2010).

[61]. X. Bai-Qing, C. Hu-Dong, S. Bing, W. Sheng-Kai, L. Hong-Gang, Chin. Phys. Lett. 29, 046801 (2012).

2. Principles of the main experimental techniques

This chapter discusses the principles of the surface characterisation tools employed in this study such as x-ray photoelectron spectroscopy (XPS) and soft x-ray photoelectron spectroscopy (SXPS). The detailed explanations of deposition techniques including thermal evaporation and atomic layer deposition are presented. The basic operation of metal oxide semiconductor devices and extraction of various electrical parameters from CV measurements are also described.

2.1 X-ray photoelectron spectroscopy (XPS)

X-ray photoelectron spectroscopy is a highly surface sensitive analytical tool used for the chemical analysis of solid surfaces. X-ray irradiation of samples results in the emission of electrons via the photoelectric effect [1], as for example photoelectron emission from the O 1s core level as shown in figure 2.1.

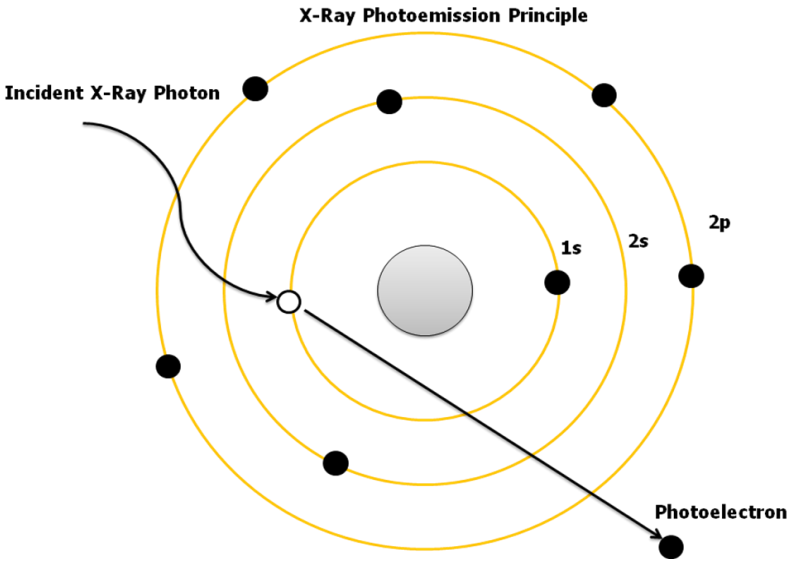

Figure 2.1: Schematic showing photoelectron emission from the O 1s core level [2].

The incident X-ray can penetrate up to ~ 1 μm and covers an area ~ 1×1 cm^2 as schematically shown in figure 2.2. The probability of photo emitted electrons escaping from the surface without any collision decays exponentially with depth into the solid, thus elemental information can only be extracted from the outermost layers (< 10 nm) making XPS a surface sensitive analytical tool.

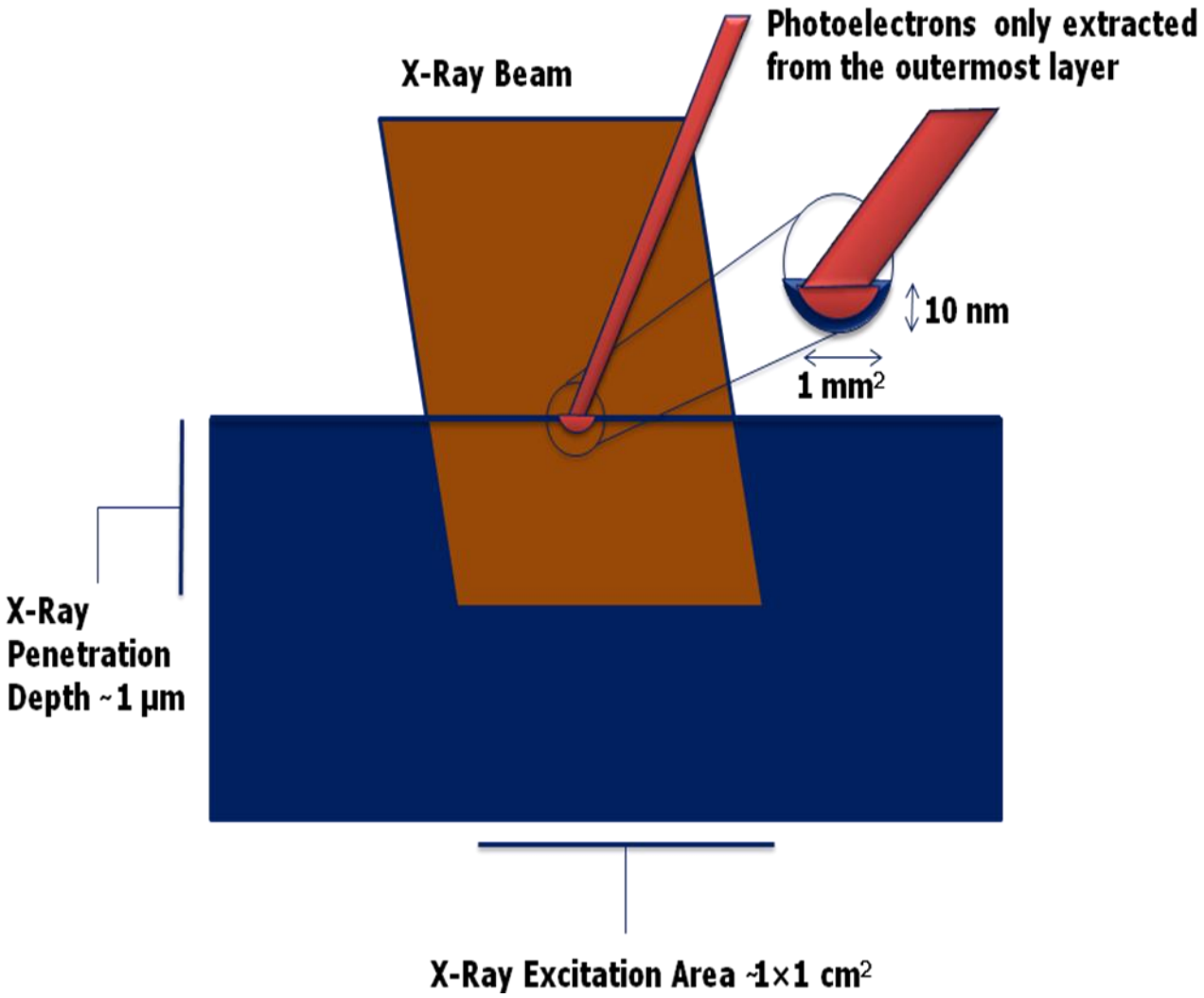

Figure 2.2: Schematic diagram showing surface sensitivity of XPS [2, 3].

2.1.1. XPS instrumentation

The schematic of a XPS experimental set up is shown in figure 2.3.When a sample surface is irradiated with low energy (< 1500 eV) x-rays in a vacuum environment, the photoemitted electrons with a wide range of kinetic energies can be collected by an electron energy analyzer and ultimately the intensity of the signal can be plotted as a function of kinetic energy.

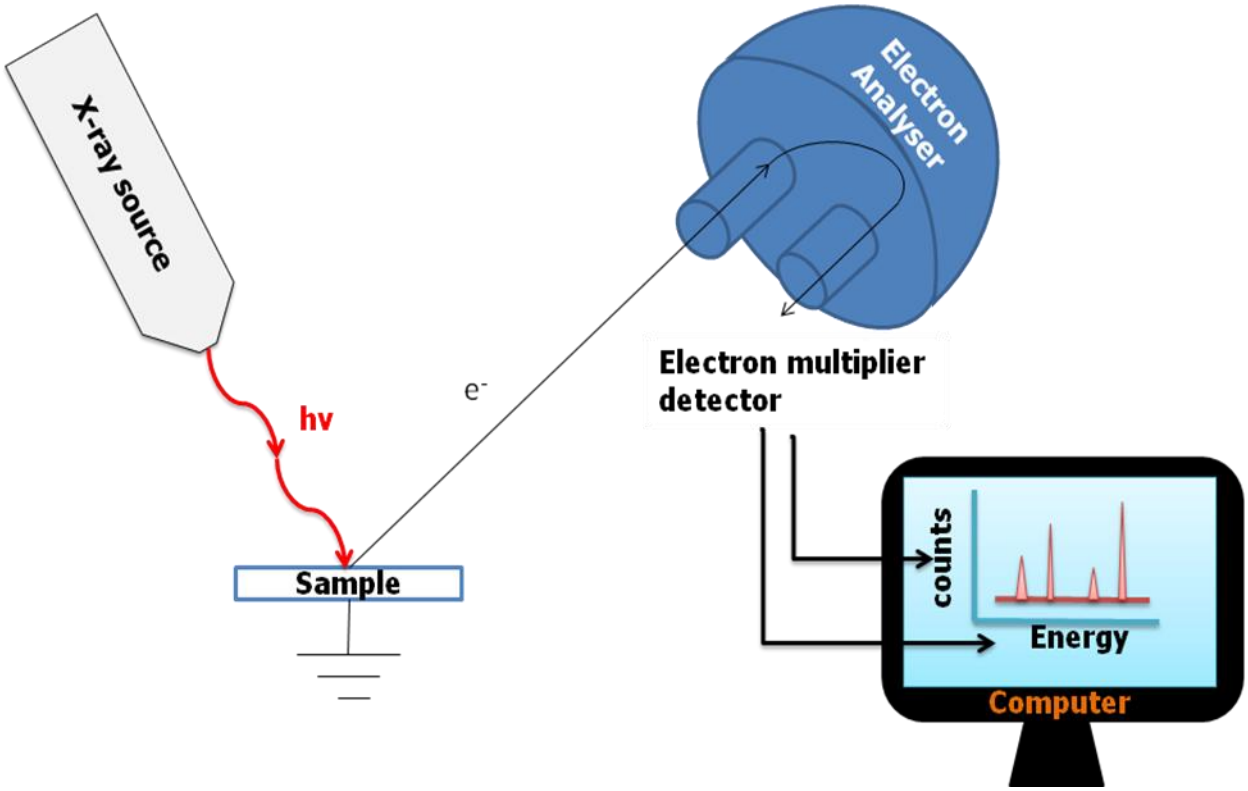

Figure 2.3: Basic experimental setup of conventional XPS system [3].

Maintaining the vacuum at ~ 10^{-9} mbar in the analysis chamber facilitates the transmission of photoelectrons into the energy analyzer. The set up basically consist of an x-ray source, a sample under investigation, an electrostatic lens, an electron energy hemispherical analyser, detection system and computer controlled output to display the acquired spectrum.

2.1.1.1. Hemispherical electron energy analyzer

The electron energy analyzer shown in figure 2.4 consist of two concentric hemispheres with the radii of curvature R_1 and R_2. By the application of different applied voltages to the two hemispheres with the outer hemisphere being more negative than the inner hemisphere, it allows electrons with a given kinetic energy so called the "pass energy" to reach the detector.

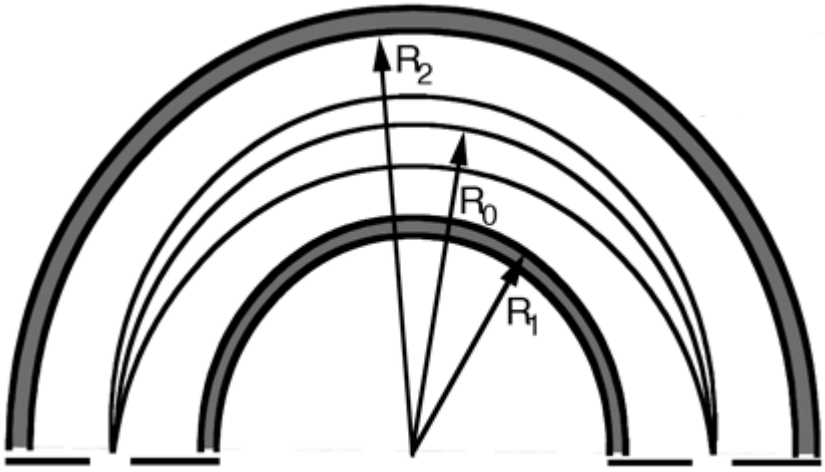

Figure 2.4: Schematic representation of hemispherical energy analyser.

$$E = e\Delta V\left(\frac{R_1 R_2}{R_2^2 - R_1^2}\right) \qquad 2.1$$

Where E is the kinetic energy of the photoelectrons, e is the electron charge, ΔV is the voltage difference between concentric hemispheres with radii of R_1 and R_2.

The radius of hemispheres is constant therefore the above equation 2.1 can be written as

$$E = Ke\Delta V \qquad 2.2$$

Where the spectrometer constant is given as K and it depends on the analyser design.

The electrons with higher kinetic energy than the pass energy will collide with the outer hemisphere as they will try to follow a radius larger than mean radius of hemisphere while however electrons with energy less than the pass energy will travel in smaller radius than the mean radius and therefore collide with the inner hemisphere.

2.1.1.2 Dual anode x-ray source

The x-ray source in a conventional XPS system is usually equipped with twin anodes which can generate different monochromatic x-ray lines typically, Al Kα and Mg Kα lines. These characteristic x-ray lines have photon energies of 1486.7 eV and 1253.6 eV which allow for core level electron excitation for many elements in the periodic table. Figure 2.5 shows a schematic diagram for a dual anode x-ray source consisting of filaments (cathode) and water cooled anodes mounted on a supporting copper rod.

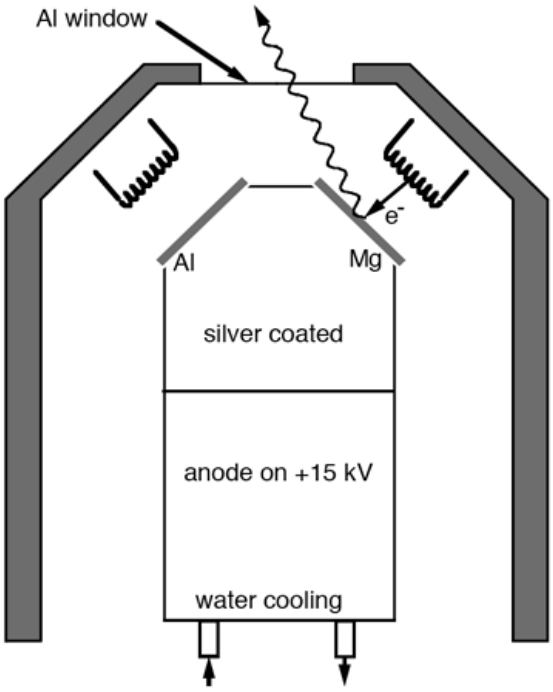

Figure 2.5: Schematic drawing of x-ray dual anode source [4].

High intense Bremsstrahlung radiation is produced when the water cooled anode is bombarded by high energy electrons accelerated from the filaments through a potential difference ranging from 10-15 kV. The high operating voltage of the anode combined with milliamp current emission generates significant waste heat necessitating adequate water cooling to avoid evaporation and interdiffusion of metal films from the anode surface. The high intensity Kα emission lines are generated by the transition of electrons from the Al or Mg 2p doublets to the 1s core level vacancies created by the incident high energy electrons. These emission lines result in the generation of characteristic x-ray lines 1486.7 eV and 1253.6 eV with the energy spread (line width) of 0.85 eV and 0.7 eV for the aluminium and magnesium anode targets, respectively. Aluminium foil (~ 2 μm) placed at the exit aperture of x-ray source protects the sample from stray electrons, contamination and the heat from the filaments.

2.1.1.3 Electrostatic lens

The electrostatic lens collects photo emitted electron from a wide angular distribution and directs them to the entrance of the electron energy analyzer. It retards the energy of electron to the pass energy.

2.1.1.4 Channeltron detector

The channeltron detector consists of a spiral glass tube which is connected to the output of the analyser and is schematically shown in figure 2.6. The inner walls are coated with an insulating material such that an incident electron on the material can results an emission of many secondary electrons.

The potential applied across the channeltron of typically 3 kV accelerates the incoming photoelectrons and ensures that the electron cascade effect amplifies the incoming signal. The output of channeltron is fed into the pulse counter where it provides a count rate of typically higher than 10^6 counts per second (c.p.s).

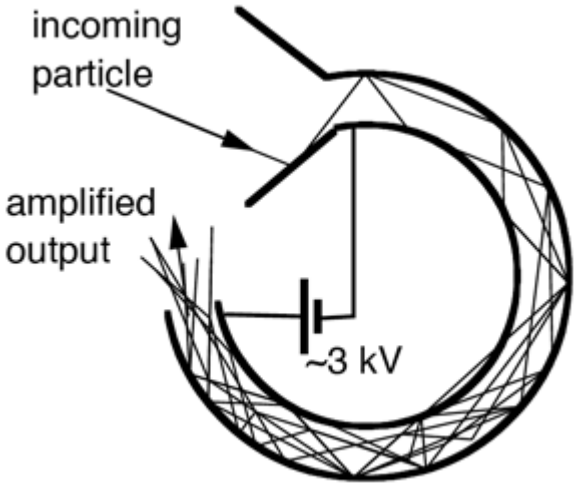

Figure 2.6: Schematic diagram showing channeltron detector [4].

2.1.2 Energy level diagram of photoemission analysis process

The energy level diagram for the principle of photoemission spectroscopy is shown in figure 2.7. The sum of kinetic energy and binding energy with respect to Fermi level of the photo emitted electron is not equal to the irradiated x-rays photon energy. Thus the difference between Fermi and vacuum level referred as work function has to be included while calculating the actual kinetic energy and expressed in the following equation 2.3.

$$h\nu = E_B^f + E_{kin}^1 + \phi_s \qquad 2.3$$

It is assumed in figure 2.7 that sample and spectrometer are in electrical contact. When electrons pass from sample to spectrometer they experience a potential difference which is equal to the difference between sample and spectrometer work functions. Therefore measured kinetic energy can be written as

$$E_{kin} = E_{kin}^{1} + (\phi_s - \phi_{spec}) \qquad 2.4$$

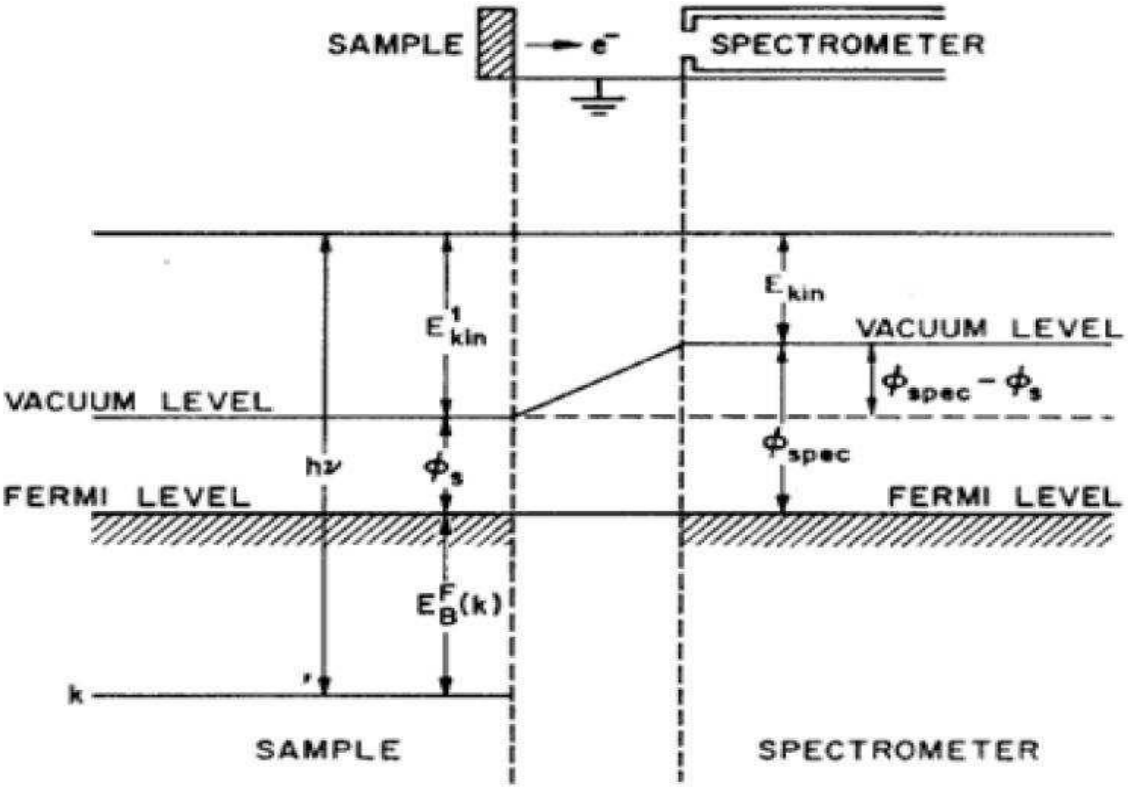

Figure 2.7: Energy level diagram showing spectrometer and sample in electrical contact [5].

By substituting the measured kinetic energy into equation 2.4, the following photon energy expression can be found.

$$h\nu = E_B^f + E_{kin} + \phi_{spec} \qquad 2.5$$

After re-arranging equation 2.5

$$E_B^f = h\nu - E_{kin} - \phi_{spec} \qquad 2.6$$

The equation 2.6 allows the calculation of binding energy of an electron by knowing the incident x-ray photon energy, measured kinetic energy and the spectrometer work function. The binding energy of a particular photoemitted electron provides element specific information which can be used to identify that element.

2.1.3 Inelastic mean free path

The photoemitted electrons which are scattered in the solid prior to emerging and being detected in the analyser provide no useful information via the photoelectric effect and contribute to the secondary electron background in the spectrum. The average distance an electron travels in a solid without been involved in any collision is termed the inelastic mean free path (IMFP). This is generally material independent and the kinetic energy dependence is shown in figure 2.8.

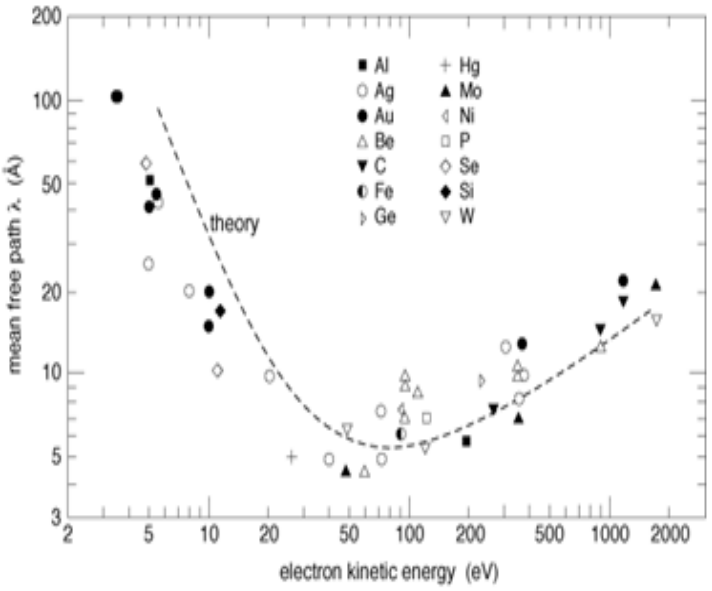

Figure 2.8: Universal mean free path λ of electrons in a range of materials [6].

The minimum IMFP (< 0.50 nm) covers the electron kinetic energy range between 50-100 eV which indicates that the photoemitted electrons with these energies will have the greatest surface sensitivity. The probability of an electron P(d) travelling a distance d within the solid without any scattering can be expressed as follows in equation 2.7.

$$P(d) = e^{\frac{-d}{\lambda}} \qquad 2.7$$

Where λ is IMFP of the electron and d is the thickness of a layer. The exponential decay of the probability as a function of depth into the solid is shown in figure 2.9.

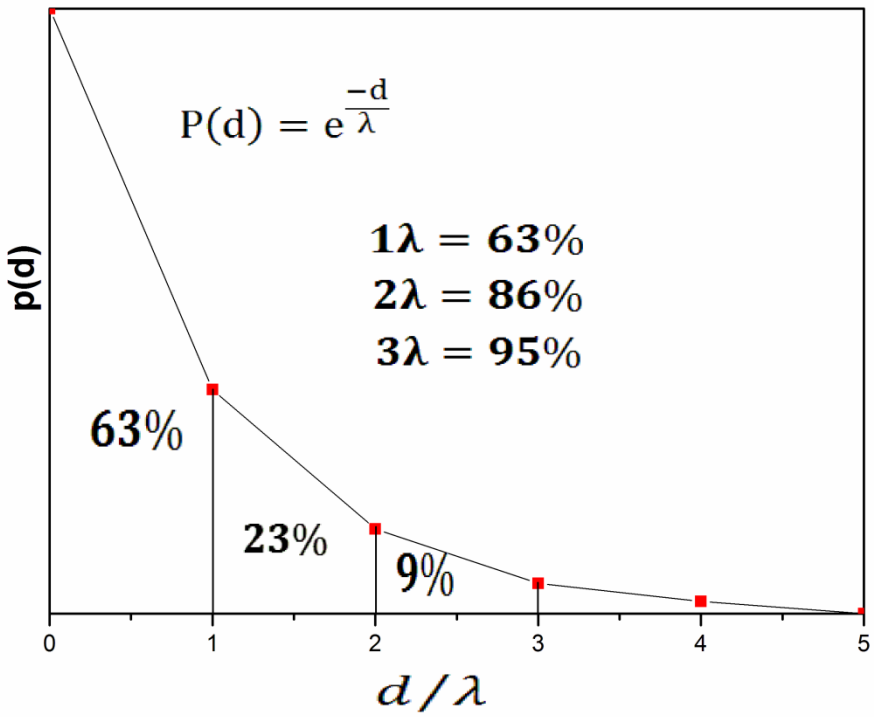

Figure 2.9: Diagram showing emission of unscattered photoelectron as a function of sample depth.

The integration of the area up to 3λ constitutes 95% of unscattered photoemitted electrons and is called the sampling depth into the material. The typical IMFPs for photoemitted

electrons using the conventional x-ray source fall in the range of 1-2 nm, giving an overall sampling depth range of 3-6 nm for most solids.

2.1.4 Elemental identification and chemical shifts

The survey spectrum for a particular sample allows identification of all elements present on the surface of the sample with a concentration greater than ~ 0.1%. The core level peaks can be identified using unique binding energies as illustrated for a germanium sample survey spectrum shown in figure 2.10.

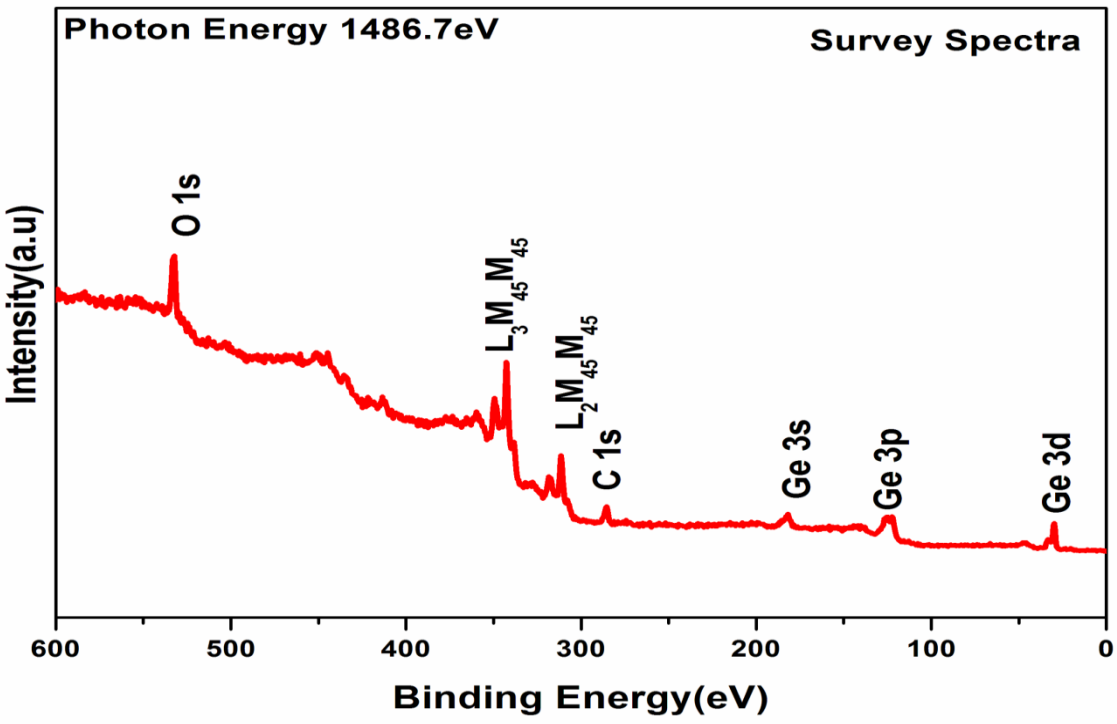

Figure 2.10: Germanium survey spectra taken at 1486.7eV showing photoelectrons from germanium, carbon and oxygen core levels.

Another important feature of XPS is the ability to distinguish the same element in different chemical environments. Changes in the electron density around the atom due to chemical

interaction scan result in the observation of a chemically shifted component of the core level peaks. These chemical shifts are basically dependent on the electronegativity of the bonding atoms. The Ge 3d spectrum from a native oxide covered germanium surface shown in figure 2.11 displays two component peaks which have been curve fitted. The main peak at a binding energy of 29.9 eV is attributed to the Ge substrate while the peak at 32.9 eV is attributed to germanium-oxide component previously identified as being Ge_2O_3 (Ge^{3+}) [7].

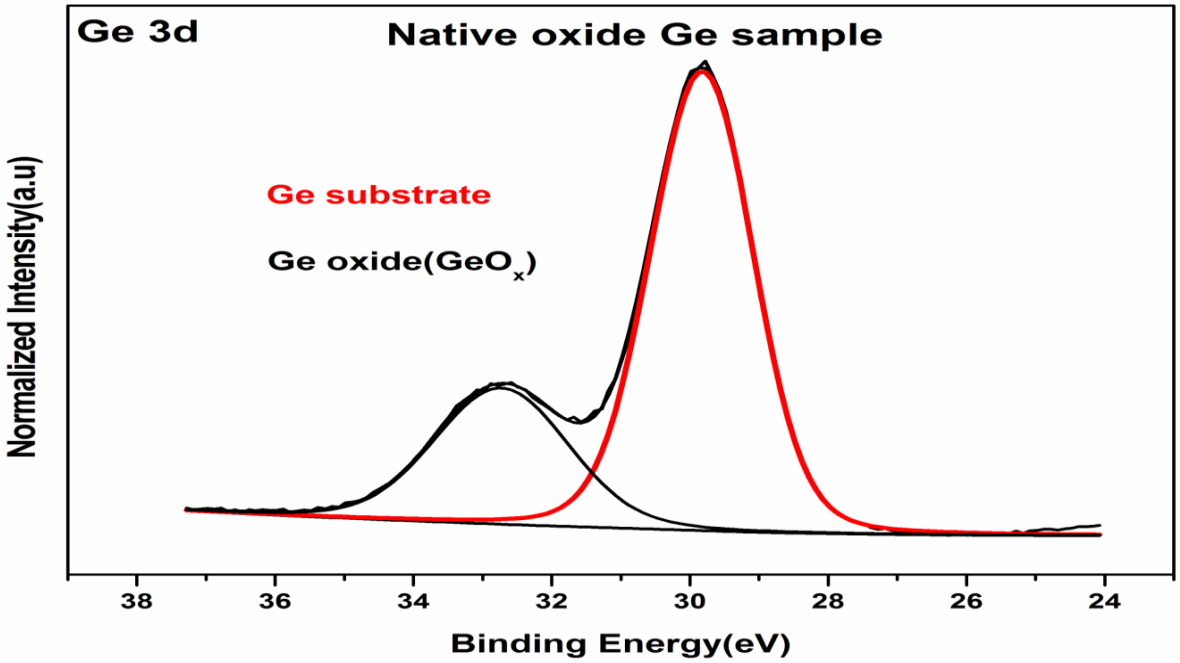

Figure 2.11: Ge 3d core level spectra of the native oxide on a germanium surface.

The higher binding energy of the oxide component reflects the increased ionic nature of the Ge-O bond relative to the Ge-Ge bond. The electrons emerging from these slightly positive Ge atoms have less kinetic energy compare to Ge-Ge bonds which results in the peak appearing at higher binding energy. The thickness of thin oxide layer can be calculated from the intensity attenuation of photoemission signal from the substrate after deposition of a thin overlayer by using the following equation 2.8.

$$I_o = Ie^{\frac{-d}{\lambda}} \qquad 2.8$$

Where I_o and I is the intensity before and after oxide deposition, λ attenuation length in the oxide and d is the thickness of the over layer. The thickness can also be determined from the ratio in intensity of the oxides to substrate peaks.

2.1.5 Peak width

The peak width of given a photoemission signal is defined as a convolution of a Gaussian and a Lorentzian peak. The full width at half maximum (FWHM) of a peak is composed of contributions from electron energy analyser E_a, x-ray source E_s and core hole life time E_l. The FWHM of a peak is defined as the square root of sum of squares of these contributions.

$$\text{FWHM} = ((E_a^2) + (E_s^2) + (E_l^2))^{\frac{1}{2}} \qquad 2.9$$

The line shape due to core hole life time and instrumental contribution is referred as Lorentzian and Gaussian. The intrinsic peak width (Γ) due to core hole life time is measured using Heisenberg uncertainty principle given in equation 2.10.

$$\Gamma = \frac{h}{\tau} \qquad 2.10$$

Where h is Plancks constant and τ is core hole life time, the intrinsic peak width is larger for inner shell than outer shell orbitals because electrons from outer shell orbitals fill vacancies created in the inner shell orbital. Therefore, the deeper the orbital, the larger the peak width and the shorter, the core hole life time. For example intrinsic peak widths of gold (Au) metal increases in the order of 4f < 4d < 4p < 4s. The probability of electrons fill inner core level from outer core level increases with increasing valence electron density. Hence intrinsic peak width increases with the increase of atomic number.

2.1.6 Depth analysis with kinetic energy

The sampling depth into a surface depends on the kinetic energy of the emerging photoelectrons. As an element in the material can have more than one core level at different binding energies, the effective sampling depth can be changed by analysing the photoemitted electrons from different core levels, particularly if they are well separated in binding energy. The Ge 3d and Ge 2p core level spectra recorded for the native oxide covered germanium surface using the Al kα x-ray source are shown in figure 2.12.

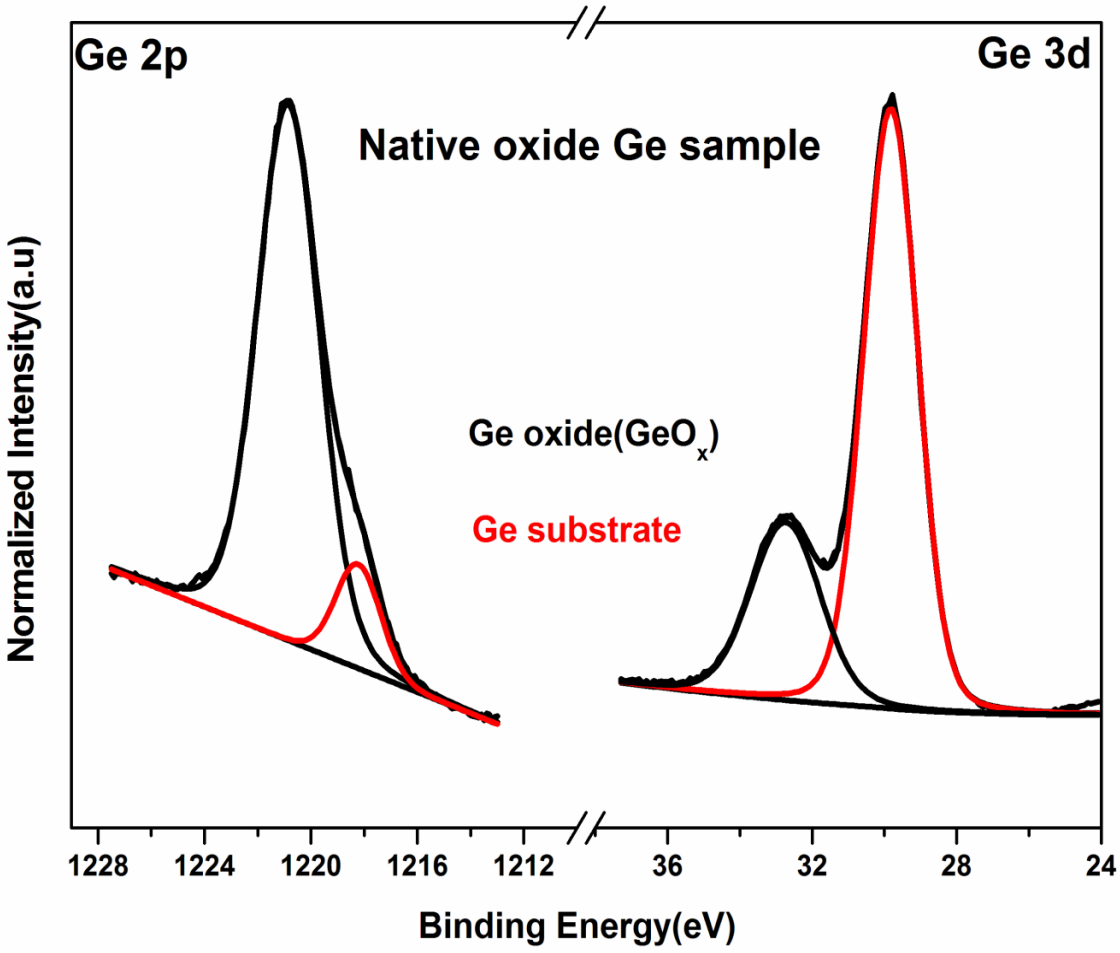

Figure 2.12: Ge 3d and Ge 2p core level spectra for the native oxide covered germanium surface.

The Ge 3d emerges at a kinetic energy of 1450 eV which gives a IMFP of ~ 2 nm as estimated from figure 2.8 with a corresponding sampling depth of ~ 6 nm. The kinetic energy of the emerging Ge 2p electrons is 264 eV giving an IMFP of ~ 0.8 nm and a sampling depth

into the surface of ~ 2.4 nm. This difference in sampling depth is reflected in the difference in the relative intensity of the substrate and oxide overlayer peaks which is directly related to the difference in the sampling depths for the two core level peaks. The shallower sampling depth for the Ge 2p core level results in a significantly larger oxide signal, as this is surface localised, than that observed for the Ge 3d peak. This is an effective non-destructive way of studying chemical information on the surface and bulk of the samples. The similar depth selectivity study can also be undertaken by exciting the same core level using different x-ray energies.

2.2 Synchrotron radiation

Synchrotron radiation is the electromagnetic radiation emitted by charged particles which are accelerating radially. When the velocity of the particles approaches the speed of light, the radiation emission pattern is strongly collimated in the forward direction. The resulting radiation produces a continuous wavelength spectrum from infrared to x-rays. The main advantage of using synchrotron light for photoemission studies is that higher surface sensitivity can be achieved by tuning the photon energy using a suitable monochromator such that the kinetic energy of the electrons emerging from a particular core level can be selected to coincide with the minimum value on the IMFP curve. This is not possible in conventional x-ray photoelectron spectroscopy as it has only fixed photon energies dependent on the anode selected. A schematic diagram of the ASTRID Synchrotron Storage Ring at Aarhus University is shown in figure 2.13. The photoemission studies of InAs and Ge samples studied in the work were carried out on the SX700 and SGM1 beam lines, which have photon energy ranges of 60 to 600 eV.

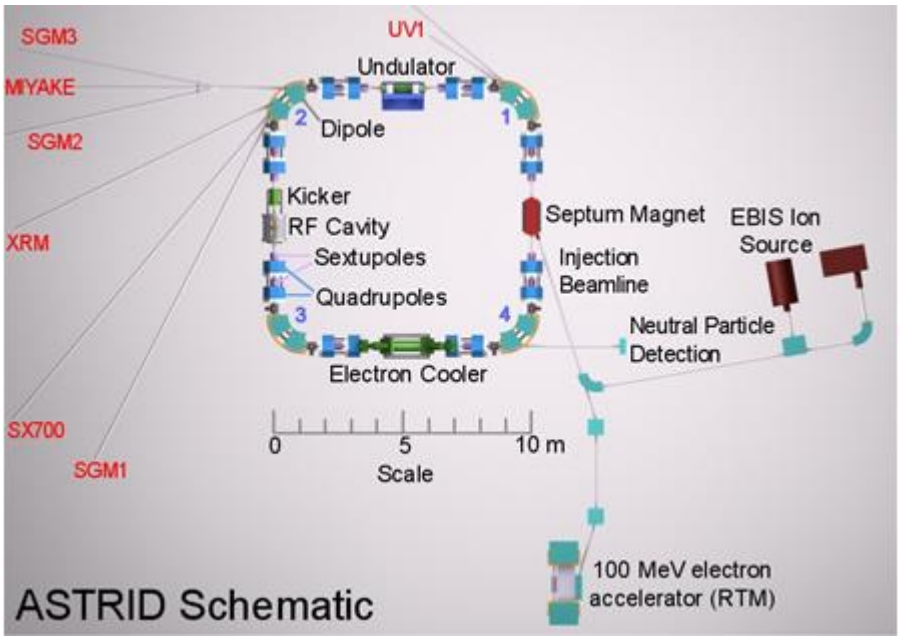

Figure 2.13: Schematic of ASTRID synchrotron storage ring [8].

2.2.1 Principle of operation

A schematic representation of a synchrotron light source layout is shown in figure 2.14. The basic instrument consists of an electron gun, a linear accelerator (linac), a booster ring and a storage ring. The electrons from the heated cathode filaments are fed into a linear particle accelerator (linac) where these electrons are accelerated by microwaves produced by radio frequency cavities. The linac then directs electrons into the booster ring which uses magnetic field and RF cavities to increase the energy of the electrons to high energy ~ 3 GeV. The electromagnets are used to direct and produce fine beam of electron bunches. The electrons are transferred to storage ring when the energy of electron inside the booster ring is close to speed light. The storage ring consists of straight tube like section and an arc of bending magnets. The insertion devices are connected along the straight sections to achieve change in electron trajectory. Insertion devices such as wiggler or undulator consist of periodic array of

magnets. If a wiggler is used as an insertion device then electrons undergoes wiggling action along the straight path and results high flux x-ray beam. As for undulator, the electrons are forced to travel into weaker zig-zag motion thus radiates energy before reaching the bending magnets which are at each corners of storage ring to direct electrons into a circular path. The photon ports at the storage ring feed synchrotron lights into the beam lines. The monochromaters connected between the photon port and the user research stations are used to select the user required photon energies to study material properties.

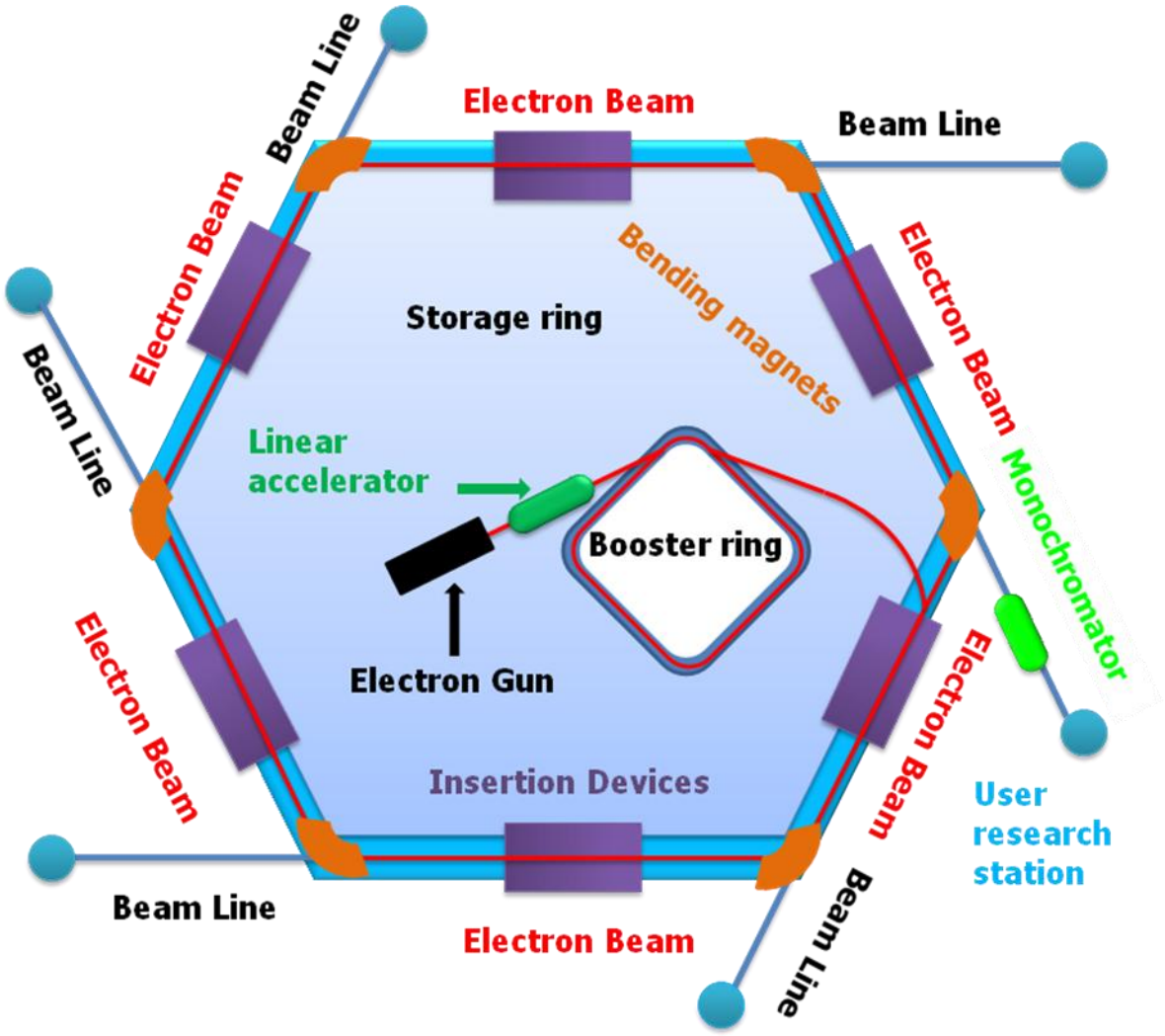

Figure 2.14: Schematic representation of synchrotron light generation [3].

2.2.2 Why SXPS?

This section discusses the surface sensitivity of SXPS over XPS in accurately identifying the chemical states at the sample surface. The As 3d spectra of the Al_2O_3 covered sulphur passivated InGaAs sample measured using XPS at 1486.7 eV and SXPS at photon energy of 92 eV are shown in figure 2.15.

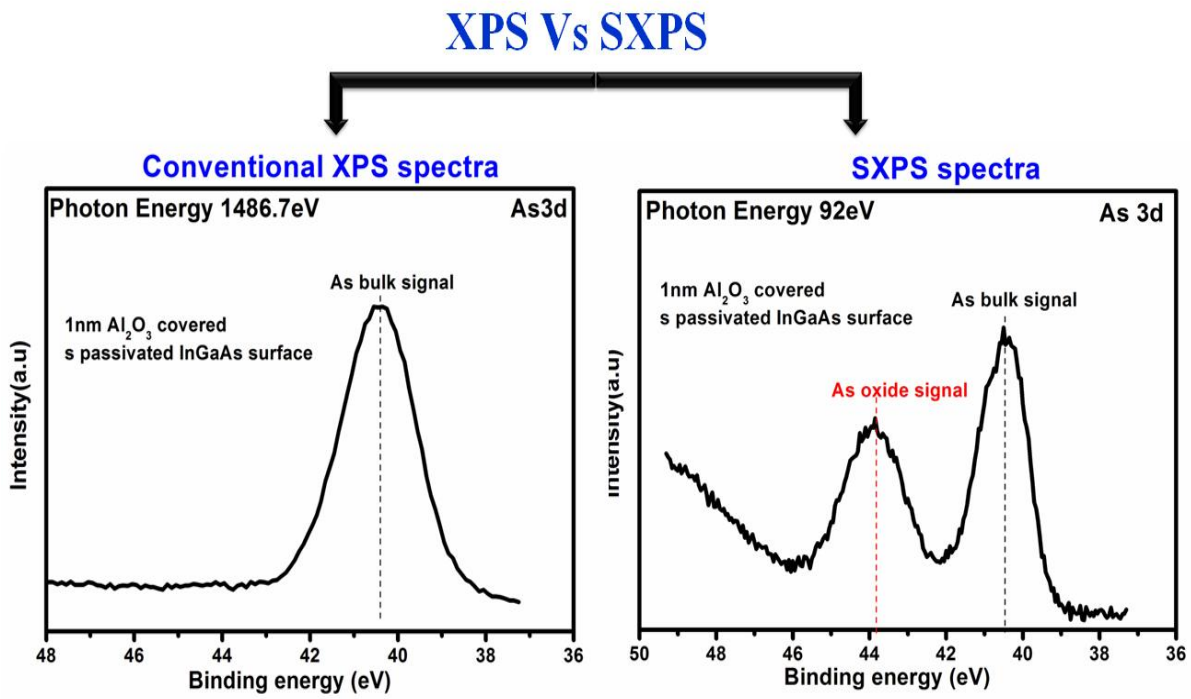

Figure 2.15: As 3d spectra of the Al_2O_3 covered sulphur passivated InGaAs surface measure using XPS and SXPS.

The same core level of same sample irradiated with XPS and SXPS results different kinetic energy for the emitted photoelectrons. Thus XPS and SXPS measurement offers sampling depth of ~ 7 nm and ~ 2 nm. This variation in sampling depth reveals that spectra recorded using SXPS results higher surface sensitive spectra than XPS. The As 3d spectra clearly shows high intense oxide signal measured using SXPS as 95% of photoelectrons are emitted within 2 nm from the surface. The As 3d spectra shows attenuated oxide signals which is measured using XPS. This suggest that photoelectrons emitted from bulk substrate is higher

than surface. Thus SXPS provides higher surface sensitivity than XPS measurements. However in SXPS tuning photon energy to vary sampling depth is an alternative non-destructive way to study chemical information as function of depth. This study is not possible in a conventional XPS as photon energies are fixed for the two anodes whereas already discussed that depth analysis can be possible by irradiating widely separated energy core levels. The energy resolution of SXPS spectra measured at lower photon energies are approximately 0.7 eV which is 0.3 eV lesser than our home XPS at DCU. The lower energy resolution offers higher chance of identifying any little interaction of atoms at the surface.

2.3 Thin film deposition

Thickness scaling of high-κ dielectric materials is a fundamental requirement for the future development of CMOS. Therefore parameters such as film uniformity, purity, roughness, coverage and defects have to be considered while choosing an oxide deposition method.

The two oxide deposition methods utilised in the course of this work were thermal evaporation and atomic layer deposition (ALD).

2.3.1 Thermal evaporation

High purity thin film metals and metal oxides can be deposited by heating the material which is mounted on a tungsten filament up to evaporation temperature. Alternatively, other materials can be thermally deposited from a tantalum pouch wrapped in a tungsten filament, particularly if the evaporation temperature isn't very high. In this course of study, selenium (purity of 99.9%) was deposited by thermal evaporation from a tantalum pouch on both germanium and InAs substrates. The metal oxide films (MgO) were deposited by evaporating magnesium metal from a tantalum pouch in an oxygen background pressure of 10^{-6} mbar. The

thickness of metal and metal oxide films were measured by taking account of substrate peak intensity before and after metal or metal oxide deposition.

2.3.2 Atomic Layer Deposition

Atomic Layer Deposition (ALD) is a self limiting chemical vapor deposition method for depositing a wide range of thin flims. The basic principle which involves layer by layer deposition of metal and oxide species offers high levels of film uniformity and thickness control thickness. In a metal oxide deposition, introduction of the metal precursor (or oxidant precursor), purge N_2 and the oxidant precursor (or metal precursor) sequentially into the reactor chamber constitutes one cycle. The required thickness of the metal oxide film can be achieved by controlling the number of cycles including purge time for metal and oxidant precursors at a constant substrate temperature. The metal and oxidant reaction sequence in a ALD deposition process is schematically shown in figure 2.16.

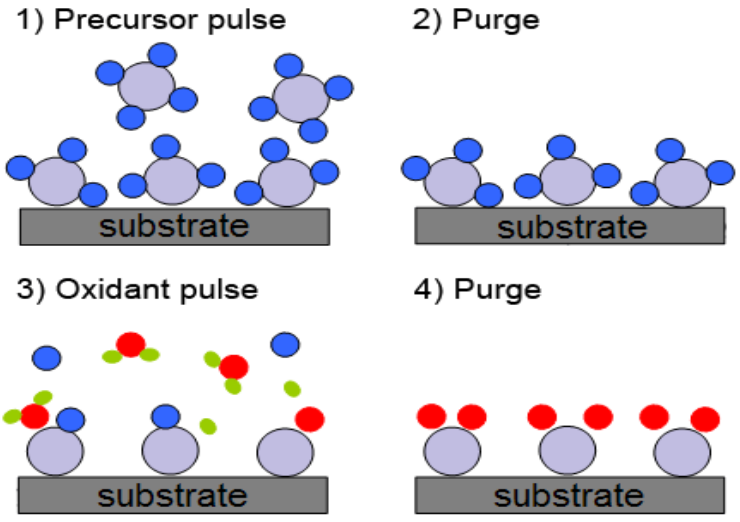

Figure 2.16: ALD process steps [9].

In the first step of ALD growth, the introduction of the metal precursor into the reactor saturates the surface through chemisorptions. The subsequent gas purging step removes excess or unreacted metal precursor and the subsequent introduction of the oxidant precursor

reacts with the functional group formed during the previous pulse. The removal of excess reactants by purging of N_2 prevents additional film growth. This self limiting oxide growth enables large coverage area, control of thickness, uniformity and pin hole free deposition. Typical substrate temperatures are 150^{o}C to 300^{o}C maintained during ALD deposition. This thesis investigates the high-κ materials such as Al_2O_3 and HfO_2 deposited using tri-methyl alumina (TMA), tetrakis (ethyl-methyl-amino) hafnium (TMEAH) and water as precursors on both germanium and InAs substrates.

2.4 Atomic Hydrogen Cracker

TC50 Oxford Instruments thermal cracker was used to generate atomic hydrogen beam which has previously been reported to remove the native oxides and carbon contamination from III-V substrate surfaces at relatively low substrate temperatures [14]. A schematic diagram of the thermal cracker is shown in figure 2.17.

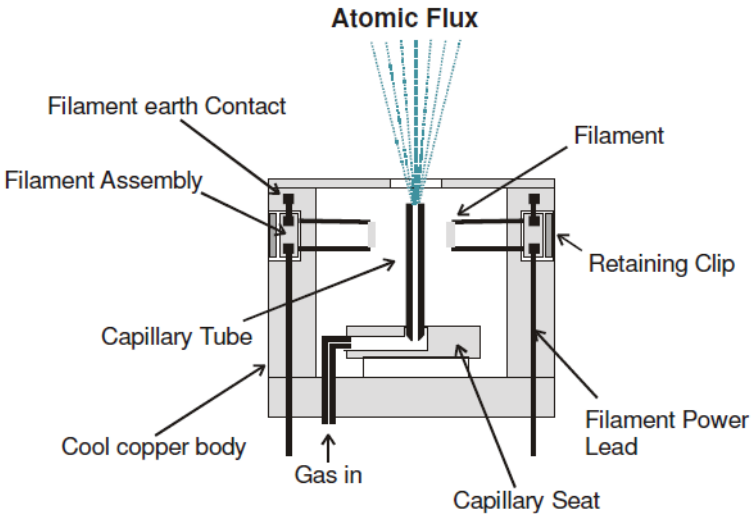

Figure 2.17: A schematic diagram of thermal cracker [10].

The capillary tube is held at 1 kV so the electrons emitted from the filament at earth potential accelerate towards it, which increases the temperature of capillary to more than 1000^{o}C.

Atomic hydrogen is produced when the hydrogen molecules thermally dissociates after hitting the capillary wall. This atomic hydrogen source was used to clean the InAs surface at relatively low temperatures.

2.5 Electrical Characterisation - CV measurements

Capacitance Voltage (CV) measurements are a widely used electrical characterization technique for metal oxide semiconductor (MOS) structures to study the physical parameters such as interface state density, fixed and mobile charges. The MOS structure is a two terminal device where the metal gate and semiconductor are the two terminals, shown in figure 2.18.

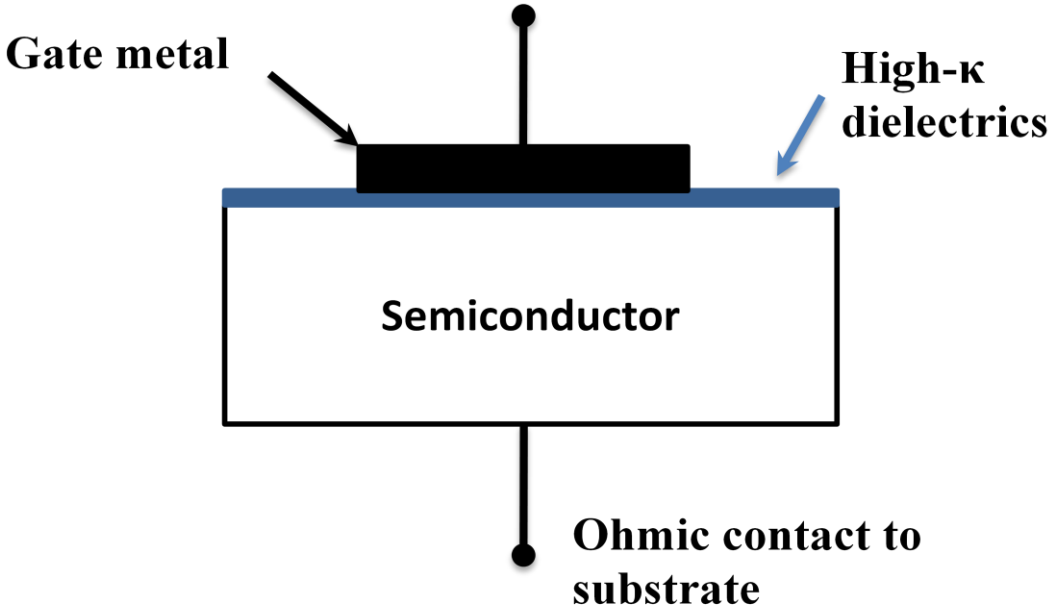

Figure 2.18: Metal Oxide Semiconductor capacitor.

The insulating high-κ gate dielectric prevents direct flow of current from the metal gate to the substrate while applying potential across it.

2.5.1 Non ideal MOS capacitor

Non-ideality behavior always existed in a practical MOS device due to the presence of fixed charge, mobile ionic charge and oxide trapped charges which are schematically shown in figure 2.19.

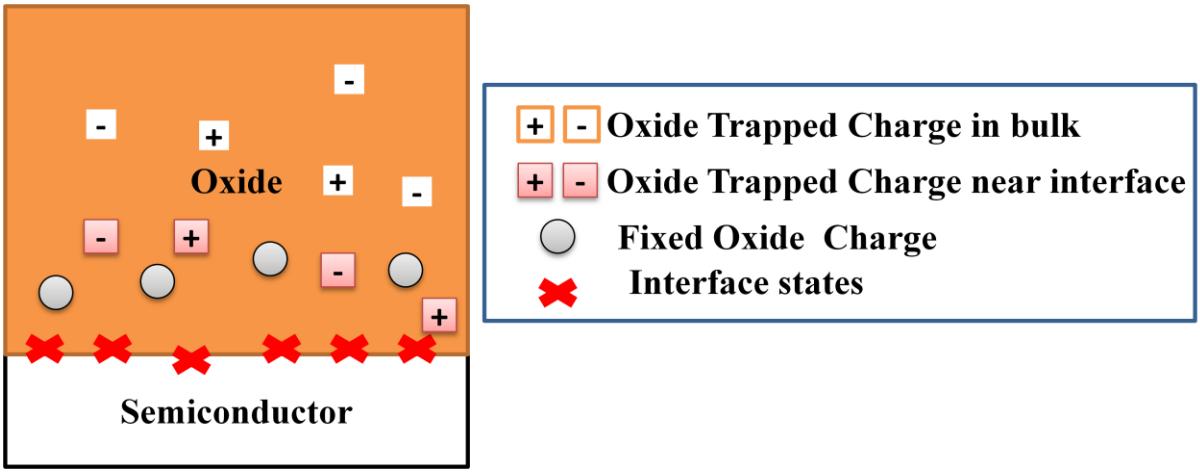

Figure 2.19: Schematic representation of charge in MOS capacitor [9].

The fixed charge can be present at the oxide/semiconductor interface or in the bulk region of oxide. This charge is independent of bias voltage applied to the MOS device. The CV curve shifts opposite to the polarity of fixed charge as schematically shown in figure 2.20 for a pMOS capacitor.

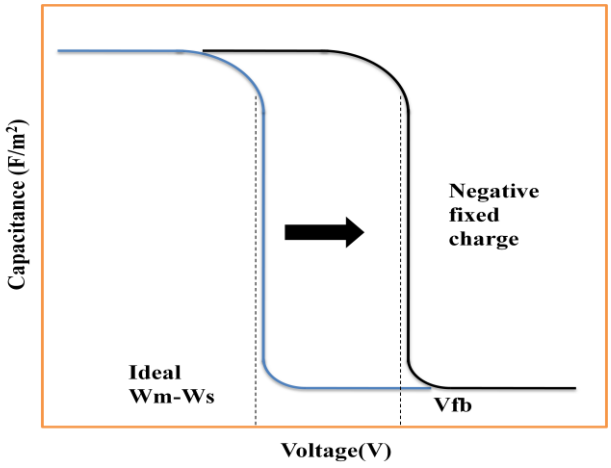

Figure 2.20: Effect of fixed charge in CV characteristics [9].

The CV curve shift towards the positive side in the above example indicating the presence of negative fixed charge in the MOS device. The charge trapping sites can be found in an amorphous dielectric layer due to its irregular structure. The oxide charge can be positive, negative or neutral depending upon holes or electrons trapped in these sites during the device operation. In an accumulation region, a p-type MOS device with high enough electric field in the semiconductor surface can push holes directly into the oxide, and these may get trapped in trapping sites. This type of carrier injection is referred as substrate injection of holes. Similarly, electrons injected from the gate metal in to the oxide layer is called gate injection. Hysteresis of a CV curve can be measured by sweeping from inversion to accumulation and then accumulation to inversion (back and forth) at high or low frequencies. An example illustrating hysteresis due to the effect of trapping and de-trapping of holes as a function CV measurement is shown in figure 2.21.

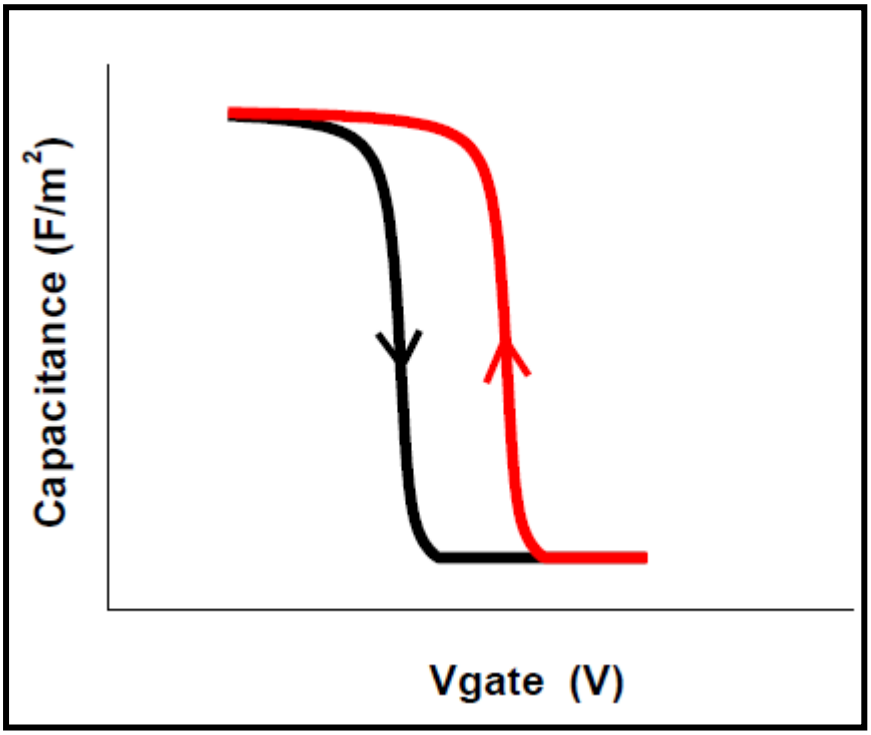

Figure 2.21: Hysteresis effect on the ideal CV curve [9].

The presence of impurities like Na^+/K^+ alkali ions act as mobile charge which moves depending on the gate bias and can result in unstable shifts in the threshold voltage. This charge can be significantly reduced by choosing proper surface cleaning and ALD-high-κ deposition.

2.5.2 Extraction of Interface states-Conductance method

The density of electrically active defects created at the semiconductor/oxide interface during the fabrication of MOS device is referred as density of interface states (D_{it}). The defect states will give rise to an energy level, if these levels are present in the bandgap of semiconductor then the electrical properties of MOS and MOSFET performance will be degraded. A conductance method is used to estimate the interface defect state densities of MOS gate stacks fabricated in this study. This method requires CV and conductance voltage measurements (GV) to extract the interface defect states. The parallel conductance (G_p) over angular frequency (ω) is given in equation 2.11

$$\frac{G_p}{\omega} = \frac{\omega \times C_{ox}^2 \times G_t}{(G_t + \omega^2 \times (C_{ox} - C_t)^2)} \qquad 2.11$$

Where C_{ox} is the oxide capacitance, C_t and G_t is the measured capacitance and conductance at respective voltages. The D_{it} can be extracted by substitution of equation 2.11 in the below equation 2.12.

$$D_{it} = \frac{2.5}{q} \left\langle \frac{G_p}{\omega} \right\rangle_{peak} \qquad 2.12$$

The interfacial defect states D_{it} were examined throughout the study using this conductance method which was developed by Nicollian and Goetzberger [11].

2.6 References

[1]. D. P. Woodruff and T. A. Delchar, Modern Techniques of Surface Science. `: Cambridge Solid State Science Series, (1986).

[2]. Jesper Andersen, lecture notes,Lund university.

[3]. Justin Bogan PhD thesis, Dublin City University (2012).

[4]. http://eapclu.iap.tuwien.ac.at/~werner/images/t_exp_pho.gif

[5]. L. C. Feldman and W. Meyer, Fundementals of surface and thin film analysis. Elsevier Science Publishing Co. Inc.,(1986).

[6]. Brigggs and J. T. Grant, Surface Analysis by Auger and X-ray Photoelectron. IM Publications,(2003).

[7]. J.OH, J.C.CAMPBELL, Journal of ELEC.MATER, Vol.33, No.4, (2004).

[8]. Astrid Schematic [online] http://www.isa.au.dk/facilities/astrid/astrid.asp

[9]. R. T. Long PhD thesis, National University of Ireland, (2010).

[10]. Oxford instruments TC50 manual (Atomic Hydrogen Cracker).

[11]. E. H. Nicollian, J. R. Brews, MOS Physics and Technology, New York, Wiley, (1982).

3 Surface and interface characterization of Ge and InAs surfaces by photoemission spectroscopy

This chapter presents the effectiveness of selenium passivation on both germanium and InAs substrates at preventing the growth of interfacial oxides during MgO deposition. In addition, a comparison study between the thermal cleaning of the native oxide covered InAs(100) surface and atomic hydrogen cleaning has also been undertaken using soft x-ray photoemission spectroscopy

3.1 Interface formation between MgO and the atomically clean and selenium passivated Ge (100) surfaces.

Germanium has long been proposed as a suitable candidate material for high mobility p-type metal oxide semiconductor (p-MOS) devices primarily because of its high hole mobility. However, this advantage has been difficult to realize because of the problems associated with controlling germanium sub-oxide growth prior to and during high-k deposition. There have many studies of germanium based MOS devices with investigations of HfO_2 [1,2], HfSiO [3], Al_2O_3 [4], Er_2O_3 [5], La_2O_3 [6] and ZrO_2 [7] high-k dielectric layers with varying reports of the presence of interfacial germanium sub-oxides which impact on the electronic performance of the device. The removal of these sub-oxide states is essential to minimize the interface defect states and to decrease the overall equivalent oxide thickness (EOT) of the dielectric layer. A wide variety of surface preparation treatments including argon ion bombardment [8], wet chemical etching using hydrochloric acid (HCl) [9], hydrogen bromide (HBr) [10], hydrofluoric acid (HF) [11], ammonium hydroxide (NH_4OH) [12,13], sulphur (gas and liquid based) [14-16] treatments, silicon interlayers [17], nitridation (NH_3 treatment) [18,19], and fluorine incorporation [20] have been investigated in attempts to suppress germanium sub-oxide layer either at the surface or high-κ/Ge interface. In this study, synchrotron radiation based soft x-ray photoelectron spectroscopy (SXPS) was used to

characterize the chemistry of interface formation between MgO and the clean Ge(100) surface with and without the presence of an interfacial selenium layer. MgO was preferred as a dielectric material for this study as it known to grow epitaxially on the germanium surface and have sufficient band offsets to minimize the leakage currents [21]. Previous studies have shown that MgO lattice matched with germanium substrates offers high quality interfaces for application in spintronic devices [21-24]. However, x-ray photoelectron spectroscopy (XPS) studies have reported the presence of germanium sub-oxides at MgO/Ge interface [22]. Therefore, in this study the effectiveness of selenium passivation of the clean Ge(100) surface prior to dielectric deposition has been investigated. This approach is consistent with a recent XPS study which showed that the selenium passivation of atomically clean germanium is effective at suppressing sub-oxide formation upon exposure to molecular oxygen [25].

3.1.1Experimental

The soft x-ray photoemission experiments were carried out on the SGM1 beamline at the Astrid synchrotron light source in the University of Aarhus in an ultrahigh vacuum (UHV) system consisting of a preparation chamber ($5x10^{-10}$ mbar) and an analysis chamber ($2x10^{-10}$ mbar). The SCIENTA SES-200 electron energy analyzer collects photoelectrons over a solid angle of 8° centred at 40° from the direction of the incoming photons. All photoemission scans were taken at normal emission with respect to the sample position. The p-type Ge (100) samples (4×10^{17} cm^{-3}) were cleaned by a cyclic series of argon ion bombardment and anneals at 550^{o}C to remove the surface oxide and carbon contaminants from the surface. Insitu Se passivation was carried out by depositing a thick Se layer and annealing at 300^{o}C to remove the excess Se from the surface. MgO was subsequently deposited in a stepwise incremental fashion at room temperature by thermally evaporating Mg from a tantalum pouch in a

background oxygen partial pressure of 5 x 10^{-7} mbar followed by UHV anneal at 300^{o}C for 20 minutes to test the thermal stability of the high-κ/Ge interface. The photoemission spectra of Ge 3d, Mg 2p, Se 3d and the valence bands, were acquired at photon energies of 60 and 130eV where the total instrumental energy resolution was estimated to be 70 meV. In order to accurately determine the incident photon energy, core level spectra of the Ge 3d were acquired with both 1st and 2nd order light as the kinetic energy difference gives the precise photon energy. The Ge 3d core level peak was fitted with parameters such as Gaussian (Lorentzian) full width at half maxima (FWHM) of 0.32±0.02 eV (0.15±0.02 eV) and a branching ratio and spin-orbit-splitting of 0.61 and 0.59 eV, respectively, consistent with previous reports [26].

3.1.2 MgO deposition on Se passivated Ge surface

Figure 3.1 displays the Ge 3d core level spectra acquired at 60 eV photon energy for the atomically clean Ge(100) surface, following selenium passivation and subsequent MgO deposition and anneal. The Ge 3d clean surface signal can be curve fitted with four spin orbit split doublet peaks attributed to up dimer atoms, down dimer atoms, a second surface layer and a bulk derived components [26]. The bulk and surface component appears at 29.73 eV and 29.48 eV binding energy, the up dimer and down dimer atom shifted to 0.19 eV lower and 0.59 eV higher binding energy, respectively, from the bulk peak consistent with the previous studies [26]. The down dimer atom is shifted 0.78 eV to higher binding energy with respect to the up dimer atom suggesting charge transfer from the up to down dimer atoms similar to the charge shifts observed by Goldoni et.al [26] and Patthey et.al [27]. Selenium passivation of the clean germanium surface shows the attenuation of the dimer signals and the appearance of a new component peak shifted 0.63 eV to higher binding energy indicative of a

Ge-Se bonding interaction as the selenium has higher electronegativity than germanium. A similar higher binding shifted component was also reported for the interaction of sulphur with the germanium surface [28].

Subsequent MgO deposition results in the appearance of a low binding energy peak shifted by 0.67 eV from the Ge 3d substrate peak suggesting a bonding interaction between the deposited Mg and the Ge surface as has been observed for Mg interactions with the silicon

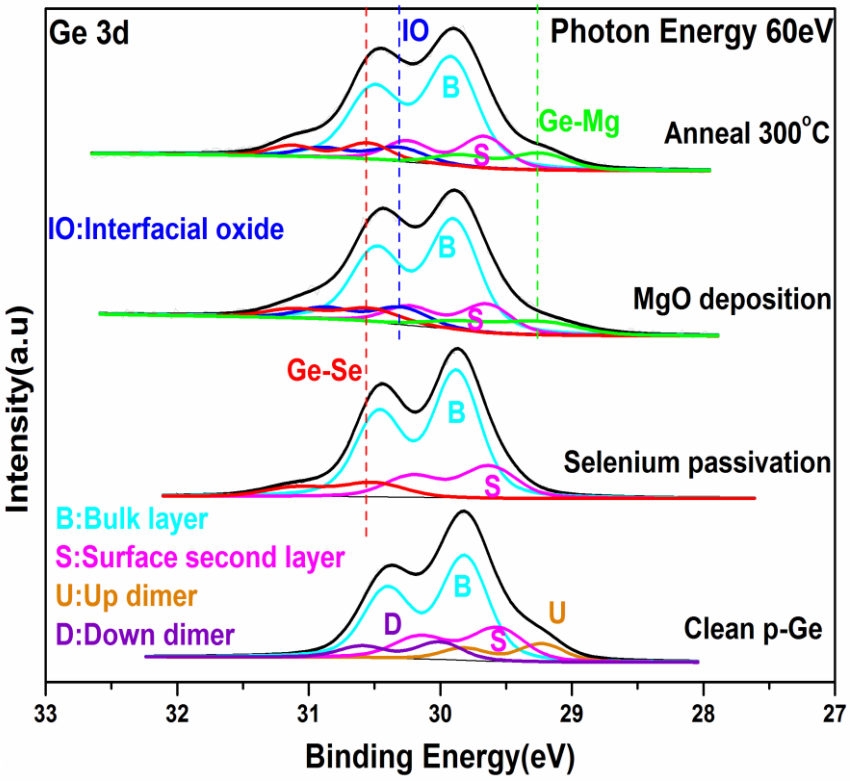

Figure 3.1: Ge 3d core level spectra taken at 60eV for the atomic clean Ge(100) surface, the selenium treated surface following MgO deposition and anneal.

surface [29]. An additional component peak shifted by 0.4 eV to higher binding energy of the bulk peak is also observed indicative of a limited bonding interaction with oxygen. The estimated thickness of the MgO dielectric film was approximately 1.0 nm as determined by the attenuation of the Ge substrate signal by the overlayer. Annealing this surface at 300^{o}C showed no significant impact on the peak profile suggesting that the interface is thermally

stable at this temperature and no evidence of selenium diffusion into the MgO layer was observed.

3.1.3 MgO deposition on atomically clean Ge surface

Figure 3.2 shows the Ge 3d core level spectra for the deposition and anneal of a similar thickness MgO layer deposited onto the atomically clean Ge(100) surface. MgO deposition results in a significant increase in intensity on the higher binding energy side of the Ge 3d peak compared to selenium treated germanium surface and is attributed to the growth of interfacial sub-oxides which can be curve fitted with three distinct Ge oxidation states shifted

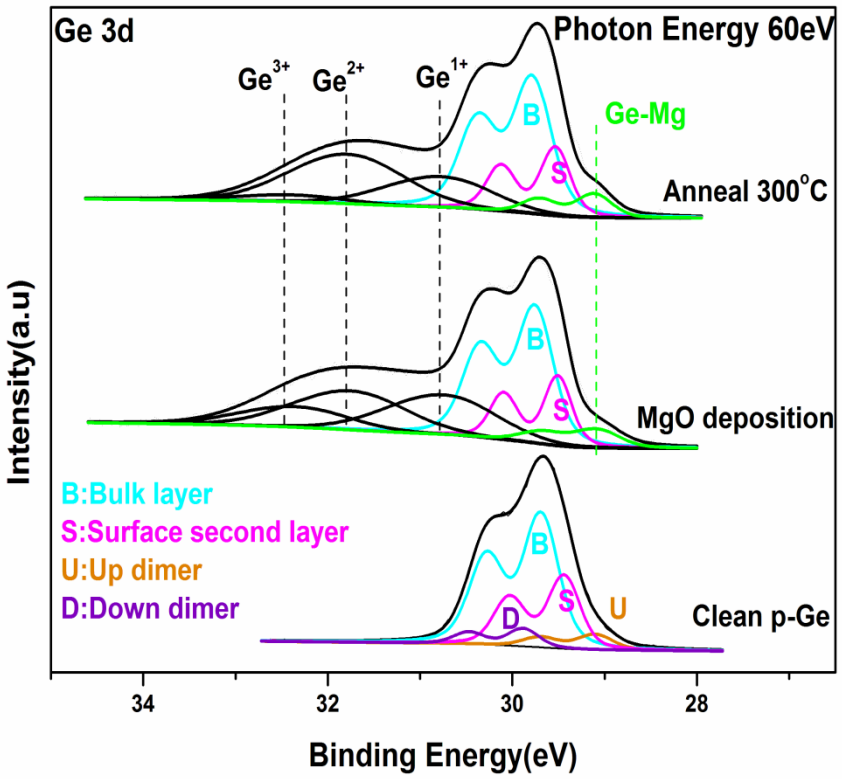

Figure 3.2: Ge 3d core level spectra taken at 60eV for the atomic clean Ge(100) surface following MgO deposition and anneal.

by 0.8 eV, 1.8 eV and 2.6 eV to higher binding energy. These chemical shifts are consistent with the presence of Ge^{1+} (Ge_2O), Ge^{2+} (GeO) and Ge^{3+} (Ge_2O_3) oxidation states as previously reported [30]. These results contrast with the recently reported XPS studies by Jeon et.al [21], for the molecular beam epitaxial (MBE) growth of MgO on the clean Ge

surface which observed no evidence of interface oxidation. However, by acquiring the Ge 3d spectra at 60 eV as opposed to the conventional Mg kα x-ray source photon energy the surface sensitivity is significantly increased. A low binding energy component peak shifted by 0.62 eV from the bulk peak is also observed similar to the Se passivated surface and is indicative of a Ge-Mg bonding interaction. Subsequent annealing at 300^{o}C results in the partial transformation of Ge sub-oxides to GeO and similar results has also been reported after annealing native oxide covered germanium surface [30].

3.2 Investigation of MgO on selenium passivated InAs surface

For the development of complementary metal oxide semiconductor (CMOS) devices beyond the 22 nm technology node, III-V transistor channel materials such as InAs have been proposed as potential candidates due to their high electron mobility. However, the growth of poor quality interfacial oxides upon high-k dielectric deposition makes it difficult to fabricate high quality interfaces. Previous reports suggest that Fermi level pinning behaviour, which results in difficulty in inverting the channel, can be attributed to the presence of interfacial oxides at the high-k/III-V interface [31,32]. Therefore, preparation of an oxide free interface is an important prerequisite for the reduction of the defect state density. Many cleaning procedures have been suggested including sulphur passivation [33] and tri-methyl aluminium treatment (TMA) [34], HCl cleaning [34,35], low energy ion sputtering [36,37], molecular hydrogen cleaning (MHC) [38,39] and atomic hydrogen cleaning (AHC) [40,41] to prepare oxide free III-V surfaces. The preservation of the stoichiometry of the InAs surface after wet or dry cleaning treatment is also important as changes can have a severe impact on Fermi level pinning [42]. Sugata et.al [43] suggested an atomic hydrogen cleaning method to prepare oxide free GaAs surface without any stoichiometric change in the surface composition. In addition to the surface cleaning step, passivation strategies for the III-V channel materials before high-k deposition need to be developed in order to control the

interfacial oxide growth. Previous studies suggest that selenium passivation on the germanium surface can effectively suppress the oxide formation upon molecular oxygen exposure [25]. Selenium treatment of III-V surfaces has also been reported [44,45] but the chemical stability towards oxygen has not been well explored which motivates this study of interface formation during high-k deposition. MgO has been chosen as a high-k gate material as it has a large band gap (~ 7.6 eV) which ensures sufficient band offsets [46] as described by Robertson [47] to minimize the carrier injection into the bands. It has also been reported to form abrupt interfaces with silicon [48] and germanium substrates [21]. Therefore, in this study an atomic hydrogen cleaning procedure has been used in the preparation of a clean InAs surface. An insitu selenium passivation treatment was then performed in an attempt to control the interfacial oxide growth during subsequent high-k deposition. High surface sensitivity synchrotron radiation based soft x-ray photoelectron spectroscopy (SXPS) has been used to characterize the interface formation between the deposited MgO and the selenium treated InAs(100) surface.

3.2.1 Sample preparation

Native oxide covered n-InAs(100) samples (5×10^{17} cm^{-3}) were loaded without any pre-cleaning into an ultra-high vacuum chamber with a base pressure of 1×10^{-10} mbar. The photoemission experiments were carried out on the SX700 beam line at the ASTRID synchrotron in Aarhus University, Denmark. The samples were subjected to an atomic hydrogen beam generated by an Oxford Research thermal cracker while been held at 360^{o}C for 90 mins to produce an atomically clean InAs surface [49]. Insitu Se passivation was carried out by thermally evaporating Se onto the InAs surface at room temperature and annealing at 300^{o}C to remove un-bonded excess selenium. Subsequently, MgO was deposited insitu at room temperature by thermally evaporating Mg in an oxygen partial pressure of $5x10^{-7}$ mbar in a sequential fashion as reported previously [50], and the sample was vacuum

annealed at 300°C for 20 minutes. The photoemission spectra of As 3d, In 4d, VB, Mg 2p, Se 3d, O 1s and C 1s core levels were acquired at photon energies ranging from 69eV to 600 eV. The As 3d (In 4d) peak profile was fitted with a doublet ratio of 0.66 (0.67), spin-orbit-splitting of 0.7 eV (0.85 eV), Gaussian width of 0.72±0.02 eV (0.73±0.01 eV) and Lorentzian width of 0.07 eV (0.2 eV), consistent with reported values [51,52]. The As 3d and In 4d core level spectra were measured at photon energies of 69 eV and 92 eV to get a comparable sampling depth of approximately 2 nm. The total instrumental energy resolution was estimated to be 0.7 eV at these photon energies. Work function changes were measured by collecting the secondary photoemitted electrons while the sample was biased -9 V by a battery.

3.2.2 Results and discussion

Figures 3.3 and 3.4 display the In 4d and As 3d curve fitted peak profiles for the atomic hydrogen cleaned InAs (100) surface and following the subsequent Se and MgO depositions and anneal.

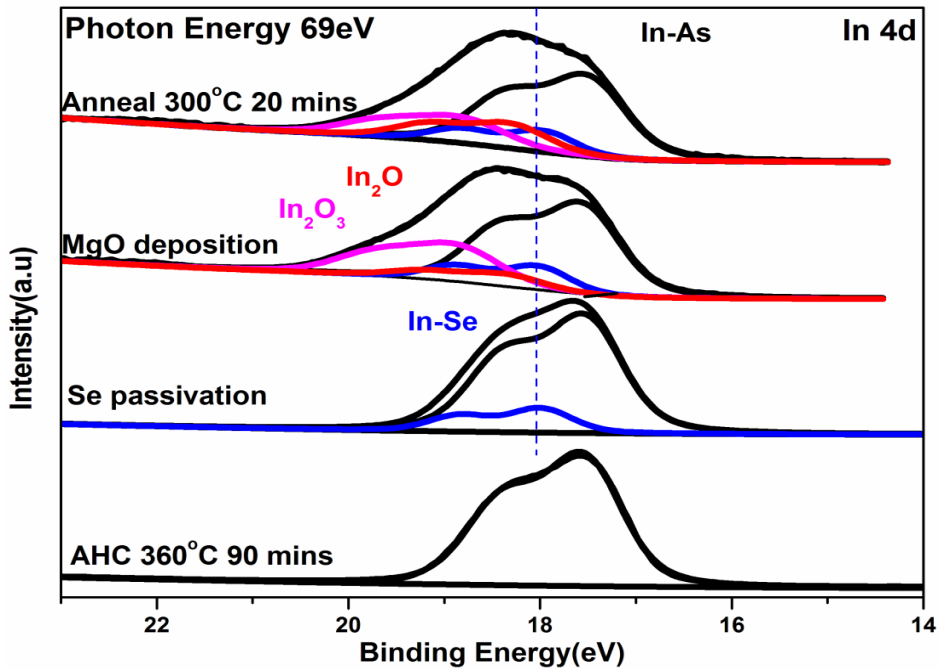

Figure 3.3: In 4d core level spectra taken at 69 eV for atomic hydrogen cleaned InAs, selenium passivation, MgO deposition and anneal at 300°C.

An atomically clean InAs(100) surface was prepared by exposing the native oxide covered surface to a beam of atomic hydrogen at 360^{o}C for 90 mins which produced an In rich surface consistent with previous studies [40,41]. The subsequent selenium deposition results in the appearance of a chemically shifted In 4d component at 0.47 eV high binding energy from the bulk In 4d peak at 17.5 eV attributed to a selenium bonding interaction. MgO deposition on this surface increased the intensity on the higher binding energy side of the bulk In 4d peak which was curve fitted with two distinct In oxidation states shifted by 0.4 eV and 1.3 eV to higher binding energy consistent with the presence of In_2O and In_2O_3 chemical species as previously reported [51,53,54]. This would indicate that the Se layer was unable to prevent the oxidation of the In at the MgO/InAs interface which contrasts with our previous study of MgO/Ge (100) interface formation where selenium passivation was effective at suppressing interfacial oxide growth. Annealing the MgO/InAs sample at 300^{o}C resulted in an attenuation of In_2O_3 signal however, a slight increase in the In_2O signal is observed suggesting the partial transfer of oxygen from the higher oxidation state.

As illustrated in figure 3.4, selenium deposition on the atomic hydrogen cleaned InAs surface shows no evidence of a bonding interaction with arsenic confirming that the surface is primarily In terminated. This is similar to the observation by Petrovykh et al [33] who reported that for an XPS study of the ammonium sulphide passivated InAs (100) the sulphur exclusively bonded to indium. The selenium treatment of the Ga rich GaAs surface also reported the observation of Ga-Se bond formation and an absence of any As-Se interaction [55]. Subsequent MgO deposition results in no evidence of As oxidation again consistent with the In rich nature of the clean InAs surface. The appearance of an additional low binding energy component shifted by 0.64 eV is attributed to the formation of arsenic dangling bonds which originated following the oxidation of the surface indium to form In_2O and In_2O_3. The thickness of MgO dielectric film was estimated to be approximately 1.2 nm from the

attenuation of InAs substrate signal by the oxide layer. The spectra shown in figure 3.5 for the atomically clean InAs surface and following selenium treatment indicate that the As 3d core level intensity decreases relative to the In 4d signal following selenium deposition from an intensity ratio of 0.3 to 0.2 reflecting the replacement of As by Se in the near surface region. Similar arsenic replacement processes was observed upon selenium treatment of InAs surface [56] and for InGaAs after sulphur passivation [57].

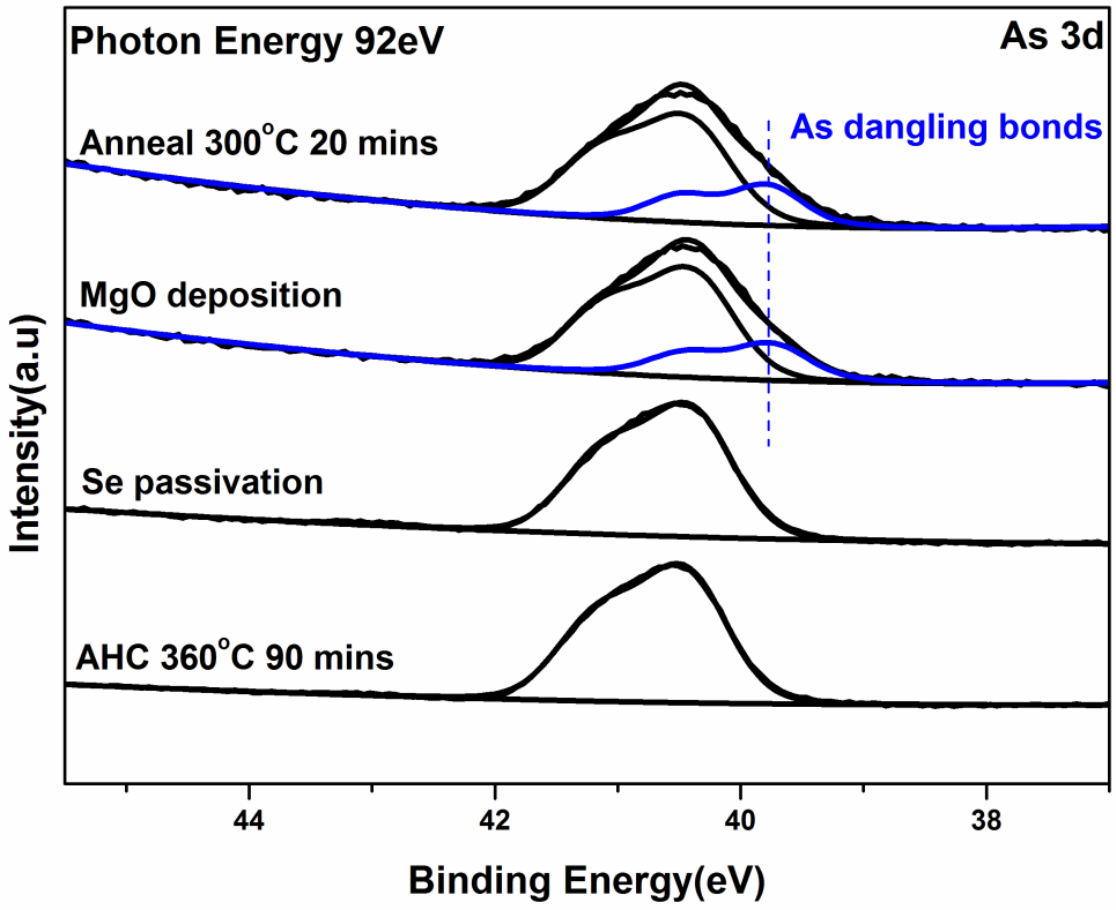

Figure 3.4: As 4d core level spectra taken at 92eV for, atomic hydrogen cleaned InAs, selenium passivation, MgO deposition and anneal at 300°C.

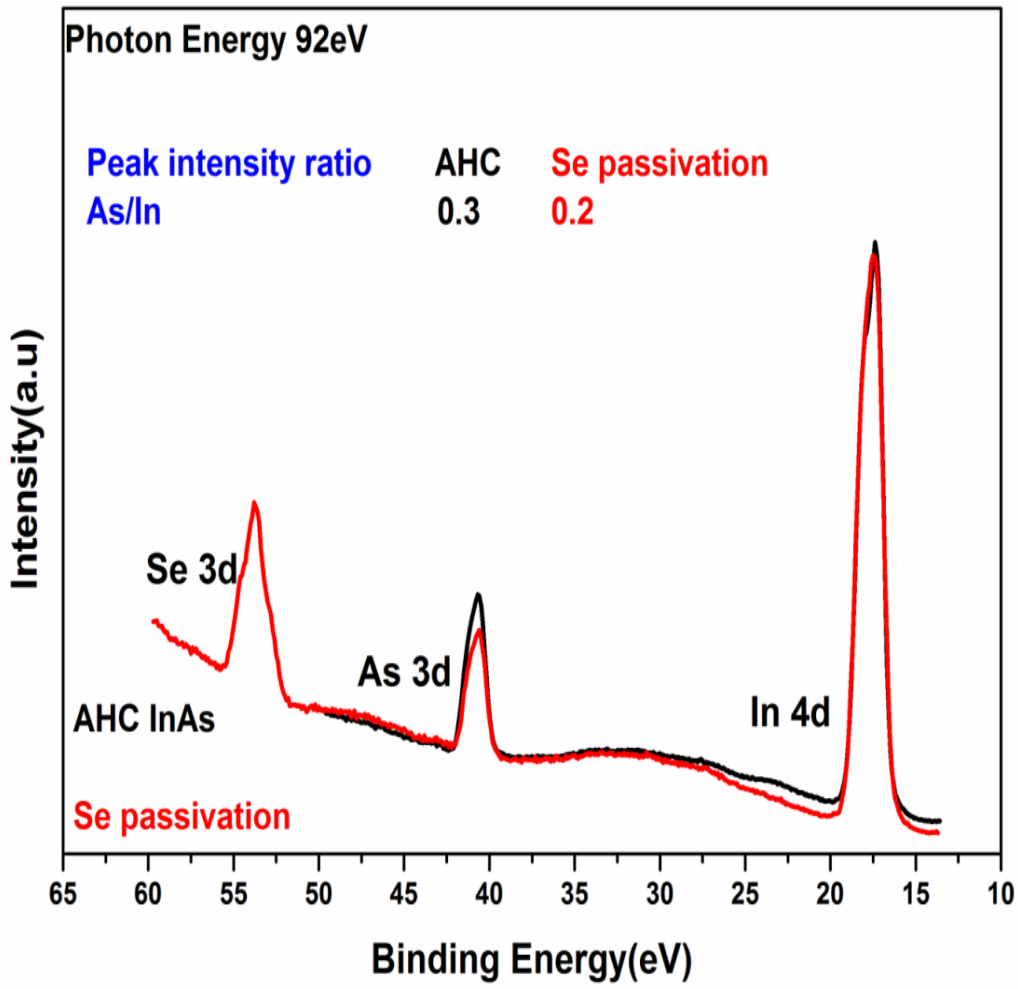

Figure 3.5: Spectra consisting of In 4d, As 3d and Se 3d core levels for both the atomic hydrogen cleaned and selenium terminated InAs surface showing the change in ratio of the In:As following Se deposition. The spectra have been normalised to the same In 4d peak intensity.

The O 1s spectrum following MgO deposition shown in figure 3.6 displays two chemically shifted components separated by 2.22 eV with the lower binding energy peak at 530.94 eV assigned to MgO and the higher binding energy peak at 533.16 eV to indium interfacial oxides which re-grow during the early stages of MgO deposition. Confirmation that the higher binding energy component is related to these interfacial oxides is obtained from a significant reduction in the intensity of this peak following the thermal annealing step.

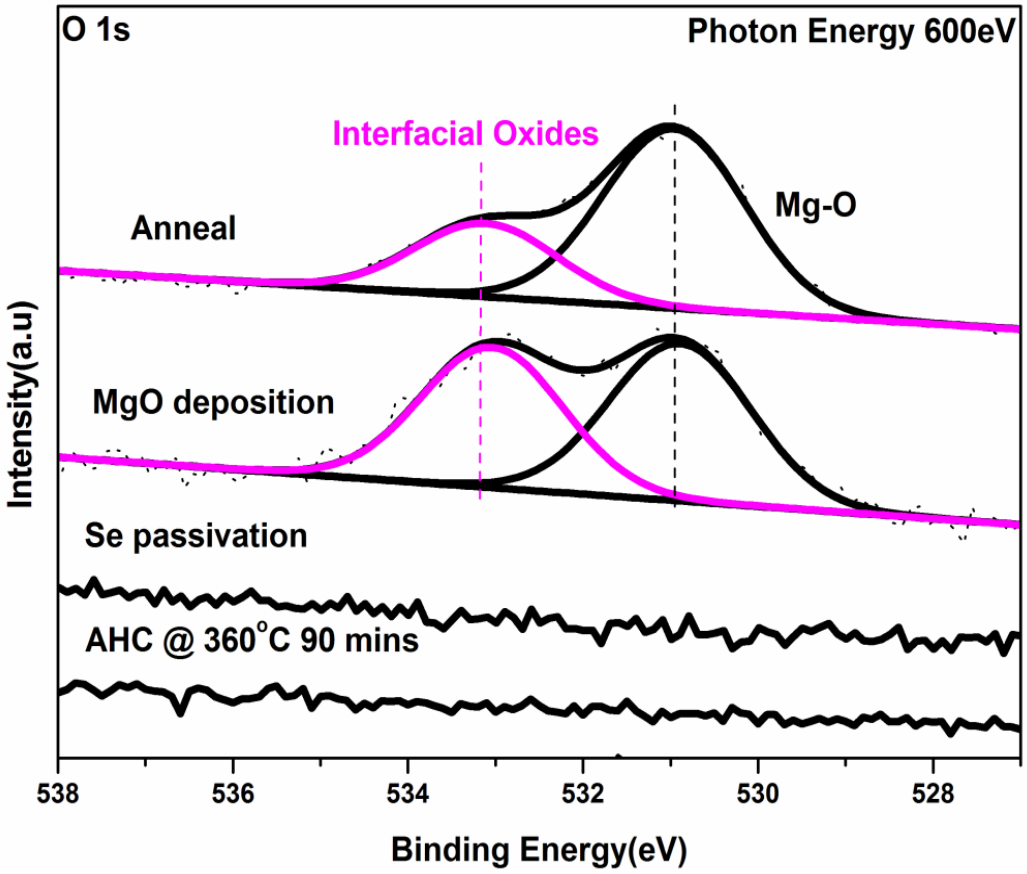

Figure 3.6: O 1s core level spectra acquired at 600 eV for the atomic hydrogen cleaned InAs, selenium passivation following MgO deposition and anneal.

Work function measurements which reflect the changes in electronic properties of the surface are shown in figure 3.7 for the experimental sequence. The clean InAs surface following the atomic hydrogen treatment results in a low energy cut off value of 4.49 eV consistent with the unrelaxed ideal InAs surface [58]. Selenium deposition resulted in an increase in work function to 5.32 eV suggesting the formation of a surface dipole layer due to the presence of the electronegative selenium. This is similar to the change in work function reported for the sulphur treatment of the atomically clean InGaAs surface [57]. The decrease in work function following MgO deposition to 3.15 eV reflects the suppression of the surface dipole by the

MgO layer towards the expected value for a thick MgO film while the subsequent annealing increases work function which may be due to densification of the MgO layer.

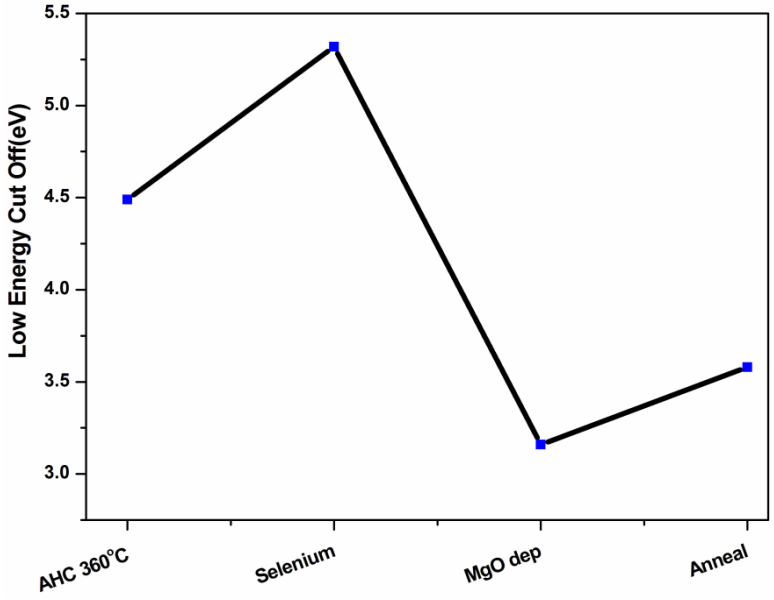

Figure 3.7: Work function measurements during the formation of MgO/Se/InAs structure.

3.2.2.1 Energy band offset MgO/Se/InAs structure

The conduction and valence band offsets were calculated from the valence band spectra taken at 69 eV using the proposed method by Kraut et al [59]. The measured valence band spectra are shown in figure 3.8 for atomically clean InAs surface, selenium passivated surface and following MgO deposition.

The valence band edge of the atomic hydrogen cleaned InAs surface is 0.8 eV below a metallic reference Fermi level in contact with the sample. Given that the bandgap for InAs is 0.36 eV, this would suggest that the Fermi level in the InAs is 0.44 eV above the conduction band edge in agreement with other studies which suggest the formation of a natural accumulation layer on the InAs surface [60,61]. The Fermi level position remains unchanged

following selenium deposition indicating no significant effect on the surface states consistent with the selenium treatment on GaAs surface [55].

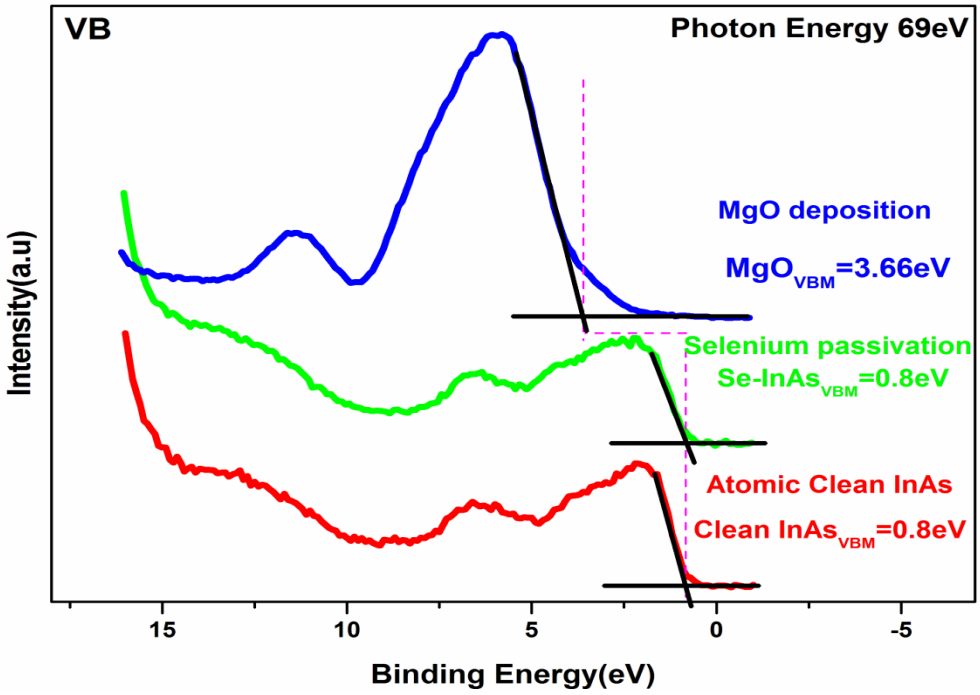

Figure 3.8: Valence band spectra acquired at 69 eV photon energy for the clean InAs surface, following selenium passivation and MgO deposition. Estimated uncertainty during the extraction of valence band minimum using linear interpolation method ±0.1eV.

MgO deposition allows the valence band maximum of the MgO layer to be identified relative to the InAs valence band edge. As suggested by Robertson [47] the band offsets should be over 1 eV to minimise the hole or electron injection into the dielectric oxides. The band offset values are calculated using the following equation 3.1[59].

$$\Delta E_V = \Delta E_{CL} + \left(E_{CL}^{InAs} - E_{VBM}^{InAs}\right) - \left(E_{CL}^{Oxide} - E_{VBM}^{Oxide}\right) \qquad 3.1$$

Where ΔE_{CL} is the binding energy separation between the oxide and As 3d core level peak estimated as 10.4 eV. The $\left(E_{CL}^{InAs} - E_{VBM}^{InAs}\right)$ and $\left(E_{CL}^{MgO} - E_{VBM}^{MgO}\right)$ terms are the binding energy difference between As 3d core level spectra and the valence band maximum (VBM) calculated to be 40 eV and the Mg 2p core level peak to MgO VBM determined to be 47.5 eV. The valence band offset can be calculated by substituting the appropriate values in equation 3.1 and the conduction band offset can be obtained by using the valence band offset, the known band gap of the MgO layer and InAs substrate as shown in equation 3.2.

$$\Delta E_C = E_g(MgO) - E_g(InAs) - \Delta E_V \qquad 3.2$$

Klau et.al [34] have reported that the MgO band gap increases from 5.6 eV to 7.6 eV as a function of thickness from 2 to 6 monolayers (ML). As the MgO thickness in this experiment was estimated to be 1.2 nm (~ 6 ML) it is assumed that the band gap of MgO is 7.6 eV at room temperature. Therefore the estimated valence band and conduction band offsets are 2.9 eV and 4.34 eV, respectively, and are illustrated in the schematic energy band diagram shown in figure 3.9. Thus ensures the required band offsets are present to inhibit the electron or hole injection into the oxide band.

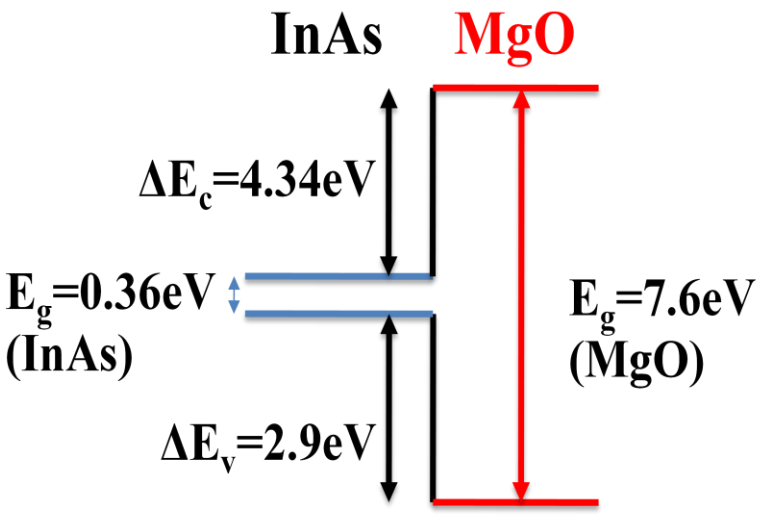

Figure 3.9: Schematic energy band diagram of MgO/Se/InAs structure.

3.3 Comparative study of thermal annealing and atomic hydrogen cleaning of InAs surfaces

The use of atomic hydrogen (AH) as a method for oxide removal and surface cleaning of III-V semiconductors has been proposed due to the relatively low temperature needed to instigate the oxide removal, [62,63] which is important due to the low decomposition temperature of III-V semiconductor materials. This treatment has been used to prepare an atomically clean GaAs surface at $\leq 430^{o}$C without any residual surface oxides [64,65]. However, when the same cleaning procedure was studied on native oxide covered InGaAs, the complete removal of the surface oxides resulted in the loss of indium which could have implications for device operation, as majority carrier mobility in InGaAs scales with indium content [62]. Previous studies have shown the complete removal of surface oxides from both polar and non-polar InAs surfaces upon atomic hydrogen exposure around 400^{o}C substrate temperature using high resolution electron energy loss spectroscopy (HREELS) and Auger electron spectroscopy measurements [40,41] however, details of the surface chemical interactions were not investigated. In this study the changes in the surface chemical composition of the native oxide covered InAs surface up to an annealing temperature of 450^{o}C are compared with the atomic hydrogen cleaning at 360^{o}C using high surface sensitivity synchrotron radiation based soft x-ray photoemission spectroscopy.

3.3.1 Impact of vacuum annealing

The As 3d and In 4d core level spectra acquired from the native oxide covered InAs surface and following thermal vacuum annealing are shown in figures 3.10 and 3.11, respectively. The As 3d core level spectrum for the native oxide sample was curve fitted with four components consisting of a bulk As peak at 40.8 eV, an elemental As peak shifted 0.5 eV to higher binding energy and two oxidation states of arsenic As^{3+} (As_2O_3) and As^{5+} (As_2O_5)

shifted to 3.2 eV and 4.4 eV higher binding energy, respectively, consistent with previous assignments [51].

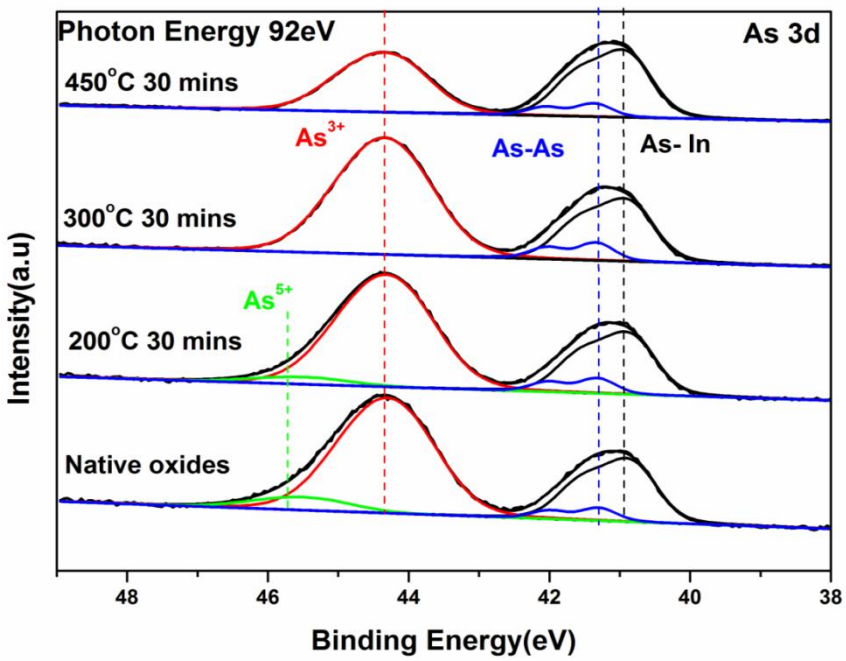

Figure 3.10: Curve fitted As 3d core level spectra acquired at 92 eV photon energy for the native oxide surface and the successive anneals up to 450°C.

Annealing at 300°C results in the complete attenuation of the As_2O_5 without any other significant difference observed in the other oxidation state intensities. Subsequent annealing at 450°C for 30 mins results in a significant attenuation of the As_2O_3 peak intensity as was reported for a similar study on InGaAs [51]. The Indium (In) 4d signal for the native oxide sample, shown in figure 3.11, was peak fitted with a bulk indium peak at 17.5 eV and a peak shifted to higher binding energy is attributed to oxidized indium [51,66]. Annealing up to 450°C results in the progressive reduction in the intensity of the In oxidation state, however, a considerable oxidized indium signal is still detected at the highest temperature anneal. The change in the intensity of both the As and In oxidation species as a function of successive anneals expressed as a ratio to the substrate signal intensities is plotted in figure 3.12.

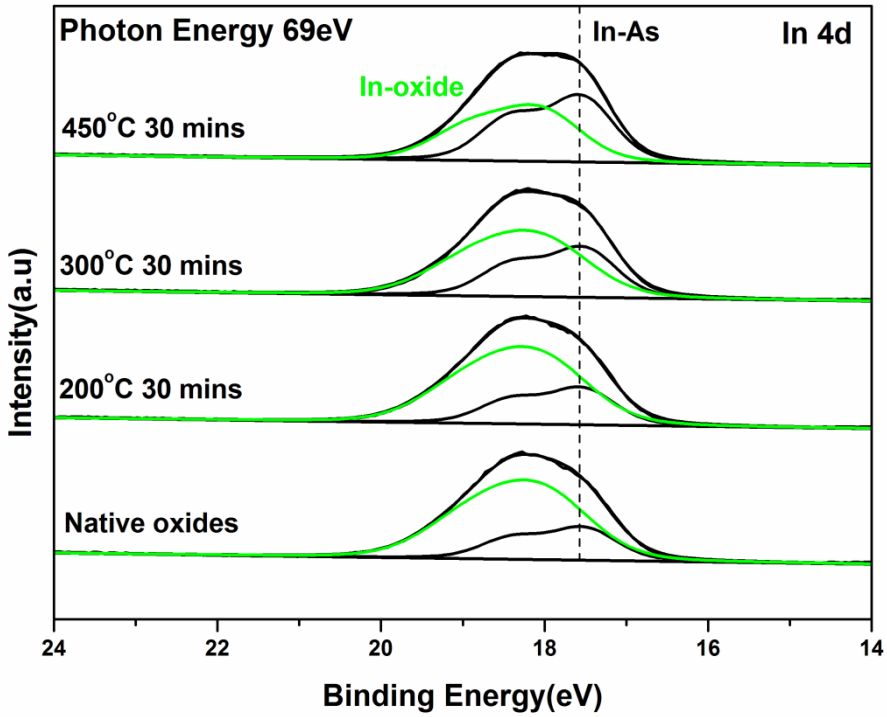

Figure 3.11: Curve fitted In 4d core level spectra acquired at 69 eV photon energy for the native oxide surface and the successive anneals up to 450°C.

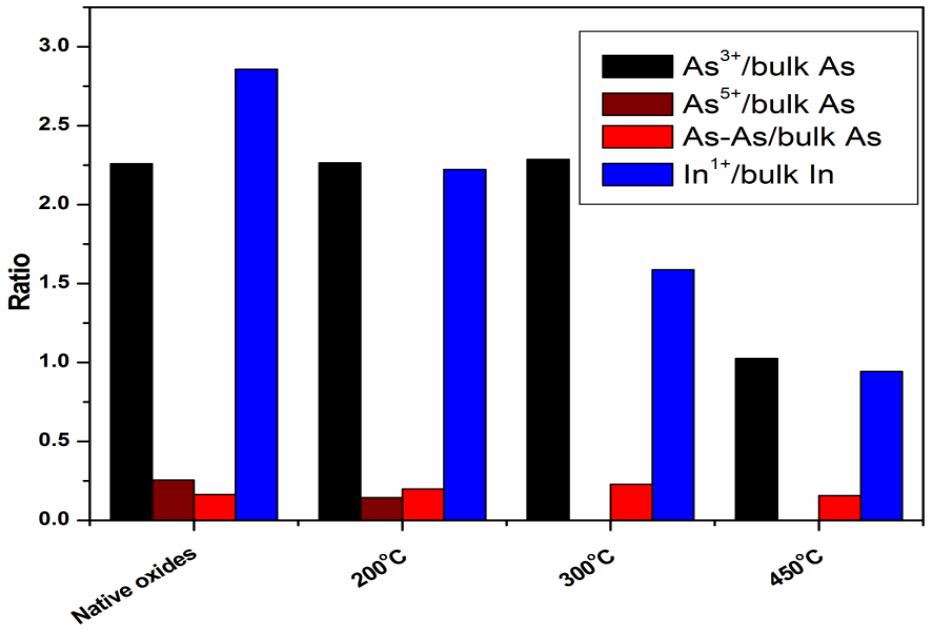

Figure 3.12: Ratio of arsenic oxidation states to bulk arsenic and indium oxidation state to bulk indium calculated from the As 3d at 92 eV and In4d at 69 eV for the native oxide surface and the subsequent annealing treatments.

This shows that the As^{5+} state is completely attenuated at 300°C and there is a corresponding increase in the intensity of As^{3+} and the elemental arsenic signals attributed to the partial loss of oxygen from the surface, as has been reported by Brennan et al [51] for the thermal anneal of native oxide covered InGaAs substrate. The presence of elemental arsenic and the As^{3+} state have been suggested as the cause of Fermi level pinning in high-κ/GaAs MOS devices [31,32,67,68]. At 450°C, As^{3+} state and elemental arsenic species have decreased in intensity, however there is still a significant amount present which is inconsistent with the reported desorption temperature of As^{3+} at 200°C [69]. The gradual attenuation of the oxidized indium signal suggests the relatively high thermodynamic stability of this oxide up to 450°C. Figures 3.13 displays the O 1s and C 1s signal of the native sample and the subsequent annealing at elevated temperatures. The FWHM of the O 1s signal for the native oxide sample 1.9 eV gradually decreases in width as a function of annealing treatments consistent with the reduction of arsenic and indium oxides and confirms that annealing at 450°C is not sufficient to completely remove the surface oxides.

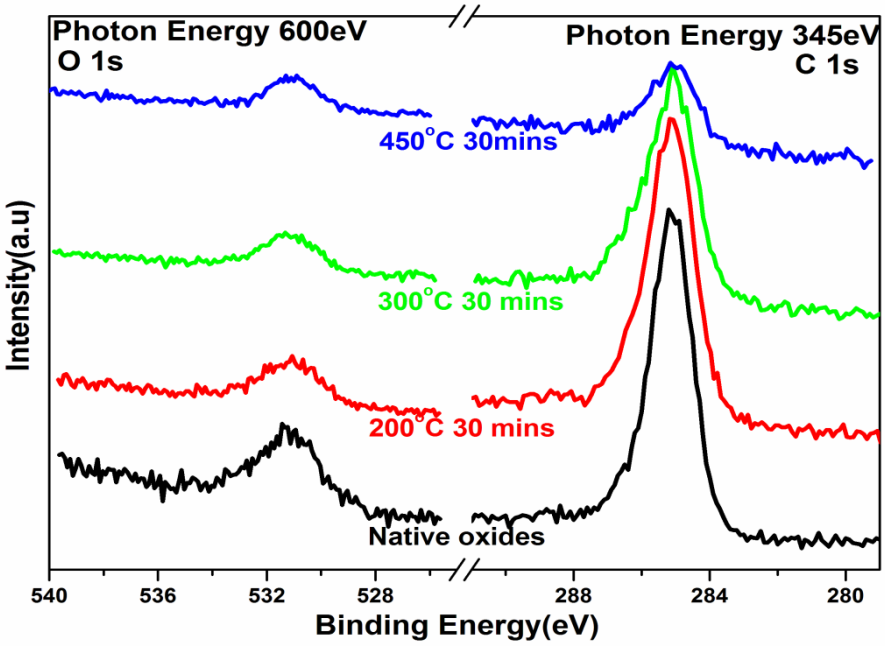

Figure 3.13: O 1s and C1s core level spectra acquired at 600 eV and 345 eV photon energies for the native oxide surface and following thermal anneals up to 450°C.

The C 1s signal shows a steady drop in peak intensity up to 450°C attributed to the desorption of carbon present on the surface but again, annealing at this temperature is insufficient to completely remove the carbon contamination.

3.3.2 Impact of Atomic Hydrogen Clean (AHC)

Figure 3.14 and 3.15 shows the peak fitted As 3d and In 4d core level spectra taken during the intermediate steps of the atomic hydrogen cleaning treatment. The As 3d and In 4d spectra for native oxide sample were fitted with the same fitting parameters as mentioned above.

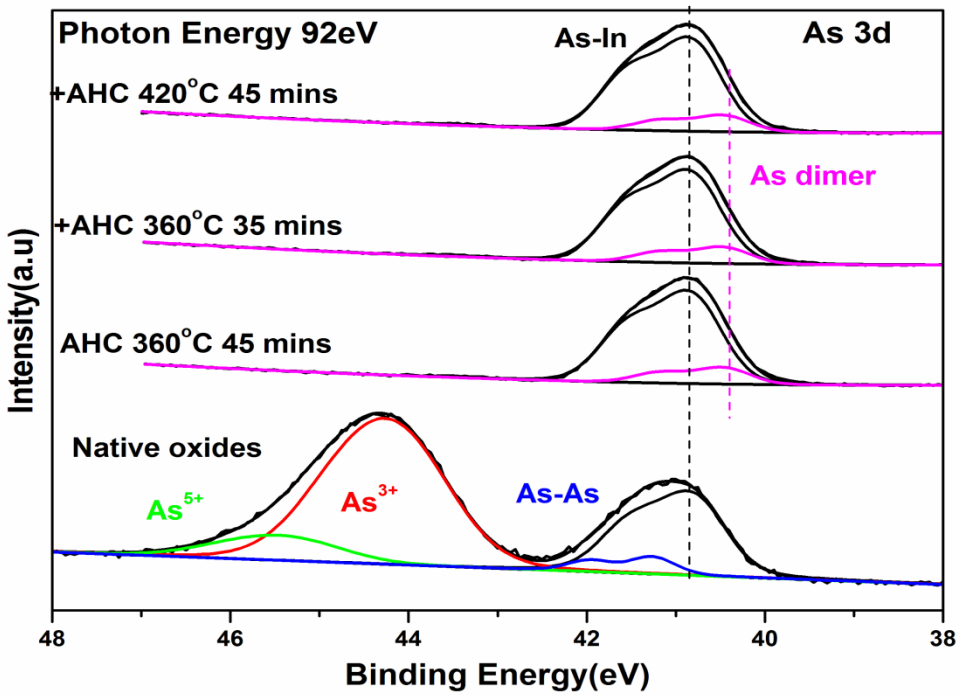

Figure 3.14: Curve fitted As 3d core level spectra acquired at 92 eV photon energy for the native oxide covered InAs surface and the subsequent atomic hydrogen exposure at substrate temperatures up to 420°C.

All detectable arsenic and indium oxides were completely removed after the first atomic hydrogen exposure at 360°C for 45 minutes. The bulk arsenic peak at 40.8 eV and the

additional peak shift to 0.5 eV lower binding energy is indicative of As dimer formation in agreement with Brennan et al [51]. The bulk indium signal from the substrate at 17.5 eV binding energy was fitted with a single spin-orbit-split component with no evidence for any elemental indium signal.

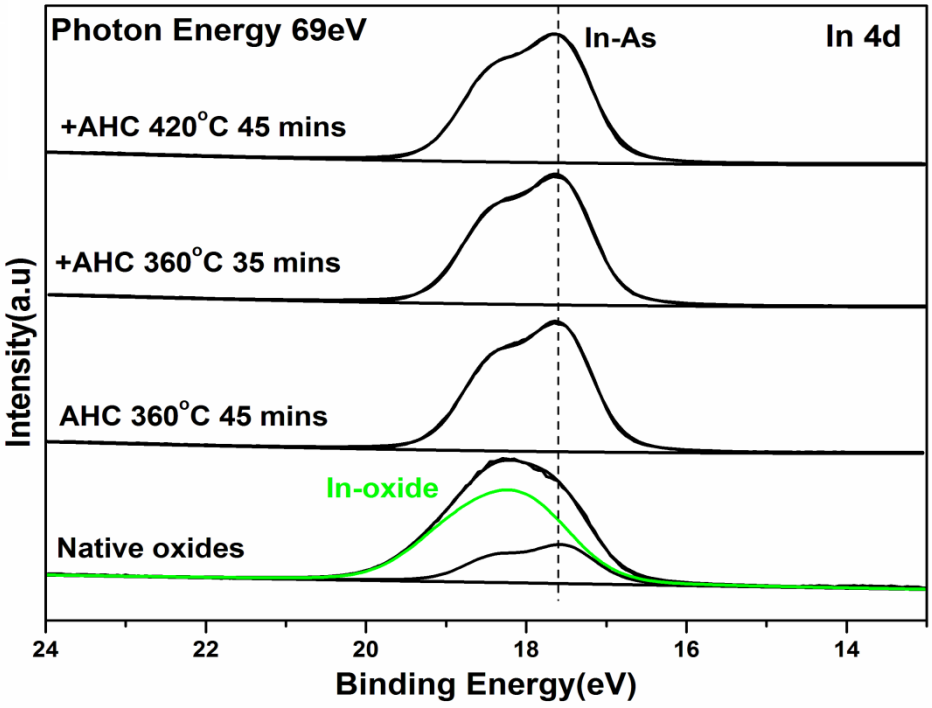

Figure 3.15: Curve fitted In 4d core level spectra acquired at 69 eV photon energy for the native oxide covered InAs surface and the subsequent atomic hydrogen exposure at substrate temperatures up to 420°C.

The reaction path for the atomic hydrogen cleaning of InAs has involves the hydrogen reduction of both the In and As surface localised oxides at elevated temperatures [40,62]. Further exposure of the InAs surface to atomic hydrogen at both 360°C for 35 mins and 420°C for 45mins resulted in no further change in the In or As peak intensities indicating that the surface composition remains constant after the oxide removal. This results contrasts with that reported for the atomic hydrogen clean of the InGaAs surface at 390°C which lead to the loss of indium from the surface [40].

The changes in the oxygen and carbon related signals following this atomic hydrogen treatment are shown in figures 3.16. While there is complete attenuation of the O 1s peak following the first clean, there is a small residual C 1s signal which is attenuated further with the higher temperature treatments.

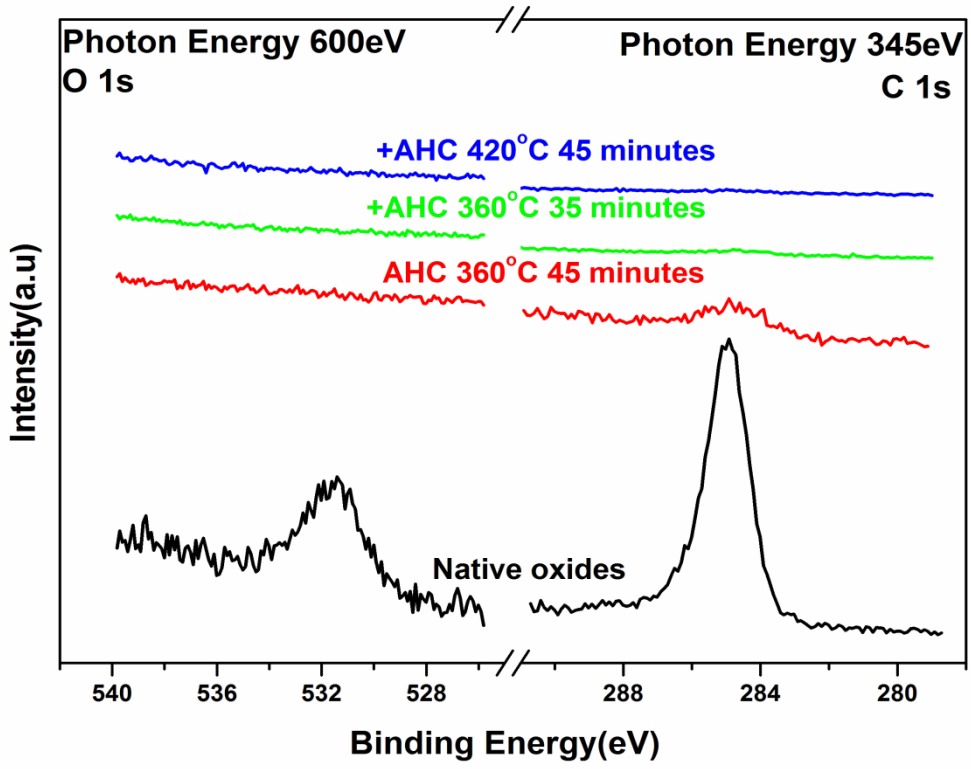

Figure 3.16: O 1s and C 1s core level spectra acquired at 600 eV and 345 eV photon energies for the native oxide covered InAs surface and the subsequent atomic hydrogen exposure at substrate temperatures up to 420°C.

The complete removal of carbon contamination can enhance the device performance as the presence of carbon has been suggested as contributing to the electrical degrade of metal oxide semiconductor (MOS) devices [70-72]. Bing et al [73] have also reported that variations in carbon contamination possibly alter the barrier height between metal electrode and high-κ dielectric layers.

3.3.2.1 Work function measurement

The work function measurement is a sensitive indicator of surface cleanliness and the changes in the measured value for the thermally treated surface are shown in figure 3.17(a). The native oxide work function measured at 3.73 eV and increased to 4.06 eV at 450^{o}C which is lower than the 4.55 eV [69] value reported for a clean InAs surface, consistent with the presence of residual oxides on the surface.

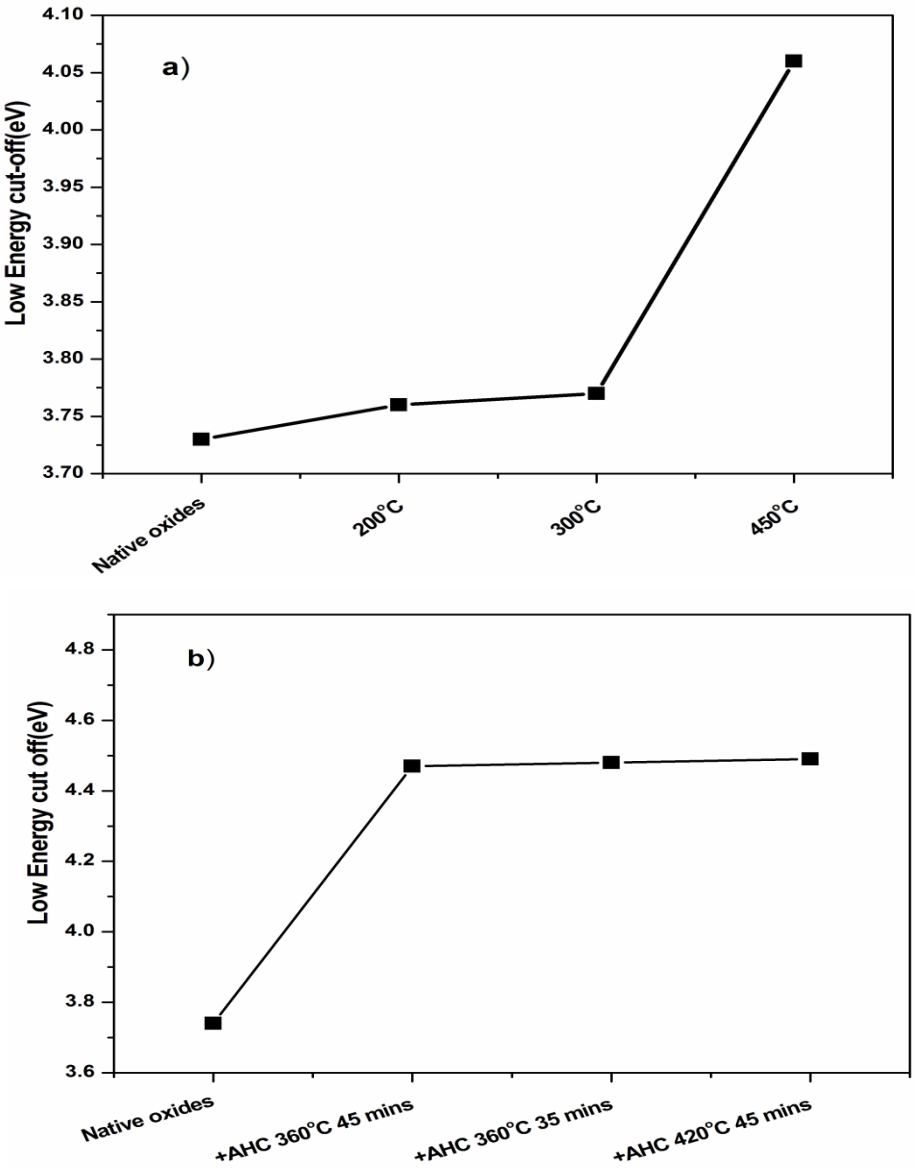

Figure 3.17: Work function changes for (a) the native oxide covered InAs surface and (b) the atomic hydrogen treated InAs surface with the thermal annealing treatments.

In figure 3.17(b), work function measurements for the atomic hydrogen exposure at 360^{o}C for 45 minutes show a sharp increase to 4.47 eV which is near to the 4.55 eV reported for the ideal InAs surface [69]. Further atomic exposure up to 420^{o}C result no significant change in work function suggest no surface compositional changes consistent with the photoemission results indicating the thermal stability of the cleaned InAs surface up to 420^{o}C.

3.4 Conclusion

The interface chemical stability of selenium in limiting interfacial oxide formation during MgO deposition on both high mobility Ge and InAs substrates has been investigated using high surface sensitivity synchrotron radiation based photoemission spectroscopy. This study displays the effectiveness of a selenium interlayer at preventing interface oxidation between the deposited MgO and the Ge surface promoting the formation of an abrupt interface which could have implications for pMOS device performance. However, room temperature selenium passivation of the atomic clean InAs surface has been shown to result in selenium substitution for arsenic in the near surface region and this passivation has been shown to be unable to prevent interfacial oxide growth upon subsequent MgO deposition. The magnitude of the calculated band offsets are such that they ensure sufficiently high barriers at the semiconductor-dielectric interface to inhibit the injection of carriers into the dielectric layer. Thermal annealing of native oxide covered InAs to 450^{o}C has been shown to be not effective at removing surface contamination or native oxides. Atomic hydrogen cleaning at the comparatively low temperature of 360^{o}C produced an oxide and carbon free surface which was indium rich. Thermal stability of the cleaned InAs surface was also investigated as a function of longer atomic hydrogen exposure suggesting no In or As desorption from the surface up to a temperature of 420^{o}C.

3.5 References

[1]. N. Wu, Q. Zhang, C. Zhu, C. Yeo, S. J. Whang, D. S. H. Chan, M. F. Li, B. J. Cho, A. Chin, D. Kwong, A. Y. Du, C. H. Tung and N. Balasubramanian, Appl. Phys. Lett. 84, 3741 (2004).

[2]. D. He, X. Cheng, D. Xu, Z. Wang, Y. Yu, Q. Sun and D. W. Zhang J. Vac. Sci. Technol. B 29, 01A802 (2011).

[3]. H. J. Na, J. C. Lee, D. Heh, P. Sivasubramani, P. D. Kirsch, J. W. Oh, P. Majhi, S. Rivillon, Y. J. Chabal, B. H. Lee and R. Choi. Appl. Phys. Lett. 93, 192115 (2008).

[4]. M. Jamil, J. Oh, M. Ramon, S. Kaur, P. Majhi, E. Tutuc, and S. K. Banerjee IEEE Elect. Dev. Lett. 31, 11 (2010).

[5]. T. Ji, T.X. Nie , J. Cui , Z.B. Fang, X.J. Yang, Y.L. Fan, Z.Y. Zhong, Z.M. Jiang.Thin Solid Films 520 3406,(2012).

[6]. J. Song, K. Kakushima, P. Ahmet, K. Tsutsui, N. Sugii, T. Hattori, and H. Iwai, Jpn. J. Appl. Phys. 46, 16, 376 (2007).

[7]. O. Bethge, C. Henkel, S. Abermann, G. Pozzovivo, M. Stoeger-Pollach, W.S.M. Werner, J. Smoliner, E. Bertagnolli, Appl. Surf. Sci. 258, 3444 (2012).

[8]. H. E. Farnsworth, R. E. Schlier, T. H. George and R. M. Burger J. Appl. Phys. 26, 252 (1955).

[9]. J. Kim, J. McVittie, K. Saraswat, Y. Nishi, S. Liu, and S. Tan: ECS Trans. 3, 1191 (2006).

[10]. Y. Moriyama, N. Hirashita, K. Usuda, S. Nakaharai, N. Sugiyama, E. Toyoda and S. Takagi, Appl. Surf. Sci. 256, 823, (2009).

[11]. T. Deegan, G. Hughes Appl. Surf. Sci.123-124, 66 (1998).

[12]. H. Okumura, T. Akane, S. Matsumoto Appl. Surf. Sci.125, 1125 (1998).

[13]. J. S. Hovis, R. J. Hamers, C. M. Greenlief, Surf. Sci. 440, 815 (1999).

[14]. T. Maeda, S. Takagi, T. Ohnishi, and M. Lippmaa, Mater. Sci. Semicond. Process. 9, 706 (2006).

[15]. S. Sioncke, H. C. Lin, G. Brammertz, A. Delabie, T. Conard, A. Franquet, M. Meuris, H. Struyf, S. De Gendt, M. Heyns, C. Fleischmann, K. Temst, A. Vantomme, M. Müller, M. Kolbe, B. Beckhoff and M. Caymax, J. Electro. Chem. Soc. 158 687–92 (2011).

[16]. J Roche, P Ryan, G. J. Hughes, Appl. Surf. Sci. 174,271 (2001).

[17]. N. Wu, Q. Zhang, C. Zhu, D. S. H. Chan, A. Du, N. Balasubramanian, M. F. Li, J. Sin and D. Kwong, IEEE Electron Device Lett. 25, 631 (2004).

[18]. T. Maeda, T. Yasuda, M. Nishizawa, N. Miyata, Y. Morita and S. Takagi Appl. Phys. Lett.85, 3181 (2004).

[19]. N. Wu, Q. Zhang, C. Zhu, C.C Yeo, S. J. Whang, D. S. H. H. Chan, M. F. Li and B. J. Cho, Appl. Phys. Lett. 84 3741, (2004).

[20]. R. Xie, M. Yu, M. Y. Lai, L. Chan, C. Zhu, Appl. Phys. Lett. 92, 163505 (2008).

[21]. K. Jeon, S. Lee, C. Park, H. Lee and S. Shin, Appl. Phys. Lett. 97, 111910 (2010).

[22]. D. Petti, M. Cantoni, C. Rinaldi, S. Brivio, R. Bertacco, J. Gazquez, and M. Varela J. Appl. Phys. 109, 084909 (2011).

[23]. K. R. Jeon, C. Y. Park, and S. C. Shin, Cryst. Growth Des. 10, 1346 (2010).

[24]. Y. Zhou, W. Han, Y. Wang, F. Xiu, J. Zou, R. K. Kawakami, and K. L. Wang, Appl. Phys. Lett. 96, 102103 (2010).

[25]. D. Tsoutsou , Y. Panayiotatos, S. Galata, A. Sotiropoulos, G. Mavrou, E. Golias and A. Dimoulas, Microelectronic Eng.88, 407 (2011).

[26]. A. Goldoni, S. Modesti; V. R. Dhanak, M. Sancrotti, M. Santoni, Phys. Rev. B ,54,11340 (1996).

[27]. L. Patthey, E. L. Bullock, T. Abukawa, S. Kono and L. S. O. Johansson, Phys. Rev. Lett. 75, 2538 (1995)

[28]. X. Bai-Qing, C. Hu-Dong, S. Bing, W. Sheng-Kai, L. Hong-Gang, Chin. Phys. Lett. 29, 4, 046801 (2012).

[29]. K. S. An, R. J. Park, J. S. Kim, C. Y. Park, C. Y. Kim, J. W. Chung, T. Kinoshita and A. Kakizaki, Journal of Elect. Spec. and Rel. Phen. 80, 165-168 (1996).

[30]. J. Oh, J. C. Campbell Journal of Elect. Mater. 33, 364-367 (2004).

[31]. M. L. Huang, Y. C. Chang, C. H. Chang, Y. J. Lee, P. Chang, J. Kwo, T. B. Wu, and M. Hong, Appl. Phys. Lett. 87, 252104 (2005).

[32]. Y. C. Chang, M. L. Huang, K. Y. Lee, Y. J. Lee, T. D. Lin, M. Hong, J. Kwo, T. S. Lay, C. C. Liao and K. Y. Cheng, Appl Phys. Lett. 92, 072901 (2008).

[33]. D.Y. Petrovykh, M. J. Yangb, L. J. Whitman. Surface science 523, 231-240 (2003).

[34]. H. Trinh, E. Y. Chang, Y. Wong, C. Yu, C. Chang, Y. Lin, H. Nguyen, and B. Tran Jpn. J. Appl. Phys. 49, 111201 (2010).

[35]. O.E. Tereshchenko, D. Paget, A. C. H. Rowe, V. L. Berkovits, P. Chiaradia, B.P. Doyle, S. Nannarone, Surf. Sci. 603, 518–522 (2009).

[36]. V. Martinelli, L. Siller, M. Garzia Betti, C. Mariani, and U. del Pennino, Surf. Sci. 391, 73 (1997).

[37]. I. Aureli, V. Corradini, C. Mariani, E. Placidi, F. Arciprete, and A. Balzarotti, Surf. Sci. 576, 123 (2005).

[38]. Y. Lyadov, R. Akhvlediani, A. Hoffman, O. Klin and E. Weiss J. Appl. Phys. 107, 053518 (2010) .

[39]. C. -L. Chang, V. Shuttanadan, S. C. Singhal, and S. Ramanathan, Appl. Phys. Lett. 90, 203109 (2007).

[40]. G. R. Bell, N. S. Kaijaks, R. J. Dixon, C. F. McConville Surf. Sci. 401, 125–137 (1998).

[41]. T. D. Veal and C. F. McConville. Appl. Phys. Lett. 77, 1665 (2000).

[42]. H. Lin, S. Wu, C. Cheng, C. Ko, C. Wann, Y. Lin, S. Chang and T. Wu Appl. Phys. Lett. 98, 123509 (2011).

[43]. S. Sugata, A. Takamori, N. Takado, K. Asakawa, E. Miyauchi, and H. Hashimoto J. Vac. Sci. Technol. B 6, 1087 (1988).

[44]. C. J. Sandroff, M. S. Hegde, L. A. Farrow, R. Bhat, J. P. Harbison, and C. C. Chang J. Appl. Phys. 67, 586 (1990).

[45]. B. A. Kuruvilla, S. V. Ghaisas, A. Datta, S. Banerjee, and S. K. KulkarniJ. Appl. Phys. 73, 4384 (1993).

[46]. K. Jeon, S. Lee, C. Park, H. Lee, and S. Shin Appl. Phys. Lett. 97, 111910 (2010).

[47]. J. Robertson, Eur. Phys. J. Appl. Phys. 28, 265–291 (2004).

[48]. L. Yan, C.M. Lopez, R.P. Shrestha, E.A. Irene, A.A. Suvorova, M. Saunders, Appl.Phys. Lett. 88, 142901 (2006).

[49]. R. K. Chellappan, Z. Li, and G. Hughes. Applied Surface Science 276, 609 (2013).

[50]. B. Brennan, S. McDonnell and G.Hughes, J. Phys. Confer. Ser.100, 042047 (2008).

[51]. B. Brennan and G. Hughes J. Appl. Phys. 108**,** 053516 (2010).

[52]. G. Hollinger, R. Skheyta-Kabbani and M. Gendry, Phys. Rev. B 49, 11159–11167 (1994).

[53]. R. W. Hewitt and N. Winograd, J. Appl. Phys. 51, 2620 (1980).

[54]. H. Trinh, Y. Lin, H. Wang, C. Chang, K. Kakushima, H. Iwai, T. Kawanago, Y. Lin, C. Chen, Y. Wong, G. Huang, M. Hudait, and E.Y. Chang Appl. Phys. Exp. 5, 021104-021104 (2012).

[55]. .T.U. Kampen, D.R.T. Zahn, W. Braun, C. Gonza´lez, I. Benito, J. Ortega, L. Jurczyszyn, J.M. Blanco, R. Pe´rez, F. Flores, Appl. Surf. Sci. 212–213, 850–855(2003).

[56]. Y. Watanabe, F. Maeda, Appl. Surf. Sci. 117–118, 735–738 (1997).

[57]. L. Chauhan and G. Hughes J. Appl. Phys. 111, 114512 (2012).

[58]. W. Liu, W. T. Zheng, and Q. Jiang Phys. Rev. B. 75, 235322 (2007).

[59]. E. A. Kraut, R. W. Grant, J. R. Waldrop and S. P. Kowalczyk, Phys. Rev. Lett. 44, 1620–1623 (1980).

[60]. L. Ö. Olsson, C. B. M. Andersson, M. C. Håkansson, J. Kanski, L. Iver, and U. O. Karlsson, Phys. Rev. Lett. 76, 3626–3629 (1996).

[61]. J. R. Weber, A. Janotti, and C. G. Van de Walle, Appl. Phys. Lett. 97, 192106 (2010).

[62]. F. S. Aguirre-Tostado, M. Milojevic, C. L. Hinkle, E. M. Vogel, R. M. Wallace, S. McDonnell, and G. J. Hughes Appl. Phys. Lett. 92, 171906 (2008).

[63]. S. I. J. Ingrey, W. M. Lau, and R. N. S. Sodhi, J. Vac. Sci. Technol. A 7, 1554 (1989).

[64]. A. Khatiri, J. M. Ripalda, T. J. Krzyzewski, G. R. Bell, C. F. McConville, and T. S. Jones, Surf. Sci. 548, 134 (2004).

[65]. C. L. Hinkle, A. M. Sonnet, E. M. Vogel, S. McDonnell, G. J. Hughes, M. Milojevic, B. Lee, F. S. Aguirre-Tostado, K. J. Choi, J. Kim, and R. M. Wallace, Appl. Phys. Lett. 91, 163512 (2007).

[66]. R. Timm, A. Fian, M. Hjort, C. Thelander, E. Lind, J. N. Andersen, L.-E.Wernersson and A. Mikkelsen, Appl. Phys. Lett. 97, 132904 (2010).

[67]. R. Suri, D. J. Lichtenwalner, and V. Misra, Appl. Phys. Lett. 92, 243506 (2008)

[68]. N. A. Ives, G. W. Stupian and M. S. Leung, Appl. Phys. Lett. 50, 256 (1987).

[69]. L. Helsen, E. B. Marlies, K. V. Bael, G. Vanhoyl and J. Mullens, Thermo. chemica. Acta 414, 145–153 (2004).

[70]. S. R. Kasi, M. Liehr, P.A. Thity, H. Dallaporta and M. Offenbergd, Appl. Phys. Let, 59, 108 (1991).

[71]. K. Motai, T. Itoga, T. Irie Jpn. J. Appl. Phys., 37, 1137 (1998).

[72]. F. J. Grunthaner and J. Maserjian, IEEE Trans. Nucl. Sci. NS-24, 2108 (1977)

[73]. B. Miao, R. Mahapatra, N. Wright, and A. Horsfall, J. Appl. Phys. 104, 054510 (2008).

4. Thermal stability of 1 nm high-κ material/Ge(100) interface as a function of surface preparation

This chapter describes an effective way to prepare oxide free dielectric-semiconductor interfaces between both HfO_2 and Al_2O_3 and the chemically treated germanium surface.. Energy band offsets for both high-κ layers deposited on the germanium substrate using photoemission spectroscopy measurements will also presented.

4.1 High-κ materials on Ge substrates

The passivation of the germanium surface is a possible method to minimize the interfacial defect states (D_{it}) and Ge out diffusion into the high-κ dielectric layer which has been reported to increase the leakage current density [1,2]. A wide range of germanium surface treatments such as chalcogenide [3,4] and rare-earth oxides [5] passivation, silicon deposition [6], nitridation [2,7,8] and oxidation [9-11] have been suggested to improve the electrical characteristics of high-κ/Ge MOS devices. Sulphur passivation has been shown to be one of the most promising methods for suppressing interfacial oxide growth in order to achieve equivalent oxide thickness (EOT) scaling following high-k deposition and has also been effective at reducing the interface state density (D_{it}) [12]. Several studies using sulphur [13-15] as an interlayer at the Al_2O_3/Ge interface have investigated the effects of post dielectric deposition or post metallization annealing on the thermal stability of the interface. Recently, Swaminathan et al [16] reported interfacial GeO_2 growth at Al_2O_3/Ge interface after forming gas anneal. Similarly Oshima et.al [17] also reported GeO_2 formation in a GeO_xN_y layer at the HfO_2/Ge interface following molecular hydrogen annealing. Xie et al have also reported the reduction of Ge diffusion into a HfON layer for the sulphur treated sample as compared with the HF pre-cleaned germanium surface after post deposition anneal at 500^oC in N_2 ambient [18]. In addition, there are a number of studies which report hafnium germinate interlayer formation at the HfO_2/Ge interface with and without post deposition annealing

treatments [13,19,20]. In addition, Frank et al [21] reported the complete desorption of sulphur from the sulphur passivated germanium surface at $\leq 380^{o}$C after vacuum annealing treatment. Therefore, it is necessary to understand the chemical changes that occur at the dielectric/Ge interface during post deposition anneal in order to optimize interface formation. This study investigates the thermal stability of ALD deposited Al_2O_3 or HfO_2 on hydrofluoric acid (HF) and sulphur treated Ge (100) surfaces up to 700^{o}C using high surface sensitivity synchrotron radiation based soft x-ray photoemission spectroscopy (SXPS). This photoemission spectroscopy technique offers high surface sensitivity enabling accurate identification of the chemical changes that occur at the Al_2O_3 or HfO_2/Ge interface as a function of thermal annealing.

4.2 Sample preparation

Native oxide covered n-Ge samples with resistivity 0.029 Ω cm were degreased in acetone and methanol for 2 minutes before being etched in a cyclic HF/water rinse treatment **(**HF: H_2O=1:10) to remove the native oxide layer [22]. For sulphur passivation, the HF treated sample was immersed in 10% aqueous ammonium sulphide ($(NH_4)_2S$) solution at room temperature for 20 minutes with a final water rinse and N_2 blow dry.

The HF treated and sulphur passivated samples were immediately loaded into an ALD chamber and ~ 1 nm HfO_2 or Al_2O_3 layer was deposited using 10 cycles of tetrakis(ethylmethylamino)hafnium (TMEAH) and water or trimethyl aluminium (TMA) and water as the precursors at 250^{o}C or 300^{o}C substrate temperature. Subsequently these samples were loaded and annealed in a step wise manner up to 700^{o}C in an ultra-high-vacuum chamber on the SX700 beamline at the ASTRID synchrotron in Aarhus University, Denmark. The core level photoemission spectra of Ge 3d, Hf 4f, Al 2p, S 2p, O 1s, C 1s and valence band (VB) were taken at photon energies ranging from 60 to 600 eV for the successive

annealing treatments. The overall estimated instrumental energy resolution at 60 eV and 130 eV photon energy is ~ 70 meV. The bulk Ge 3d peak was curve fitted with a Gaussian width 0.52±0.04 eV, a Lorentzian width 0.18eV, spin orbit splitting of 0.61 and branching ratio of 0.59 eV. The incident photon energy was corrected by taking the energy difference between the 1st and 2nd order photoemission peak.

4.3 Thermal stability of HfO_2 deposited on S passivated Ge surface

The Ge 3d core level spectra acquired at 130eV of the HfO_2/S/Ge sample and the ratio calculated for the interfacial oxide and sulphur component to bulk germanium as a function annealing treatments up to 700°C are shown in figures 4.1 and 4.2, respectively.

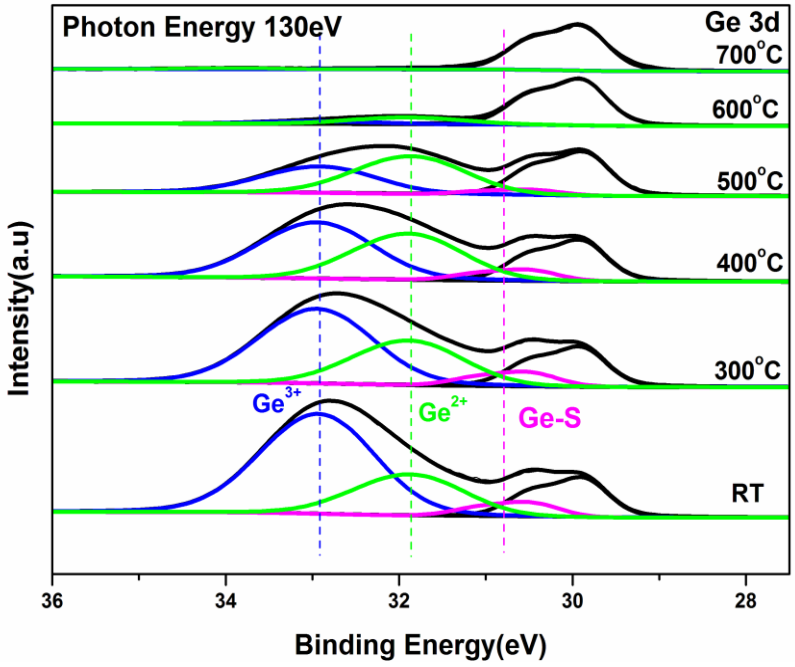

Figure 4.1: Ge 3d core level spectra taken at 60eV for the HfO_2/S/Ge sample of successive annealing cycles up to 700°C.

The Ge 3d spectrum measured at room temperature was curve fitted with a bulk peak at 29.9 eV, a higher binding energy peak shifted by +0.9 eV attributed to Ge-S bond formation and peaks at +1.85 eV and +2.9 eV relative to the bulk peak assigned to Ge^{2+} (GeO) and Ge^{3+} (Ge_2O_3) oxidation states, consistent with previous studies [23-25].

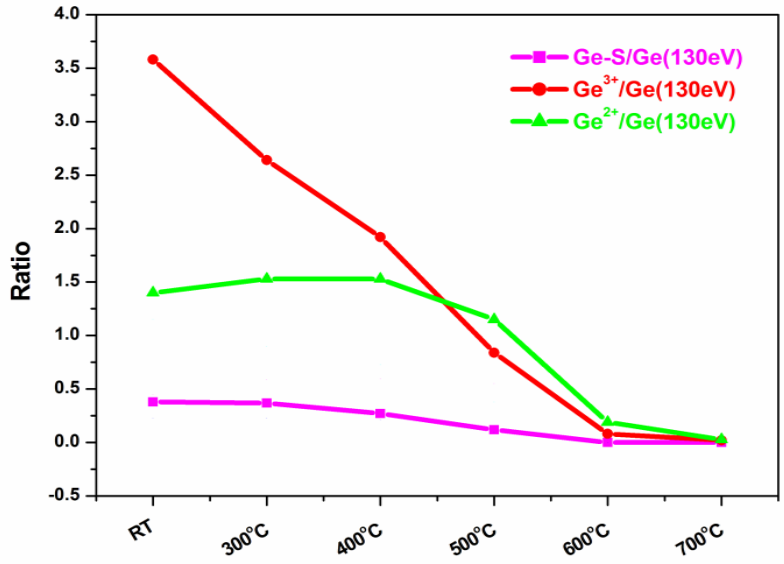

Figure 4.2: Ratio of interface oxide and sulphur components to Ge 3d bulk at successive annealing cycles up to 700°C.

Annealing this sample up to 400°C shows a gradual attenuation of Ge^{3+} signal accompanied with a marginal increase of Ge^{2+} signal which can be more clearly seen from the ratio calculated for the oxide to bulk germanium component [25,26]. Annealing at 500°C attenuates both the Ge^{3+} and Ge^{2+} oxide signals which is consistent with previous report that desorption of the Ge^{2+} oxidation state begins to occur at 430°C [26].

The intensity of the sulphur component is significantly attenuated at this temperature and is completely removed from the interface following the 600°C anneal. This is identical to the desorption temperature observed for the thermal annealing studies of Al_2O_3 on the sulphur passivated germanium surface discussed later. While following the 700°C anneal residual traces of interfacial oxide can be detected, given the surface sensitivity of the measurements,

the interface can be considered to be effectively oxide free. Figures 4.3 and 4.4 show the O1s and Hf 4f peak acquired at 600 eV and 130 eV and the S 2p peak at 230 eV for the successive vacuum annealing steps.

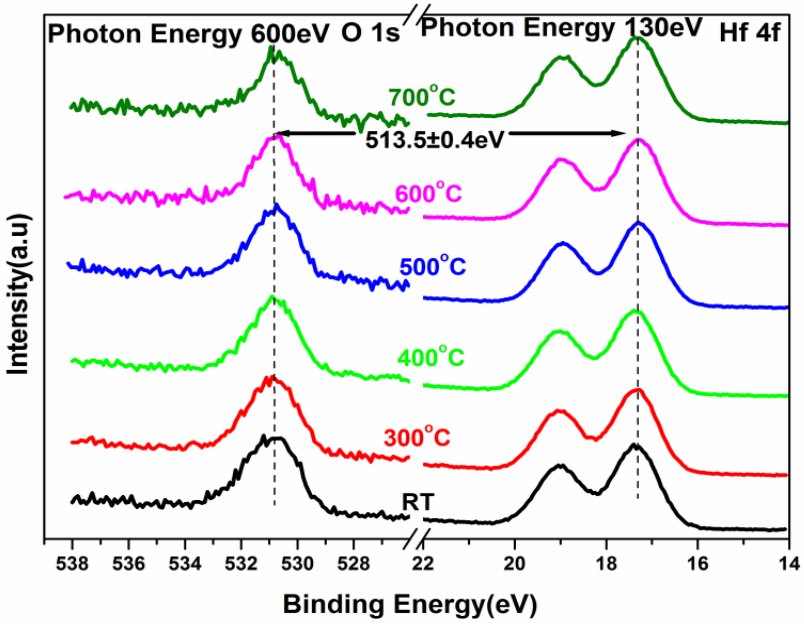

Figure 4.3: O 1s and Hf 4f spectra taken at 600eV and 130eV for the HfO_2 on sulphur passivated sample at various stages of annealing treatments.

The binding energy difference of 513.5 eV between the O1s and Hf 4f signals for the room temperature measurement varied by no more than ±0.4 eV throughout the annealing sequence which is consistent with the HfO_2 layer remaining stable at the reported value for stochiometric HfO_2 material [27].

The Hf 4f peak full width at half maximum (FWHM) of 1.3 eV showed no change as a result of successive annealing suggests that it is thermally stable up to 700^{o}C.Noriyuki et al [28] and Chu et al [29] previously reported HfO_2 layer to be thermal stability at 500^{o}C for 10 minutes and 700^{o}C for 1 minutes for post vacuum annealing treatments on germanium substrates. The S 2p peak located at 162 eV indicates the presence of sulphur at HfO_2/Ge interface [18]. This interface sulphur peak profile was not significantly affected up to 400^{o}C however further annealing at 500^{o}C progressively reduced the intensity of sulphur signal and

after 600°C annealing treatment, the sulphur was completely removed from the interface as consistent with our current study where the complete removal of interface sulphur at this same temperature from the Al_2O_3/S/Ge stack was also observed.

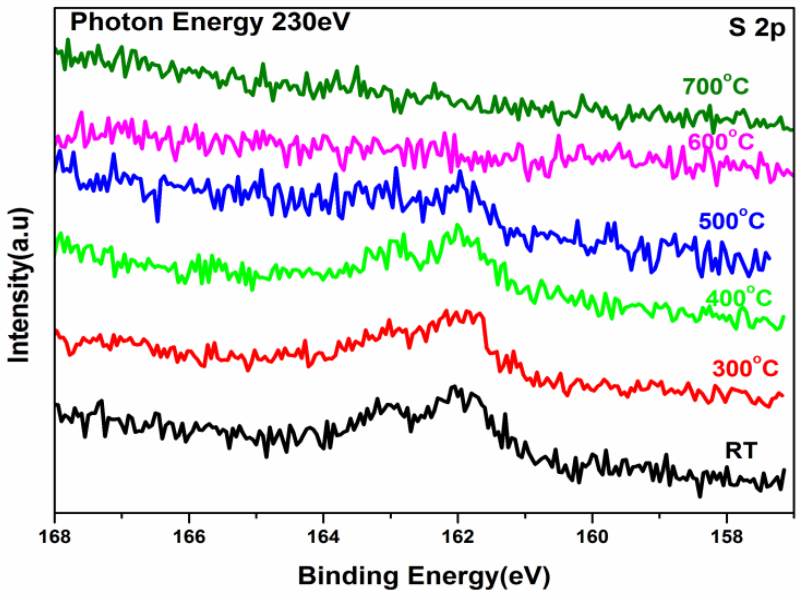

Figure 4.4: S 2ptaken at 230eV for the HfO_2 on sulphur passivated sample at various stages of annealing treatments.

However, previously Frank et al [21] reported complete desorption of sulphur from the sulphur passivated germanium at 380°C in the absence of a capping overlayer.

4.3.1 Thermal stability of sulphur passivated Ge surface

The thermal stability of a sulphur passivated Ge (100) surface without a high-κ overlayer was studied as a function of annealing temperatures. The Ge 3d spectra taken at 130 eV and S 2p core level spectra at 230 eV (inset) with the thermal anneals which are shown in figure 4.5 indicate that no change in the sulphur signal is seen up to 400°C, however, sulphur was completely removed after the 600°C annealing . This indicates that the presence of the HfO_2 overlayer doesn't have significant impact on the desorption temperature of the interfacial sulphur.

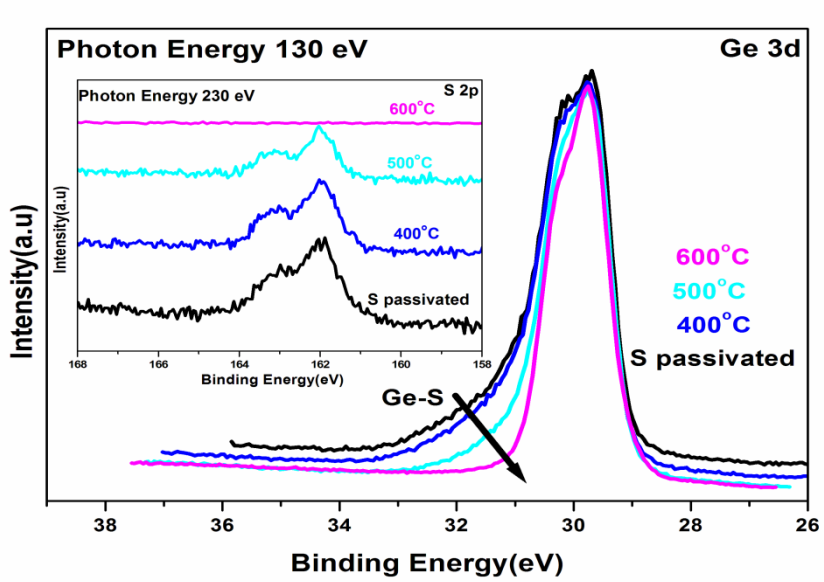

Figure 4.5: Ge 3d peak at 130eV and S 2p peak at 230eV (inset) for the sulphur passivated germanium sample as a function of annealing temperatures.

4.3.2 Energy band offset for HfO_2/S/Ge structure

The Valence band (VB) spectra acquired at 60 eV for the sulphur passivated germanium surface before and after HfO_2 deposition are shown in figure 4.6.

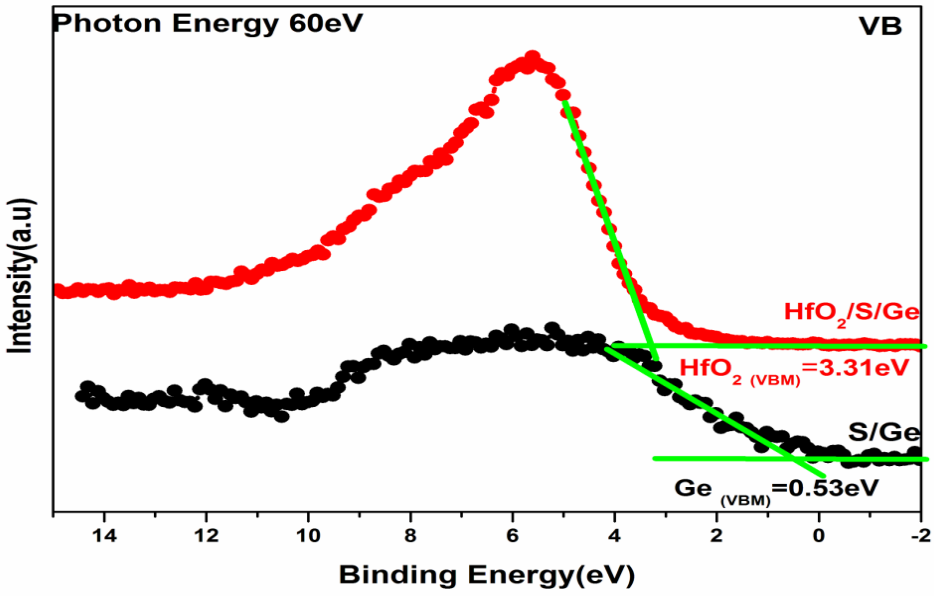

Figure 4.6: Valence band (VB) spectra taken at 60 eV for the sulphur passivated sample and the HfO_2 deposited on the sulphur passivated sample Approximated uncertainty during the extraction of valence band minimum using linear interpolation method ± 0.1 eV.

The valence band maximum of sulphur passivated germanium surface and HfO_2 dielectric material was extracted using a linear interpolation method. The valence and conduction band offsets were estimated from the following equations [30].

$$\Delta E_V = \Delta E_{CL} + \left(E_{CL}^{Ge} - E_{VBM}^{Ge}\right) - \left(E_{CL}^{HfO_2} - E_{VBM}^{HfO_2}\right) \quad 4.1$$

Where ΔE_{CL} is the core level energy difference between Hf 4f (dielectric oxide) and Ge 3d(substrate) peak $\left(E_{CL}^{HfO_2} - E_{CL}^{Ge}\right)$ and is measured to be 12.6 eV while $\left(E_{CL}^{Ge} - E_{VBM}^{Ge}\right)$ and $\left(E_{CL}^{HfO_2} - E_{VBM}^{HfO_2}\right)$ were calculated to be 29.37 eV and 14.0 eV, respectively. These values were substituted into the above equation and the valence band offset (ΔE_V) was estimated as 2.7 eV. A conduction band offset (ΔE_c) of 2.2 eV was calculated by substituting ΔE_V, the Ge and HfO_2 band gaps of 0.66 eV and 5.7 eV [31], respectively, into the following equation.

$$\Delta E_C = E_g(HfO_2) - E_g(Ge) - \Delta E_V \quad 4.2$$

The schematic energy band diagram for the HfO_2/S/Ge structure plotted from the determined band offsets using the model proposed by Kruat et al [30] shown in figure 4.7 suggests this dielectric layer/Ge interface has sufficiently high barriers to inhibit hole or electron injection [31].

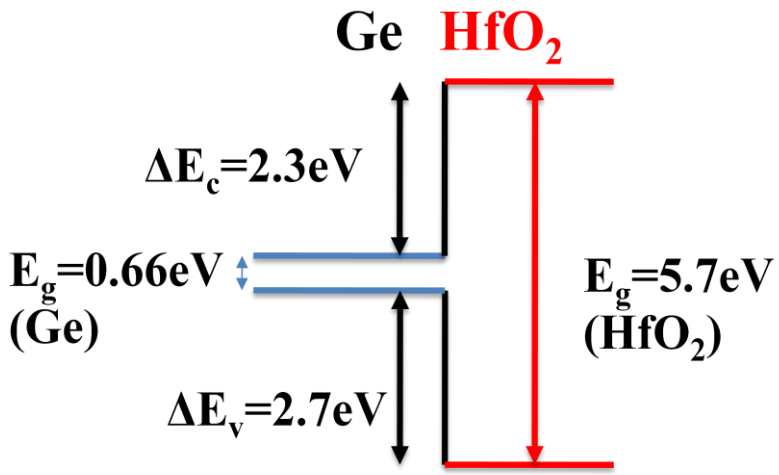

Figure 4.7: Energy band diagram of HfO_2/S/Ge sample inferred from the VB spectra

4.4. Thermal stability of HfO_2 deposited on HF treated Ge surface

The Ge 3d spectra taken for the HfO_2 deposited on the HF treated germanium surface at 130 eV and the ratio of interfacial oxide components to bulk Ge 3d with the successive annealing stages are shown in figures 4.8 and 4.9.The Ge 3d spectra acquired at room temperature was peak fitted with bulk peak at 29.9 eV and the higher binding energy interface oxide peak components shifted to +0.85 eV, +1.85 eV and +2.9 eV are identified as Ge^{1+} (Ge_2O), Ge^{2+} (GeO) and Ge^{3+} (Ge_2O_3) [24,25].

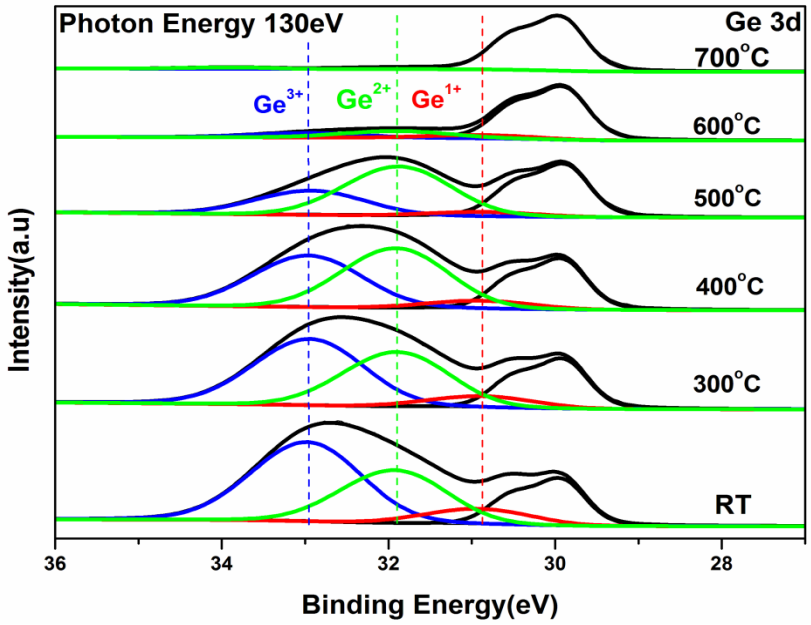

Figure 4.8: Ge 3d core level spectra taken at 130 eV for the HfO_2/Ge sample of successive annealing cycles up to 700°C.

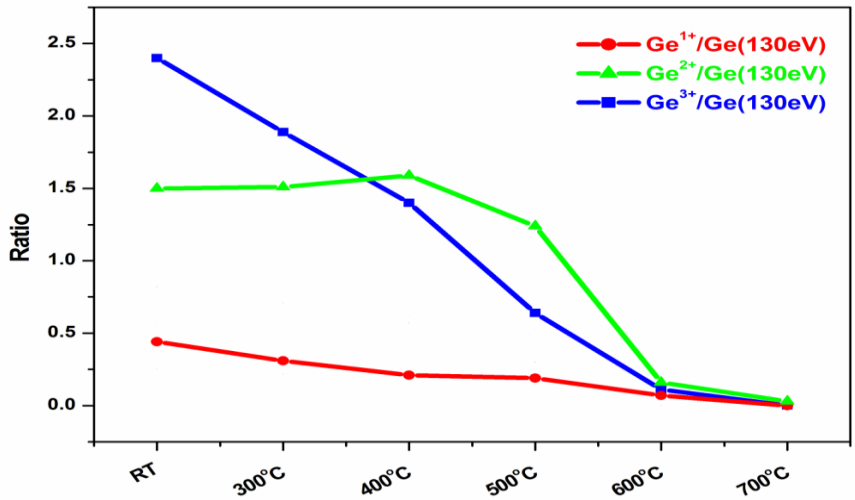

Figure 4.9: Ratio of interface oxide to Ge 3d bulk at successive annealing cycles up to 700°C.

The gradual attenuation of interfacial oxide component Ge^{3+} and Ge^{1+} peaks along with a slight increase of Ge^{2+} signal suggests some oxygen transfer from the Ge^{3+} and Ge^{1+} state to Ge^{2+} up to 400^{o}C annealing treatment. Subsequent annealing shows progressive attenuation of all the interface oxide signals with a very small residual interfacial oxide remaining following the 700^{o}C anneal in contrast with previous studies which reported strong chemical interaction between hafnium and silicon at the $HfO_2/SiO_x/Si(111)$ interface at this annealing temperature [33]. The thickness of residual interfacial oxides was estimated to be ~ 0.9 nm.

4.5 Investigation of interfacial oxides –HfO_2/S/Ge and HfO_2/Ge samples

The Ge 3d spectra acquired at a photon energy of 130 eV for the sulphur passivated and HF treated germanium samples before and after HfO_2 deposited are shown in figure 4.10 and provide an insight into the origin of interfacial oxides present on both the samples.

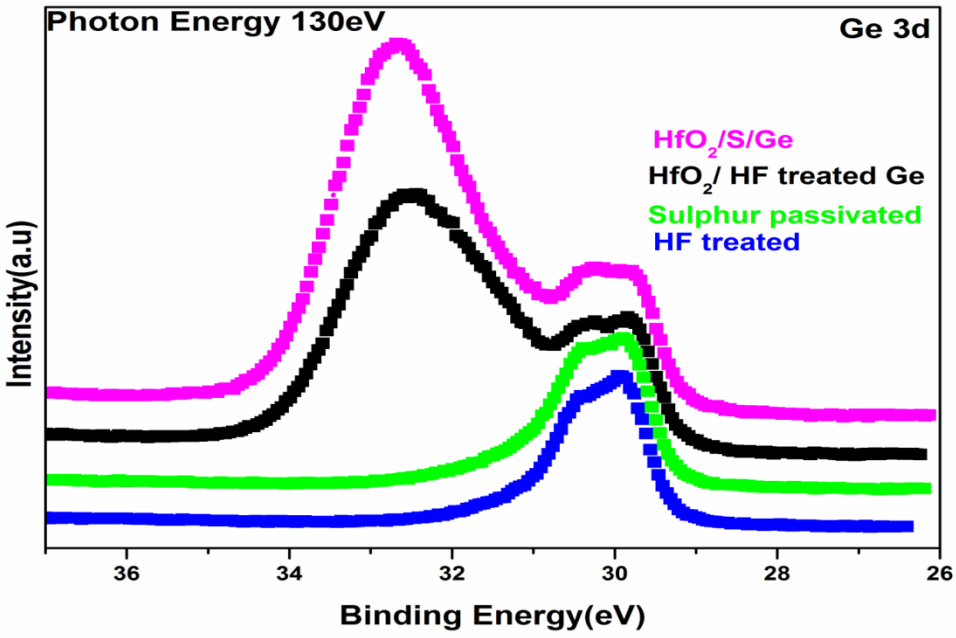

Figure 4.10: Ge 3d peak at 130eV for the HF treated and sulphur passivated germanium and HfO_2 deposited on sulphur and HF treated germanium surface.

Following sulphur passivation, no germanium oxide components are present in the Ge 3d bulk peak profile, however, following HfO_2 deposition, an interfacial oxide ~ 1.1 nm thick is detected which has either formed during the ALD growth or following air exposure. Similarly for the HF treated germanium surface, the post etch surface had a very thin residual germanium oxide, but the thickness of the HfO_2/Ge interfacial oxide is comparable to the sulphur treated surface. He et al [34] reported the growth of an interfacial oxide following the deposition of ALD-HfO_2 on GeO_x/Ge surface, however they observed an increase in the thickness of this layer following a post deposition anneal at 450^{o}C in a nitrogen environment, in contrast to the vacuum annealing results in the current study. No evidence of Ge or Hf diffusion was observed for either surface preparation and the results suggest that an essentially oxide free HfO_2/Ge (100) interface can be formed by vacuum annealing to these high temperatures without affecting the stoichiometry of high-κ layer, This is in contrast to the study by Renault et al who reported evidence of hafnium germanate formation after ALD deposition of HfO_2 at 350^{o}C without any addition post deposition annealing treatment [19].

4.6. Thermal stability of Al_2O_3 deposited on sulphur passivated Ge surface

Figure 4.11 show Ge 3d core level spectra taken at 60 eV for the Al_2O_3/S/Ge sample at successive anneal cycles up to 600^{o}C. The Ge 3d core level can be curve fitted with a bulk component at 29.9 eV and the higher binding energy components are identified as Ge-S (0.63 eV),Ge^{3+} (2.7 eV) and Ge^{4+} (3.5 eV), respectively [13,15,25]. The estimated inelastic mean free path λ of the photoemitted electrons for 60 eV photon energy is ~ 0.5 nm giving an overall sampling depth of less than 2 nm [35]. The estimated thickness of the interfacial oxide layer is approximately 0.7 nm. Annealing the sample at temperatures of 300^{o}C, 400^{o}C and 500^{o}C shows a significant reduction in the interface oxide components as can be seen from the changes in the profile of the Ge 3d core level peak.

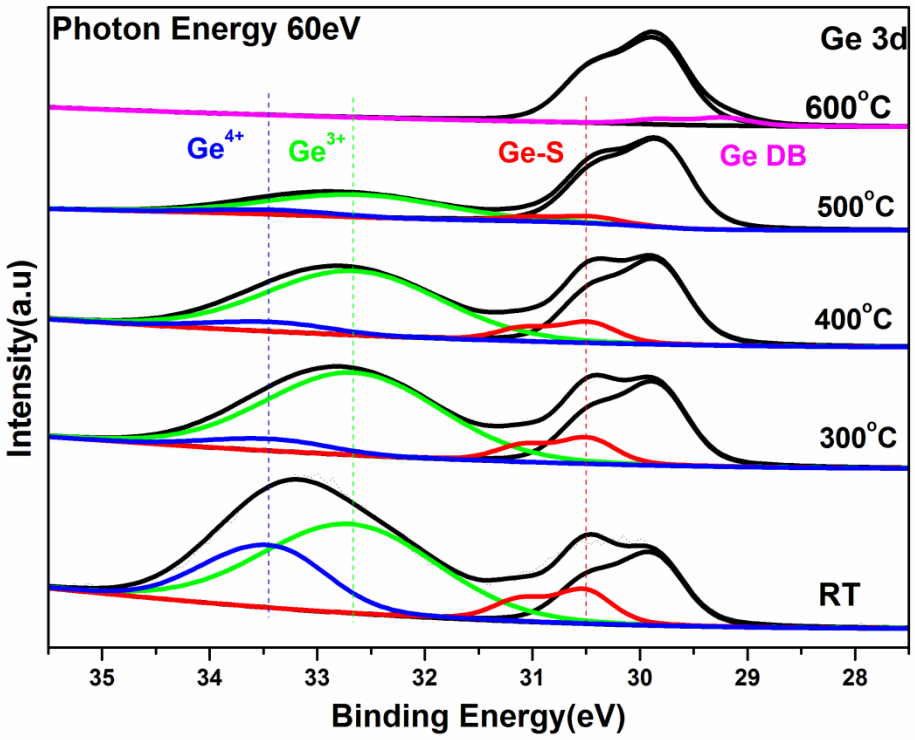

Figure 4.11: The Ge 3d core level spectra acquired at a photon energy of 60 eV for the Al_2O_3/S/Ge sample at successive anneal cycles up to 600°C.

Further annealing at 600°C which completely removed the interface component is accompanied by the appearance of a lower binding energy peak shifted to 0.53 eV from the bulk and identified as dangling bond formation at the interface. The ratio of the oxides to substrate peak intensity calculated to precisely quantify the removal of the interfacial oxide as a function of annealing treatments are shown in figure 4.12. Annealing at 400°C shows a significant attenuation of the Ge^{3+} and Ge^{4+} components however there was no significant attenuation of the sulphur signal suggesting that the presence of the high-κ layer inhibits this desorption as XPS studies reported by Frank et al [21] reported that sulphur is completely desorbed from the sulphur treated germanium surface at 380°C in a vacuum anneal. Subsequent 500°C annealing treatment further reduces the interface oxide components which are completely attenuated after the 600°C annealing treatment implying abrupt Al_2O_3/Ge interface formation.

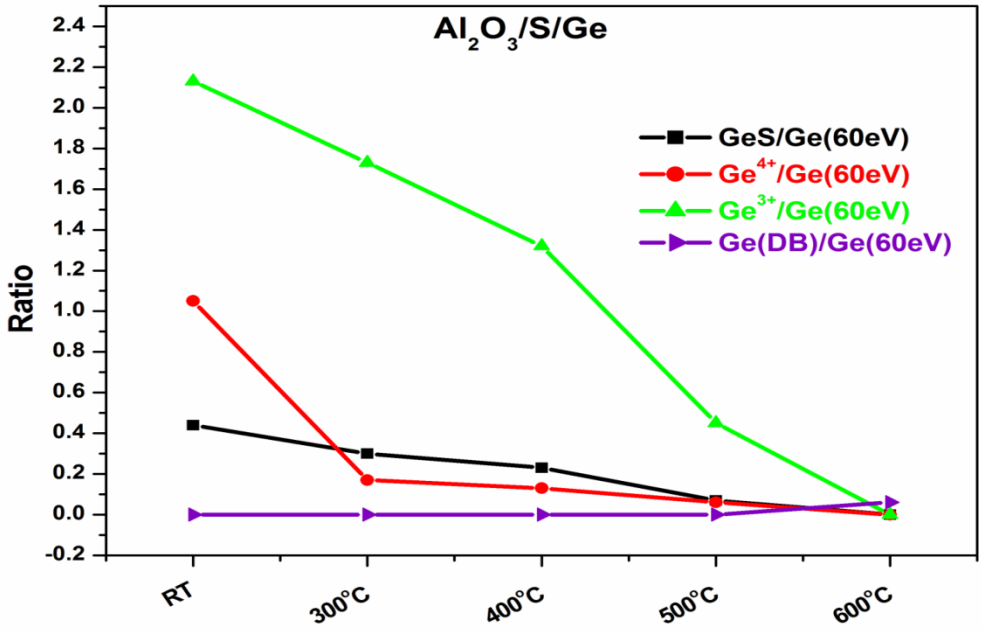

Figure 4.12: Ratio of the interface oxide and sulphur components to the Ge 3d bulk component at 60 eV for the sulphur passivated sample at the different annealing temperatures up to 600°C.

This vacuum annealing treatment showed no evidence of germanium out diffusion into the Al_2O_3 high-κ layer in contrast to the results of a rapid thermal annealing study of Al_2O_3/Ge structure in N_2 ambient at 600°C by Chao-Ching Cheng et al [36] which reported significant out diffusion of interfacial GeO_2 into the Al_2O_3 layer.

Figure 4.13 and 4.14 display the S 2p spectra acquired at 230 eV and the O 1s and Al 2p spectra at 600 eV and 120 eV, respectively, for the successive vacuum anneals. The interface sulphur S 2p core level spectra at 161.8 eV [15, 37] can be curve fitted with a single spin-orbit-split component peak consistent with the formation of a well defined Ge-S bonding interaction at the Al_2O_3/Ge interface. A similar S 2p peak profile has been reported after annealing the sulphur treated germanium surface at 200°C [38,39]

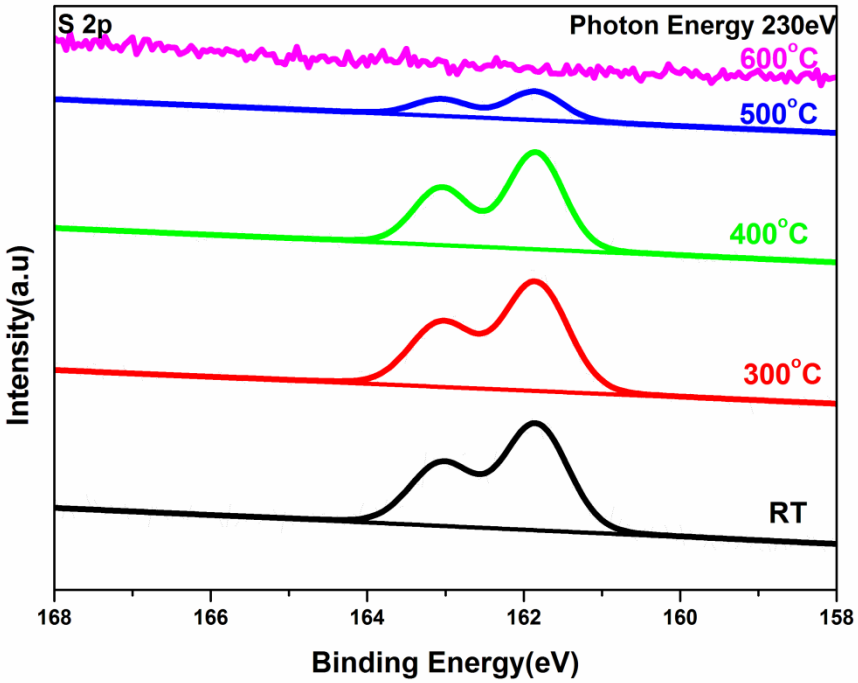

Figure 4.13: Curve fitted S 2p spectra acquired at a photon energy of 230eV showing the attenuation in the signal above 400°C anneals for the Al_2O_3/S/Ge sample.

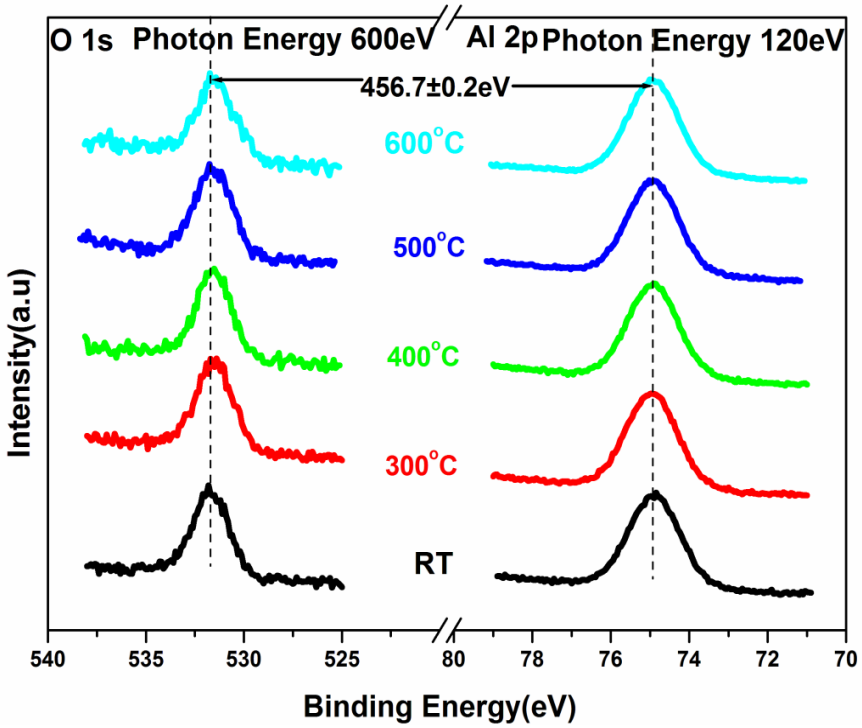

Figure 4.14: O 1s and Al 2p spectra acquired at photon energies of 600eV and 120eV, respectively for the sulphur passivated sample at different annealing stages up to 600°C.

Annealing up to 400^{o}C shows no significant change in the peak profile however at 500^{o}C there is a sharp decrease in the intensity of sulphur signal suggesting the desorption of sulphur from the interface. Subsequent annealing treatment at 600^{o}C completely removes the sulphur component consistent with the attenuation of the high binding energy peaks in the Ge 3d core level spectrum consistent with the breaking of the Ge-S bonds. The binding energy difference between Al 2p peak and the O1s peak is approximately 456.7 eV which is indicative of the presence of a stoichiometric Al_2O_3 layer as reported in previous studies [36]. The binding energy difference varies no more than ±0.2 eV with the annealing treatments and is very close to the value reported for sapphire [40]. The Al 2p spectra show no change in terms of the full width at half maximum (FWHM) of 1.5 eV indicating the thermal stability of this dielectric layer up to 600^{o}C.

4.6.1 Energy band offset for the Al_2O_3/S/Ge structure

The thermal stability of the dielectric-semiconductor valence band offset for the Al_2O_3/S/Ge structure was determined from the valence band(VB) spectra acquired at 60 eV photon energy taken after successive anneals up to 600^{o}C and shown in figure 4.15. The main difference with temperature is the appearance of Ge substrate signal intensity in the 0.6 eV – 4 eV binding energy range attributed to the desorption of the interfacial oxide layer. The valence and conduction band offsets were calculated using the model proposed by Kraut et al [30]. The VB spectrum following the 600^{o}C anneal displayed a clear VB maximum from which it is possible to determine the band offsets to the Al_2O_3 valence band feature. Therefore, the substrate and dielectric VBM were directly extracted from the VB spectra of using a linear interpolation method. Thus the valence band offset can be estimated from the following equation.

$$\Delta E_V = \Delta E_{CL} + \left(E_{CL}^{Ge} - E_{VBM}^{Ge}\right) - \left(E_{CL}^{Al_2O_3} - E_{VBM}^{Al_2O_3}\right) \qquad 4.3$$

Where ΔE_{CL} is the binding energy difference between Al 2p and Ge 3d core level spectra given as 45.33 eV; $\left(E_{CL}^{Ge} - E_{VBM}^{Ge}\right)$ as 28.8 eV and $\left(E_{CL}^{Al_2O_3} - E_{VBM}^{Al_2O_3}\right)$ 70.7 eV. The estimated valence band offset of 3.4 eV is substituted in the following equation by assuming the band gap of Al_2O_3 is 6.8 eV and the germanium band gap is 0.66 eV.

$$\Delta E_C = E_g(Al_2O_3) - E_g(Ge) - \Delta E_V \qquad 4.4$$

The calculated conduction offset is 2.7 eV which is consistent with reported values using photoemission studies [17,43]. The band offset calculations shown in figure 4.6 suggest this Al_2O_3/Ge stack has sufficient band offset to prevent carrier injection as suggested by Robertson [32].

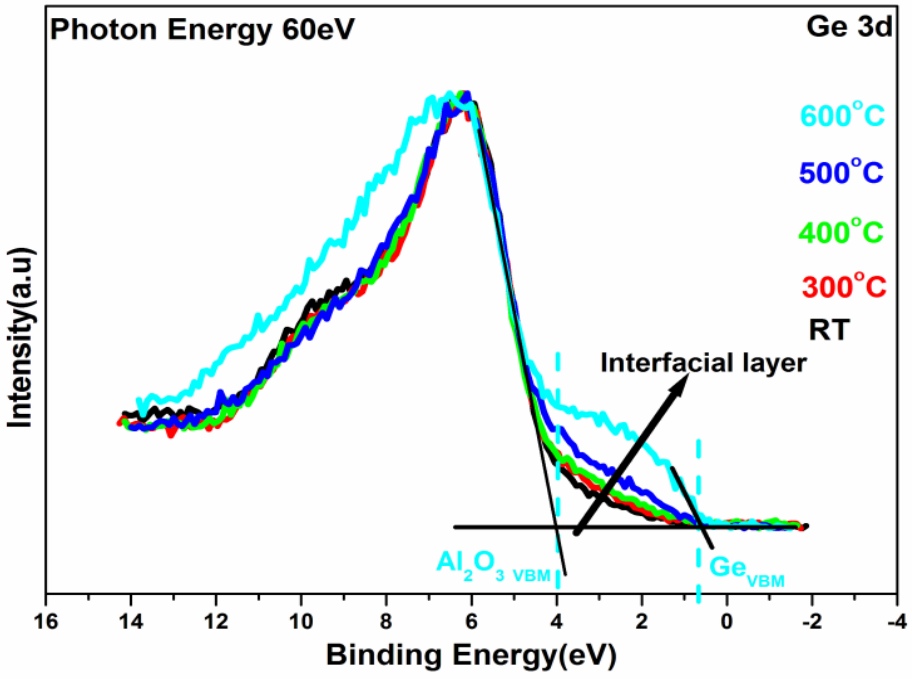

Figure 4.15: Valence band (VB) spectra taken at 60eV for the sulphur passivated sample up to 600°C

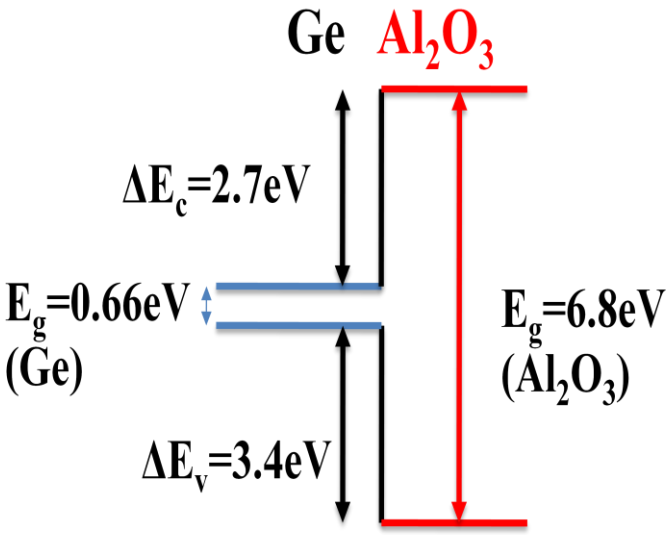

Figure 4.16: A schematic energy band diagram after the 600°C anneal showing the calculated VB and CB offsets.

4.7 Thermal stability of Al_2O_3 deposited on HF treated Ge surface

The Ge 3d core level spectra of the HF etched surface taken at 60 eV for the Al_2O_3/Ge sample exposed to successive annealing steps up to 600°C are shown in figure 4.17. The Ge 3d spectra were curve fitted with bulk and three oxide components shifted to 1.8 eV, 2.7 eV and 3.5 eV higher binding energy as Ge^{2+} (GeO), Ge^{3+} (Ge_2O_3) and Ge^{4+} (GeO_2) from the Ge 3d bulk peak at 29.9 eV [25]. The thickness of interfacial oxide was estimated to be approximately 0.7 nm. Annealing at 400°C shows significant attenuation of the Ge^{4+} and Ge^{3+} oxidation states, however, the increased Ge^{2+} signal is attributed to the partial oxygen transfer from the higher oxidation states of germanium. Subsequent annealing at 500°C results in the continued attenuation of the oxidation states and the appearance of a lower binding peak shifted by 0.63 eV from the bulk peak again identified as dangling bonds. The interfacial

oxides were not completely removed even after 600°C annealing treatment, however, given the surface sensitivity of these photoemission spectra, the residual oxide is significantly less than a monolayer coverage.

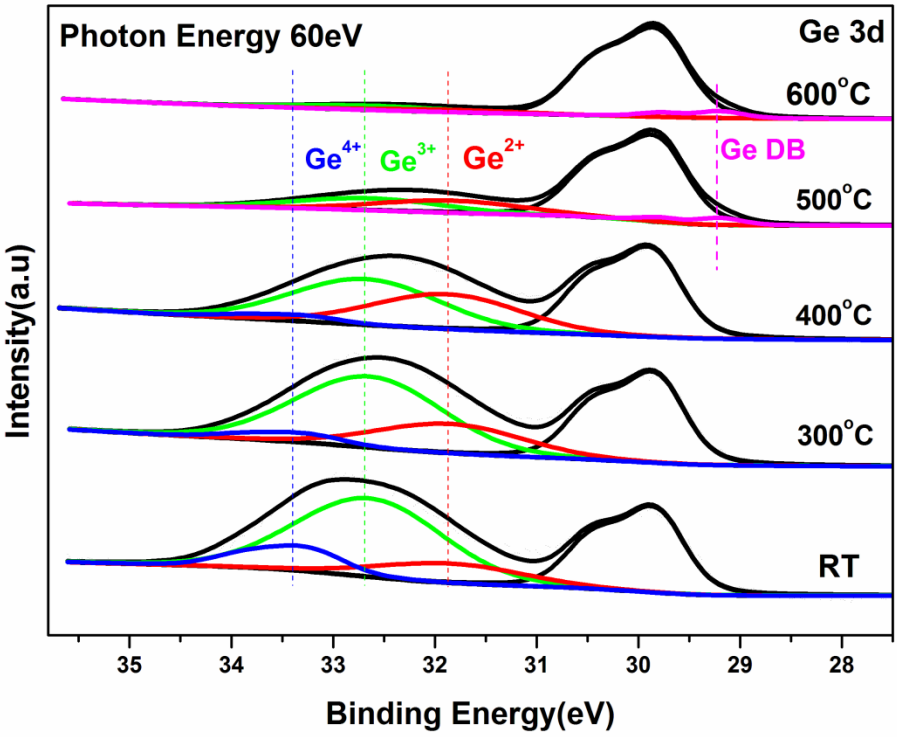

Figure 4.17: The Ge 3d core level spectra acquired at a photon energy of 60 eV for the Al_2O_3/Ge sample at successive anneal cycles up to 600°C.

The ratios of the oxide to substrate signal intensities as a function of thermal anneal are shown in figure 4.18. The increase in Ge^{2+} signal occurs simultaneously with the attenuation of Ge^{3+} and Ge^{4+} signals suggesting partial oxygen transfer in agreement with annealing studies of a thin germanium oxide covered germanium substrate [26]. Annealing at 500°C significantly attenuates the Ge^{2+} and Ge^{3+} signals in agreement with the work of Prabhakaran et.al [26] as they reported the loss of the Ge^{2+} oxidation state at 430°C.

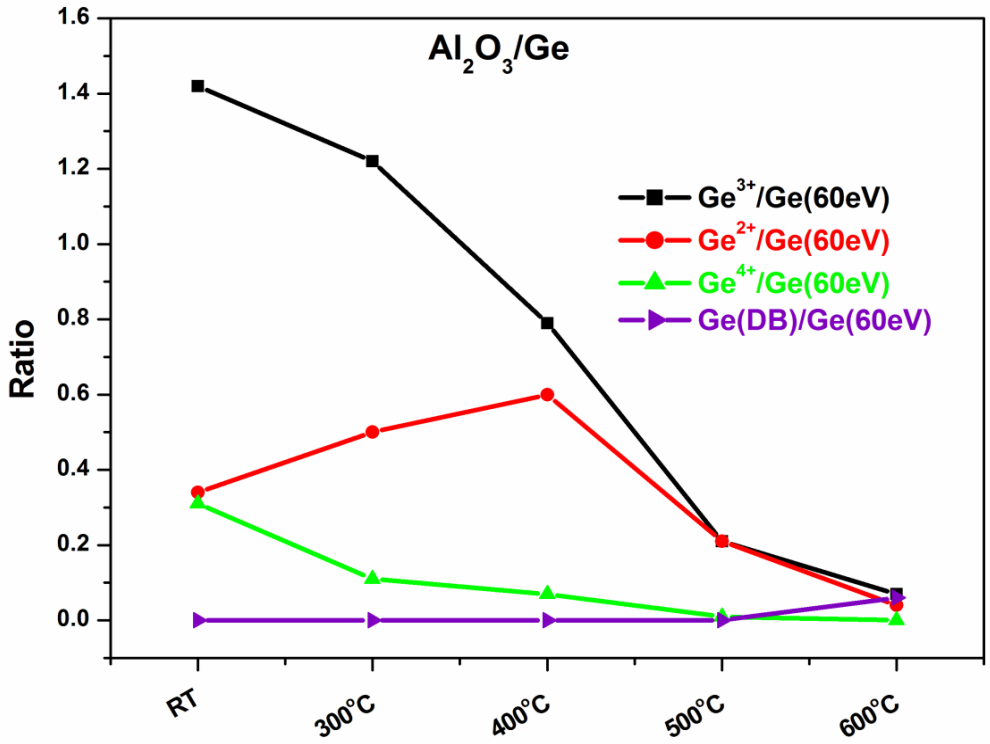

Figure 4.18: Ratio of interface oxide components to Ge 3d bulk component at 60eV for the HF treated sample at the different annealing temperatures up to 600°C.

4.8 Investigation of interfacial oxides-Al_2O_3/S/Ge and Al_2O_3/Ge stacks

The origin of interfacial oxide layer beneath the Al_2O_3 (1 nm) layer for sulphur passivated and HF treated Ge samples required further investigation. Therefore, a separate set of samples were prepared with the same surface treatments but without any Al_2O_3 deposition and were measured at 130 eV by synchrotron radiation based photoemission. The Ge 3d core level spectra for sulphur passivated, HF treated and native oxide (untreated) samples acquired at 130 eV photon energy are shown in figure 4.19 and compared to the Ge 3d spectra for Al_2O_3 deposited on HF treated and sulphur passivated germanium surfaces. The Ge 3d peak profiles of the HF and sulphur treated surfaces are almost identical prior to Al_2O_3 deposition

indicating almost complete removal of the native oxide. Following Al_2O_3 deposition, the magnitude of the interfacial oxide on both surfaces is also very similar and estimated to be approximately 0.7 nm thick.

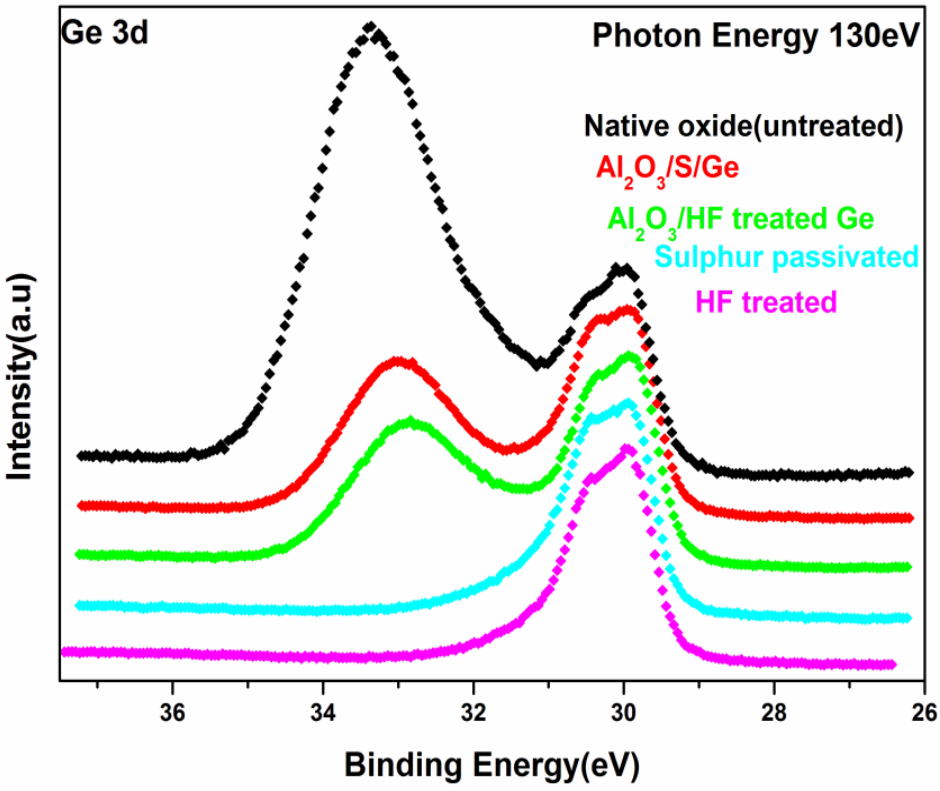

Figure 4.19: The Ge 3d peak acquired at 130eV photon energy for the native oxide (untreated), HF treated and sulphur passivated germanium in comparison to the Ge 3d peaks acquired for the sulphur and HF treated Al_2O_3 capped germanium surfaces.

Therefore, the interfacial oxide thickness is independent of surface preparation and grew either during the Al_2O_3 deposition process or post deposition when the samples were air exposed. Previous studies have reported interfacial germanium oxide growth on the clean germanium surface following the deposition of a 1 nm thick Al_2O_3 layer [42]. In addition, oxygen permeability studies of Al_2O_3 on silicon substrates [43] reported an increase in the interfacial oxide layer thickness after exposure to atmospheric conditions. Interfacial

germanium oxide growth at the Al_2O_3/Ge interface following oxygen treatment at elevated temperature also confirms the oxygen permeability of thin Al_2O_3 layers [9,10,44]. Therefore, it is not possible to unambiguously determine when this interface oxidation occurred, but the fact that the same thickness resulted on two differently prepared surfaces would indicate that the growth has a self-limiting nature and this study has shown that it can be removed at elevated temperatures.

4.9 Conclusion

The interface formation between ALD deposited HfO_2 and Al_2O_3 layer on both HF and sulphur passivated germanium surfaces and the subsequent high temperature thermal stability were studied using high resolution synchrotron based photoemission spectroscopy. The interfacial oxides were effectively removed at the higher annealing temperature on both samples without impacting the high-κ dielectric materials stoichiometry. The interfacial sulphur component present beneath the high-κ layer was removed from the interface above an annealing temperature of 500^{o}C. The calculated valence and conduction band offsets are of a sufficiently large magnitude to inhibit carrier injection.

4.10 References

[1]. N. Lu, W. Bai, A. Ramirez, C. Mouli, A. Ritenour, M. L. Lee, D. Antoniadis, and D. L. Kwong Appl. Phys. Lett. 87, 051922 (2005).

[2]. Y. Oshima, M. Shandalov, Y. Sun, P.Pianetta, and P. C. McIntyre Appl. Phys. Lett. 94, 183102 (2009).

[3]. S. Sioncke, J. Ceuppens, D. Lin, L. Nyns, A. Delabie, H. Struyf, S. De Gendt, M. Müller, B. Beckhoff, and M. Caymax, Microelectron. Eng. 88, 1553 (2011).

[4]. D. Tsoutsou , Y. Panayiotatos, S. Galata, A. Sotiropoulos, G. Mavrou, E. Golias and A. Dimoulas, Microelectron. Eng. 88, 407 (2011).

[5]. X. Li, X. Liu, Y. Cao, A. Li, H. Li, Di.Wu, Appl. Surf. Sci. 264, 783-786 (2013).

[6]. N. Wu , Q. Zhang, C. Zhu, D.S.H. Chan, A. Du ,N. Balasubramanian, M. F. Li, J. K. O. Sin and D. L. Kwong, IEEE Electron Device Lett. 25, 631, (2004).

[7]. T. Maeda, T. Yasuda, M. Nishizawa and S.Takagi, Appl.Phys. Lett. 85 3181(2004).

[8]. N. Wu, Q. Zhang, C. Zhu, C. C. Yeo, S. J. Whang, D. S. H. Chan, M. F. Li and B. Cho. J. Appl. Phys. Lett. 84, 3741 (2004).

[9]. R. Zhang, T. Iwasaki, N. Taoka, M. Takenaka, and S. Takagi, Appl. Phys. Lett.98, 112902 (2011).

[10]. R. Zhang, T. Iwasaki, N. Taoka, M. Takenaka, and S. Takagi, IEEE Trans. Electron Devices. 59, 335 (2012).

[11]. S. N. A. Murad, P. T. Baine, D. W. McNeill, S. J. N. Mitchell, B. M. Armstrong, M. Modreanu, G. Hughes, R. K. Chellappan. Sol. Stat. Elect. 78,136–140 (2012).

[12]. S. Sioncke, H. C. Lin, A. Delabie, T. Conard, H. Struyf, S. De Gendt and M. Caymax ECS J. Solid State Sci. Technol. 1, P127-P132 (2012).

[13]. X. Li, A. Li, X. Liua, Y. Gonga, X. chun Chen, H. Li, D. Wu, Appl. Surf. Sci. 257 4589–4592, (2011).

[14]. S. Sioncke, H. C. Lin, G. Brammertz, A. Delabie, T. Conard, A. Franquet, M. Meuris, H. Struyf, S. De Gendt, M. Heyns, C. Fleischmann, K. Temst, A. Vantomme, M. Müller, M. Kolbe, B. Beckhoff and M. Caymax J.electrochem. Soc. 158 H687–92, (2011).

[15]. X. Bai-Qing, C. Hu-Dong, S. Bing, W. Sheng-Kai and L.Hong-Gang Chin. Phys. Lett. 29, 046801 (2012).

[16]. S. Swaminathan, Y. Sun, P. Pianetta, and P. C. McIntyre, J. Appl. Phys. 110, 094105 (2011).

[17]. Y. Oshima, Y. Sun, D. Kuzum, T. Sugawara,K. C. Saraswat, P. Pianetta, and P. C. McIntyre, J. Elect. Chemic. Soc. 155, G304-G309 (2008).

[18]. X. Ruilong and C. Zhu. Elect. Dev. Lett. IEEE.2811, 976-979(2007).

[19]. O. Renault, L. Fourdrinier, E. Martinez, L. Clavelier, C. Leroyer, N. Barrett, and C. Crotti. Appl. Phys. Lett. 90,052112 (2007).

[20]. V. Elshocht, M. Caymax, T. Conard, S. De Gendt, I. Hoflijk, M. Houssa, B. De Jaeger, J. Van Steenbergen, M. Heyns, and M. Meuris. Appl. Phys. Lett. 88, 141904 (2006).

[21]. M. M. Frank, S. J. Koester, M. Copel, J. A. Ott, V. K. Paruchuri, H. Shang and R. Loesing Appl. Phys. Lett 89, 112905 (2006).

[22]. T. Deegan and G. Hughes. Appl. Sur. Sci. 123, 66-70 (1998).

[23]. D. Tsoutsou, Y. Panayiotatos, A. Sotiropoulos, G. Mavrou, E. Golias, S. F. Galata, and A. Dimoulas. J. Appl. Phys. 108, 064115 (2010).

[24]. T. Weser, A. Bogen, B. Konrad, R. D. Schnell, C. A. Schug, and W. Steinmann. Physical Review B, 35, 8184 (1987).

[25]. J. Oh, J.C. Campbell Journal of Electronic Materials, 33, 364-367 (2004).

[26]. K. Prabhakaran, F. Maeda, Y. Watanabe, and T. Ogino Appl. Phys. Lett. 76, 2244 (2000).

[27]. K. Cherkaoui, S. Monaghan, M. A. Negara, M. Modreanu, P. K. Hurley, D. O-Connell, S. McDonnell, G. Hughes, S. Wright, R. C. Barklie, P. Bailey, and T. C. Q. Noakes, Journal of Applied Physics,104, 064113 (2008).

[28]. M. Noriyuki, T. Yasuda and Y. Abe. Journal of Applied Physics 107, 103536 (2010).

[29]. L. K. Chu, R. L. Chu, T. D. Lin, W. C. Lee, C. A. Lin, M. L. Huang, Y. J. Lee, J. Kwo and M. Hong. Sol. Stat. Elect.54, 965-971 (2010).

[30]. E. A. Kraut, R. W. Grant, J. R. Waldrop and S. P. Kowalczyk. Phys. Rev. Lett. 44, 1623 (1980).

[31]. M. Perego, G. Seguini, and M. Fanciulli. Materials Science in Semiconductor Processing, 11, 221-225(2008).

[32]. J. Robertson, J. Eur. Phys. J. Appl. Phys, 28(03), 265-291 (2004).

[33]. S. McDonnell, B. Brennan, P. Casey and G. J. Hughes. Surf. Sci., 605, 1928 (2011).

[34]. D. He, X. Cheng, D. Xu, Z. Wang, Y. Yu, Q. Sun, and D. W. Zhang J. Vac. Sci. Technol. B, 29, 01A802 (2011).

[35]. M. P. Seah, W. A. Dench Surface and Interface Analysis, 1, p2–11,(1979).

[36]. C. Cheng, C. Chien, G. Luo, J. Liu, C. Kei, D. Liu, C. Hsiao, C. Yang and C. Chang J. Electro chem. Soc, 155, G208 (2008).

[37]. R. B. Shalvoy, G. B. Fisher, and P. J. Stiles, Phys. Rev. B 15, 1697 (1977).

[38]. J Roche, P Ryan, G.J Hughes Appl. Surf. Sci. 174, 271–274, (2001).

[39]. G. Gothelid, C. LeLay, C. Wigren, M. Bjorkqvist, M. Rad, U.O. Karlsson, Appl. Surf. Sci., 115, 87. (1997).

[40]. C. S. Yang, J. S. Kim, J. Choi, M. H. Kwon, Y. J. Kim, J. G. Choi and G.T. Kim, J of Indust and Eng. Chem,6, 149-156, (2000).

[41]. V. V. Afanas'ev, A. Stesmans, A. Delabie, F. Bellenger, M. Houssa, and M. Meuris, Appl. Phys. Lett. 92, 022109 (2008).

[42]. M. Milojevic, R. Contreras-Guerrero, M. Lopez-Lopez, J. Kim, and R. M. Wallace Appl. Phys. Lett. 95, 212902 (2009).

[43]. W. Tsai, R.J. Carter, H. Nohira, M. Caymax, T. Conard, V. Cosnier, S. DeGendt , M. Heyns, J. Petry, O. Richard, W. Vandervorst , E. Young ,C. Zhao, J. Maes, M.

Tuominen , W.H. Schulte , E. Garfunkel , T. Gustafsson. Microelectron. Eng. 65, 259–272, (2003).

[44]. S. Shibayama, K.Kato, M.Sakashita, W.Takeuchi, O.Nakatsuka, S.Zaima Thin Solid Films 520, 3401 (2012).

5. High temperature thermal stability study of 1 nm high-κ materials deposited as a function of InAs surfaces

This chapter discusses the thermal stability of ultra-thin atomic layer deposited (ALD) high-κ (Al_2O_3 and HfO_2) layers (~1 nm thick) on sulphur passivated and native oxide covered InAs surfaces. The impact of the thermal anneal on the sulphur passivated InAs surface before and after high-κ deposition are investigated. Energy band offsets for both high-κ layers on the InAs surface determined from valence band photoemission measurements are also presented.

5.1 Introduction

Integration of high mobility InAs substrate materials in the development of n-channel metal oxide semiconductor (n-CMOS) devices potentially offer higher electron mobility than silicon substrates. However problems associated with the abrupt dielectric-semiconductor interface formation hampers the realization of this advantage. Previous studies relate Fermi level pinning to the poor electrical quality of interfacial oxides which form at the high-κ/III-V interfaces [1,2]. Several surface treatment methods like low energy ion sputtering [3,4], molecular hydrogen [5,6] and atomic hydrogen cleaning [7-9] methods have been used to prepare oxide free III-V surfaces. However, surface passivation strategies are one of the most promising approaches to limit substrate re-oxidation prior to or during high-κ deposition. The ex-situ passivation methods using wet chemical sulphur treatments have been reported as being effective at removing native oxides and passivating the surface [10]. The sulphur passivation combined with the post deposition annealing (PDA) of high-κ/III-V structures are reported to improve the electrical properties [11, 12]. Previously, Katayama et al [13] reported the complete removal of sulphur at 430^{o}C from the sulphur passivated InAs surface. Therefore there is a need to further investigate the thermal stability of sulphur at the semiconductor-dielectric interfaces. There are several other studies which suggest the

diffusion of substrate elements across the high-κ/III-V interfaces after the post annealing treatments [14, 15]. In addition to this, recently Martinez et al reported indium hydroxide formation at the Al_2O_3/InAs interface after post deposition anneal (PDA) at 600^oC in vacuum [16]. This study investigates the chemical changes induced by the post deposition annealing of ultra-thin ALD deposited Al_2O_3 or HfO_2 on sulphur and native oxide covered InAs surfaces using high resolution synchrotron radiation based photoemission spectroscopy which offers higher surface sensitivity than the conventional x-ray photoelectron spectroscopy.

5.2 Experimental

5.2.1 Sample preparation

N-type InAs(100) samples with doping density of 4×10^{17} cm^{-3} were pre-cleaned with acetone followed by methanol for 1 minutes prior to immersion in the ammonium sulphide solution (10%) for 20 minutes. The sulphur passivated and native oxide covered InAs surfaces were immediately loaded into the ALD chamber and ~1 nm Al_2O_3 or HfO_2 was deposited using 10 cycles of tri-methyl aluminium (TMA) and water or tetrakis(ethyl methyl amino) hafnium (TMEAH) and water as precursors. Subsequently these samples were secured into a molybdenum sample holder and loaded into the ultra high vacuum (UHV) chamber on the SX700 beamline at Aarhus University, Denmark. The SXPS spectra acquired for In 4d, As 3d, Al 2p, O 1s, S 2p, Hf 4f and valence band spectra were acquired at photon energies ranging from 69eV to 600 eV from room temperature and following successive anneals up to 600^oC. The As 3d and In 4d spectra taken at photon energies of 92 eV and 69 eV, respectively, to give comparable sampling depths of approximately 2 nm. The As 3d (In 4d) core level spectra was curve fitted with a branching ratio of 0.66 (0.67), a spin orbit splitting ratio of 0.7eV (0.85 eV), Gaussian line width of 0.72 eV (0.73 eV) and Lorentzian line width of 0.07eV (0.2eV). The photon energy at which these photoemission peaks were acquired

was energy corrected by taking the kinetic energy difference between the peaks acquired by 1st and 2nd order light from the monochromator.

5.3 Thermal stability of sulphur passivated InAs surfaces before and after Al_2O_3 deposition

The S 2p at 230 eV, and As 3d at 92 eV and In 4d at 69 eV for the sulphur passivated InAs surface was shown in figure 5.1 and 5.2. The increase of As 3d and In 4d photoemission peak intensity at higher binding energy attributes the bonding interaction with sulphur. The S 2p spectra results progressive attenuation at 500°C and completely attenuated at 600°C consistent with the removal of higher binding energy signals from bulk As 3d and In 4d core level spectra. However these results suggest that sulphur component on InAs surface can be

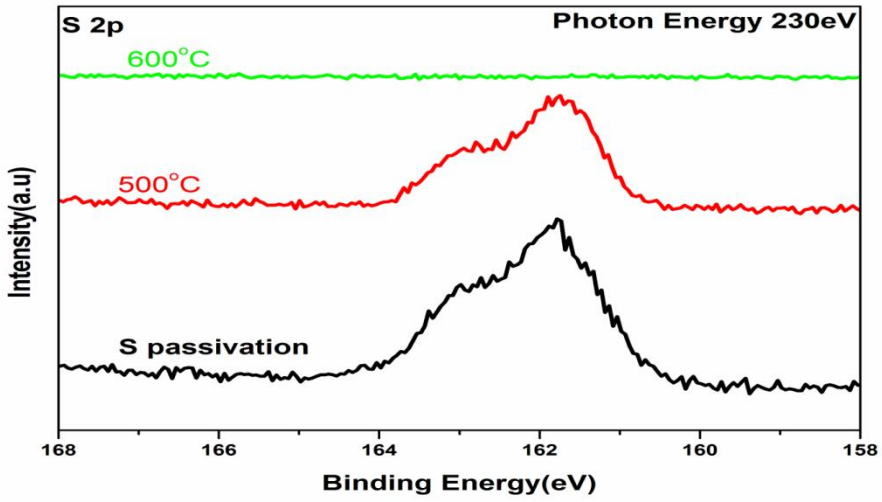

Figure 5.1: The S 2p spectra at 230eV for the sulphur passivated InAs surface following successive anneals.

stable up to 500°C whereas previous studies report complete attenuation of sulphur at 430°C [13]. Subsequently, ALD-Al_2O_3 on sulphur passivated InAs surface was measured to study any impact of top dielectric layer in retaining interfacial sulphur components during post deposition annealing.

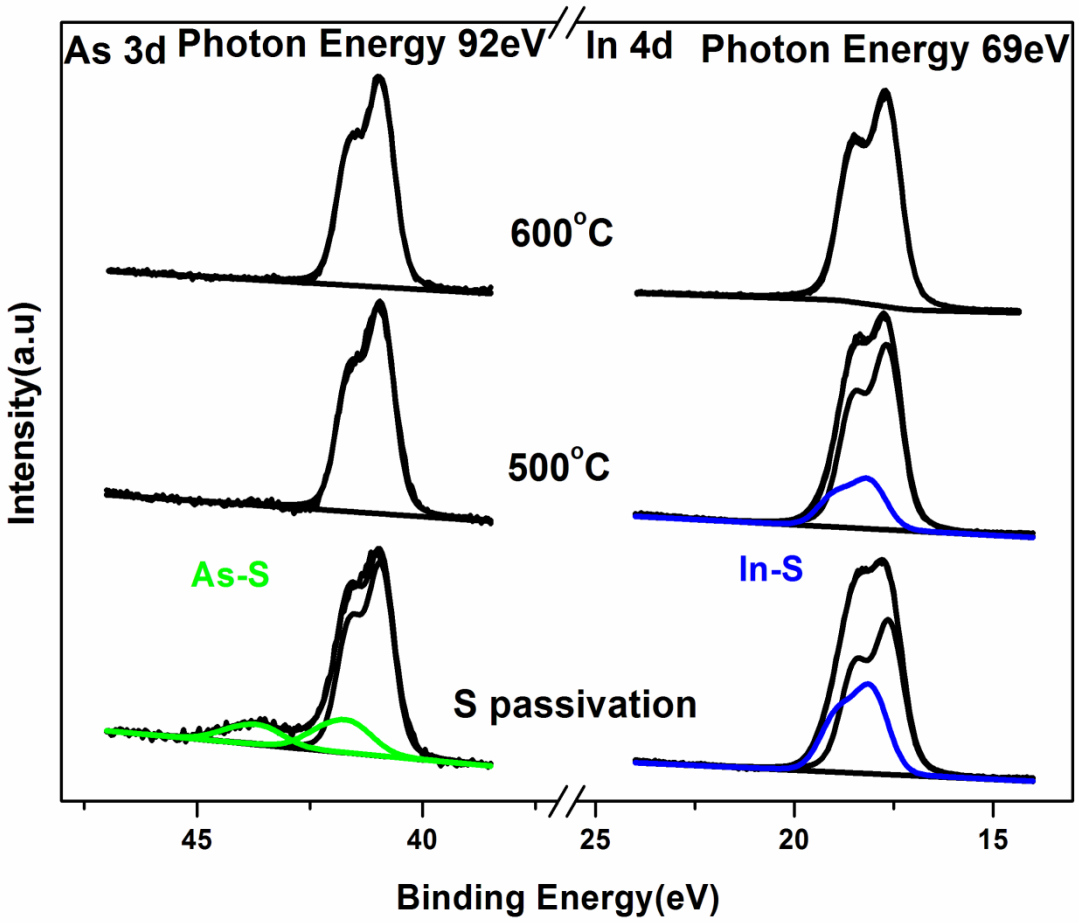

Figure 5.2: The As 3d and In 4d at 92 eV and 69 eV taken for the sulphur passivated InAs surface following successive annealing stages.

The As 3d and In 4d spectra was shown in figures 5.3(a) and (b) for the ultra thin Al_2O_3 deposited on sulphur passivated InAs surface as a function of annealing stages up to 600°C. The As 3d core level spectrum taken at room temperature was curve fitted with the bulk peak at 41 eV and higher binding energy peaks shifted to +3 eV, +2.9 eV and +3.7 eV are attributed to As-S, As_2O (As^{2+}) and As_2O_3 (As^{3+}) chemical states consistent with previous studies[17-20]. The origin of these interfacial oxides will be discussed later. Annealing the sample up to 400°C results in the gradual attenuation of the As^{2+} and As^{3+} states with no significant change in the As-S signal, however, at 600°C complete removal of all arsenic oxidation states and the As-S signal was observed. The In 4d core level spectrum was curve

fitted with a bulk peak at 17.5 eV and two higher binding peaks shifted by +0.65 eV and +1.38 eV were attributed to oxidised indium (Indium oxide 1) and In-S states [21-23].

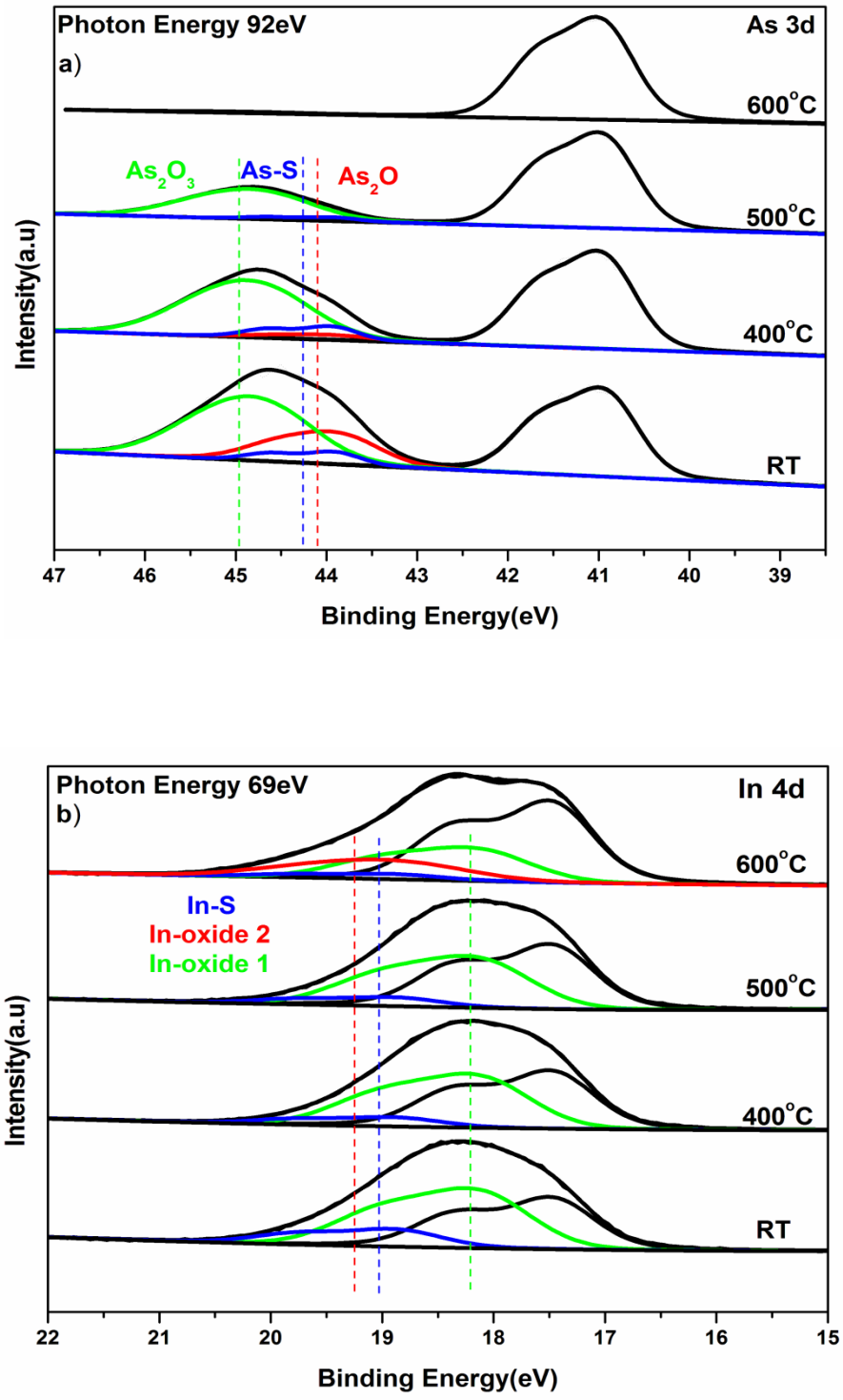

Figure 5.3: (a) Curve fitted As 3d at 92 eV and (b) In 4d at 69 eV of the Al_2O_3 on sulphur passivated InAs surface as a function of post deposition anneals.

The binding energy difference between assigned In-S component at In 4d peak and S 2p of 143.68 eV is consistent for the reported indium sulphide chemical state [21]. Subsequent annealing up to 500^{o}C shows gradual attenuation of both higher oxidation states however 600^{o}C annealing results an additional higher oxidation state shifted to 1.3 eV was attributed to another oxidised indium signal (Indium oxide 2) [11]. Figure 5.4 displays the ratio of oxidation states to bulk substrate peak intensity calculated to precisely quantify the chemical changes during the post deposition anneals. The appearance of additional oxidised indium component (Indium oxide 2) after 600^{o}C annealing treatment could be due to the oxygen transformation from the As^{3+} state. This method of indium oxidation is possible during high temperature thermal anneal since the Gibbs free energies of As_2O_3 is -137.7 kcal/mol and In_2O_3 is -198.6 kcal/mol [24]. The complete attenuation of As_2O_3 and As-S signals were observed at 600^{o}C annealing treatment while previous studies reports complete attenuation of interfacial As-S signal at the HfO_2/GaAs interface after the post deposition anneal at 400^{o}C [25].

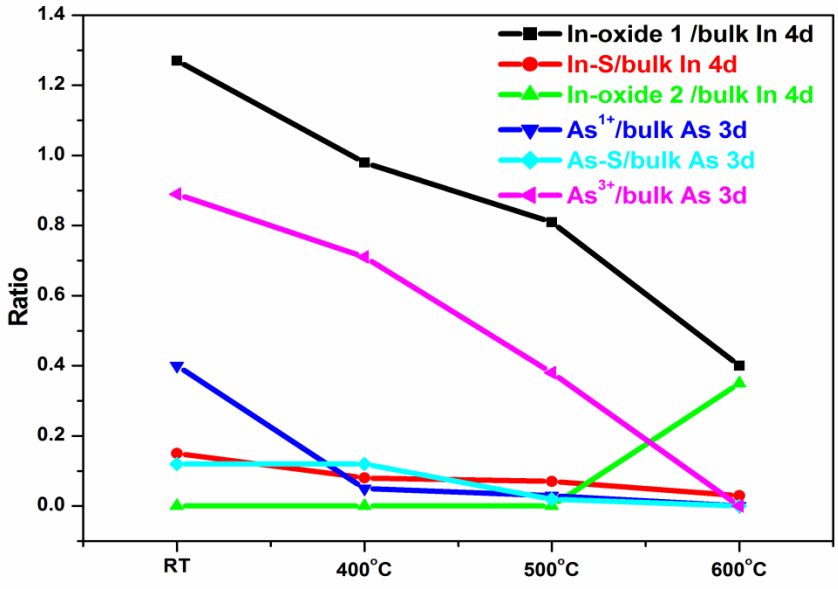

Figure 5.4: Ratio of interface oxidation components to bulk substrate peak for the Al_2O_3/S/InAs structure as a function of post deposition anneals.

Figures 5.5 (a) and (b) shows O 1s and Al 2p spectra at 600 eV and 120 eV and the S 2p spectra taken at 230 eV for the Al_2O_3 deposited on sulphur passivated InAs sample as a function of vacuum anneals.

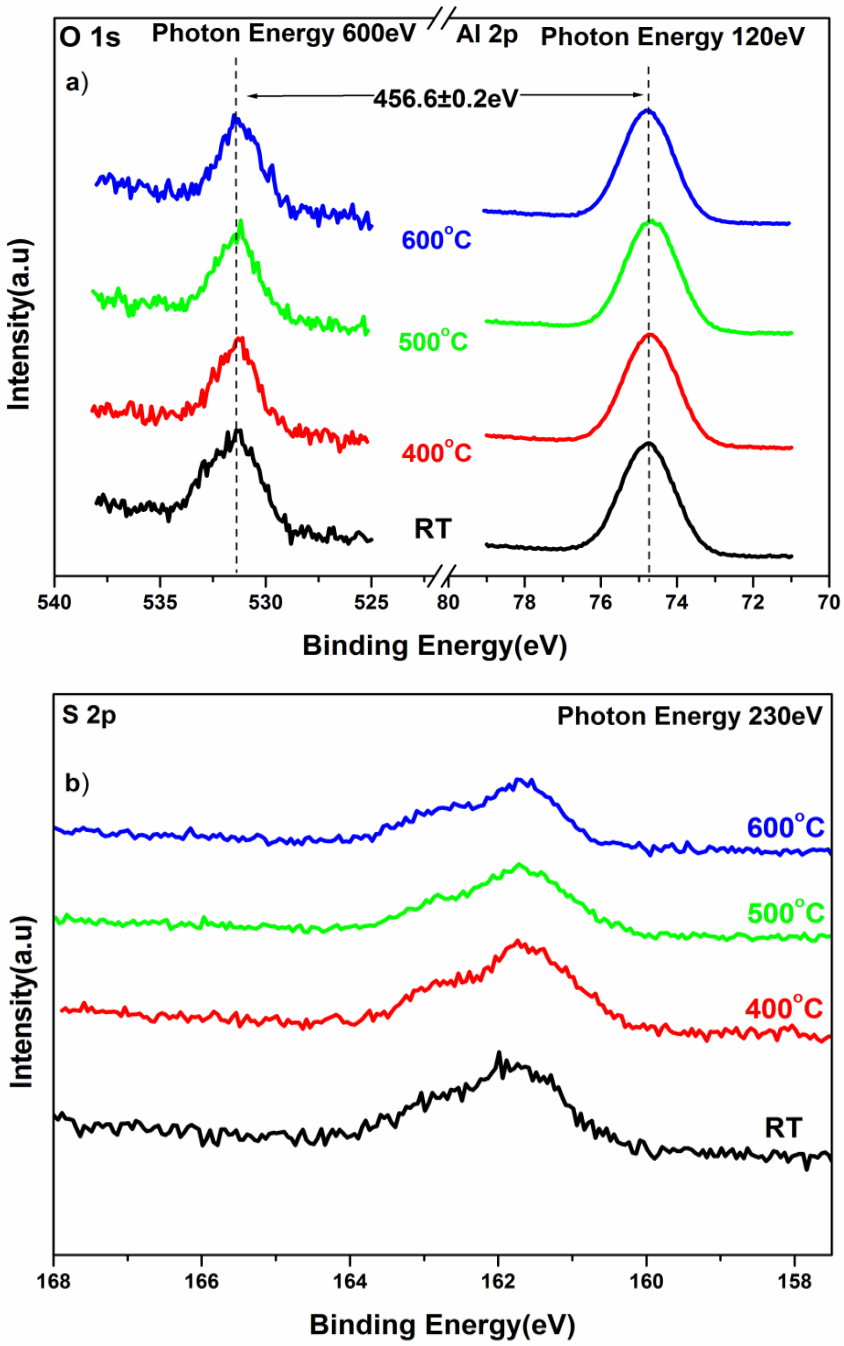

Figure 5.5: (a) displays the O 1s and Al 2p spectra at 600 eV and 120 eV and (b) the S 2p spectra taken at 230 eV of the Al_2O_3 deposited on sulphur passivated InAs sample following subsequent post deposition annealing temperatures.

The Al 2p and O 1s core level peak binding energy difference of 456.6 eV [26] consistent with previously reported energy difference for the stoichiometric Al_2O_3 material however post deposition annealing shows change in binding energy difference not more than ±0.2 eV remains still very close to sapphire [27]. The S 2p taken at 230 eV shows gradual attenuation up to 500^{o}C however subsequent anneal to 600^{o}C still shows sulphur signal which is in contrast with the thermal stability studies of sulphur passivated InAs surface where sulphur was stable up to 500^{o}C. This result suggests that addition of high-κ layer can significantly inhibit complete removal of sulphur from the interface up to 600^{o}C anneal.

5.4 Thermal stability of Al_2O_3 deposited on native oxide covered InAs surface.

The ALD-Al_2O_3 on native oxide InAs surface was also investigated to study any chemical changes induced on this structure without sulphur treatment and as a function of post deposition annealing up to 600^{o}C. Figure 5.6 (a) and (b) shows peak fitted As 3d at 92 eV and In 4d at 69 eV core level spectra of the ultra thin Al_2O_3 deposited on native oxide covered InAs surface for the successive vacuum anneals up to 600^{o}C. The As 3d spectra were fitted with bulk peak and two distinct oxidation states identified as As_2O and As_2O_3 shifted to +2.9 eV and +3.7 eV higher binding energy from the bulk peak at 41 eV consistent with previous literatures [17,18]. Subsequent annealing to 500^{o}C showed attenuation of As^{3+} state with the complete removal of As^{1+} state however further anneal at 600^{o}C resulted in an additional lower binding energy component shifted by -0.64 eV from the bulk peak attributed to dangling bond formation at the interface accompanied with the removal of As^{3+} state. The In 4d spectrum taken at 69 eV was peak fitted with two oxidation states shifted to + 0.65eV higher binding energy from the bulk peak at 17.5 eV was again attributed to oxidised indium (Indium oxide 1) [21,22]. Annealing the sample up to 500^{o}C showed gradual attenuation of the Indium oxide 1 signal. Subsequent anneal at 600^{o}C results increase in higher binding

energy shifted by +1.3 eV from bulk indium peak was identified as Indium oxide 2 signal consistent with the current Al_2O_3/S/InAs study.

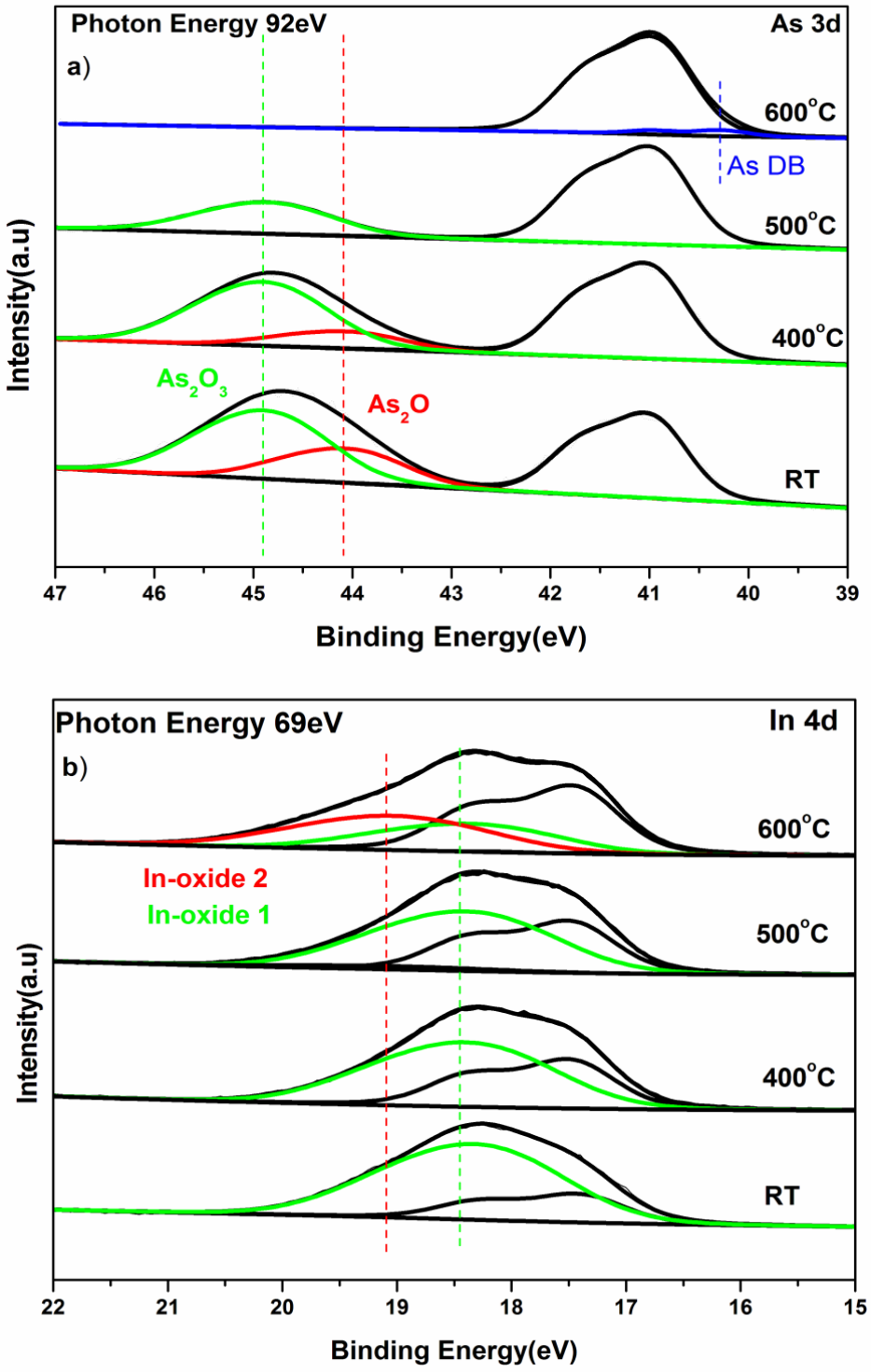

Figure 5.6: (a) Peak fitted As 3d at 92eV and (b) In 4d at 69eV core level spectra of the Al_2O_3 deposited on native oxide covered InAs surface as a function of post deposition annealing treatments up to 600°C.

The ratio estimated for oxide to bulk substrate signal intensity for this Al_2O_3 on native oxide covered InAs sample was shown in figure 5.7. The As^{3+} and As^{1+} states are completely attenuated after 600°C annealing treatment while residual oxidised indium signals were still present.

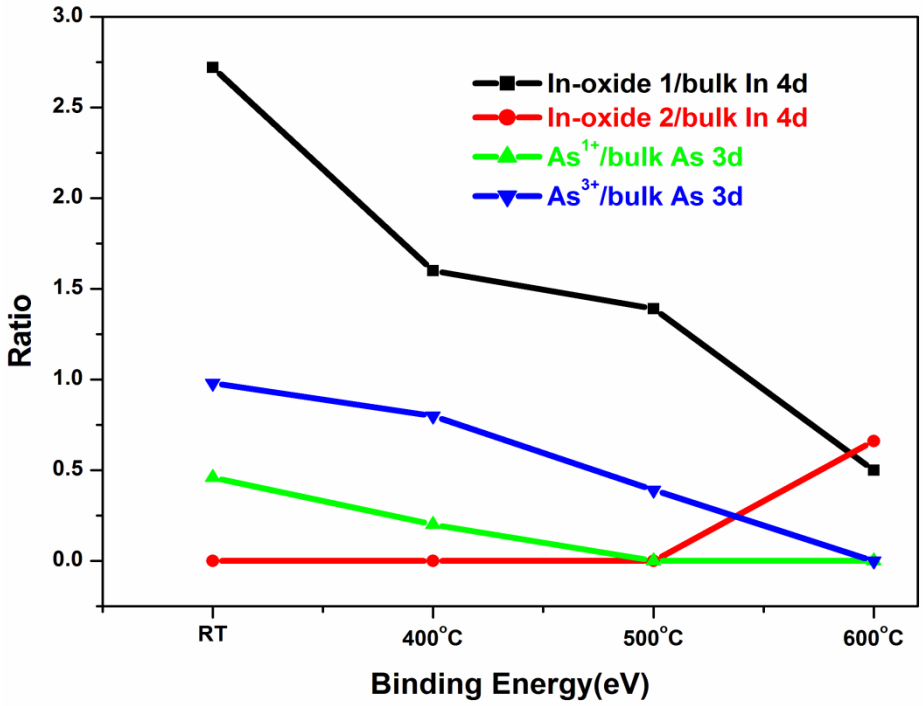

Figure 5.7: Ratio of interfacial oxidation components to bulk substrate peak for the Al_2O_3/InAs structure as a function of post thermal anneals.

5.5 Origin of interfacial oxide-Al_2O_3/S/InAs and Al_2O_3/InAs stacks

The origin of arsenic interfacial oxide formation beneath the Al_2O_3 of native oxide covered and sulphur passivated InAs surface are discussed further. The As 3d and acquired at 92 eV for the Al_2O_3 deposition on before and after sulphur and native oxide covered InAs surfaces are shown in figure 5.8. The As 3d for native oxide InAs surface shows progressive reduction of oxides after the deposition of Al_2O_3. As for the sulphur passivated sample, magnitude of interfacial oxide was increased after the deposition of Al_2O_3 layer. The estimated interfacial arsenic oxide is approximately 0.8 nm which suggests the thickness of interfacial oxide is

independent for both InAs surfaces. Therefore, this interfacial oxide might grown after post air exposure [28].

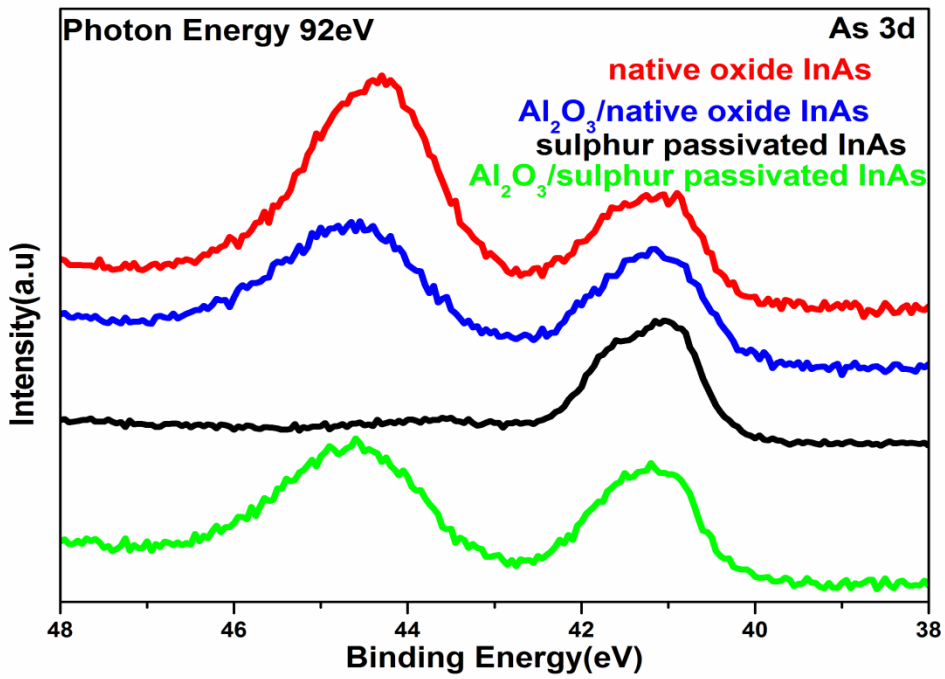

Figure 5.8: As 3d peak acquired at 92eV photon energy for the native oxide (untreated) and sulphur passivated InAs surface before and after Al_2O_3 deposition.

5.6 Energy band offset for Al_2O_3/S/InAs structure

The Valence band (VB) spectra measured at 69 eV for the sulphur passivated InAs surface before and after Al_2O_3 deposition on sulphur passivated InAs surfaces are shown in figure 5.9(a). The sulphur passivated InAs sample results Fermi level position at 0.34 eV above the conduction band minimum assuming a bandgap of 0.36 eV. The valence band minimum (VBM) of sulphur passivated and Al_2O_3 deposited on sulphur passivated InAs surface was extracted as 0.7 eV and 3.51 eV by using linear interpolation method. The valence band offset was estimated as 2.81 eV by substituting the $InAs_{VBM}$ and Al_2O_{3VBM} in the following equation 5.1.

$$\Delta E_V = Al_2O_{3_{VBM}} - InAs_{VBM} \qquad 5.1$$

The conduction band offset was calculated as 3.6 eV by assuming band gap of 0.36 eV and 6.77eV [29] for InAs substrate and Al_2O_3 dielectric material in the below equation 5.2.

$$\Delta E_C = E_g(Al_2O_3) - E_g(InAs) - \Delta E_V \qquad 5.2$$

The calculated valence band offset and conduction band offset are 2.81 eV and 2.45 eV, are represented in the schematic energy band diagram shown in figure 5.9 (b). Thus, conduction and valence band offsets ensure the required barrier to prevent carrier injection into the dielectric bands as suggested by Robertson [30].

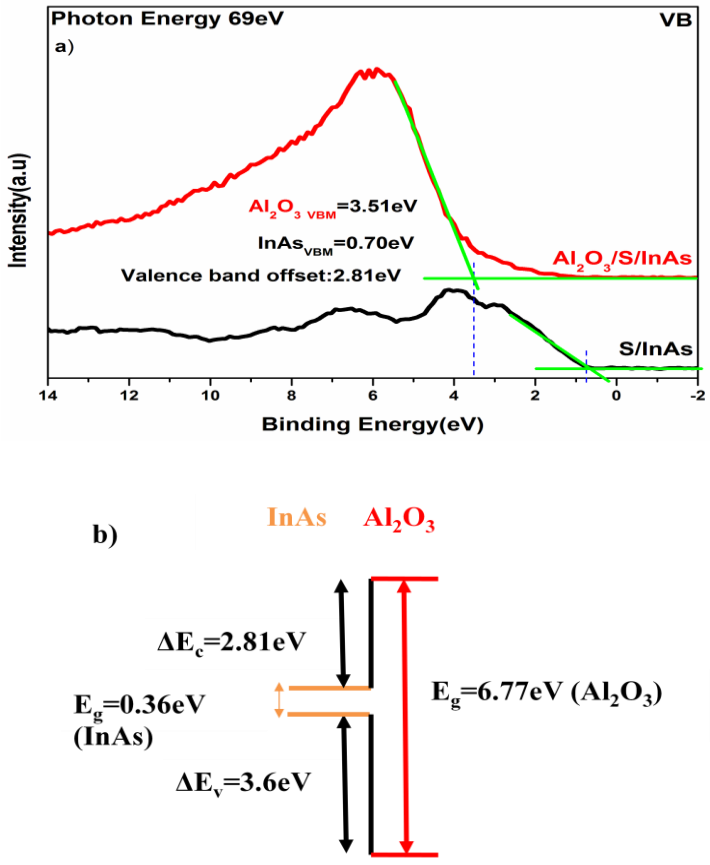

Figure 5.9: (a) Valence band (VB) spectra taken at 69 eV for the sulphur passivated InAs before and after Al_2O_3 deposition sample (b) a schematic energy band diagram showing the calculated VB and CB offsets. Estimated uncertainty in VBM extraction ~ ± 0.1 eV.

5.7 Thermal stability of HfO_2/InAs surface

The As 3d core level acquired at 150 eV is shown in figure 5.10 for the HfO_2 deposited on native oxide covered InAs sample as a function of thermal annealing cycles. The As 3d core level spectra was peak fitted with bulk component at 41 eV and the oxide component was identified as As_2O_3 shifted to 3.5 eV higher binding energy [18].

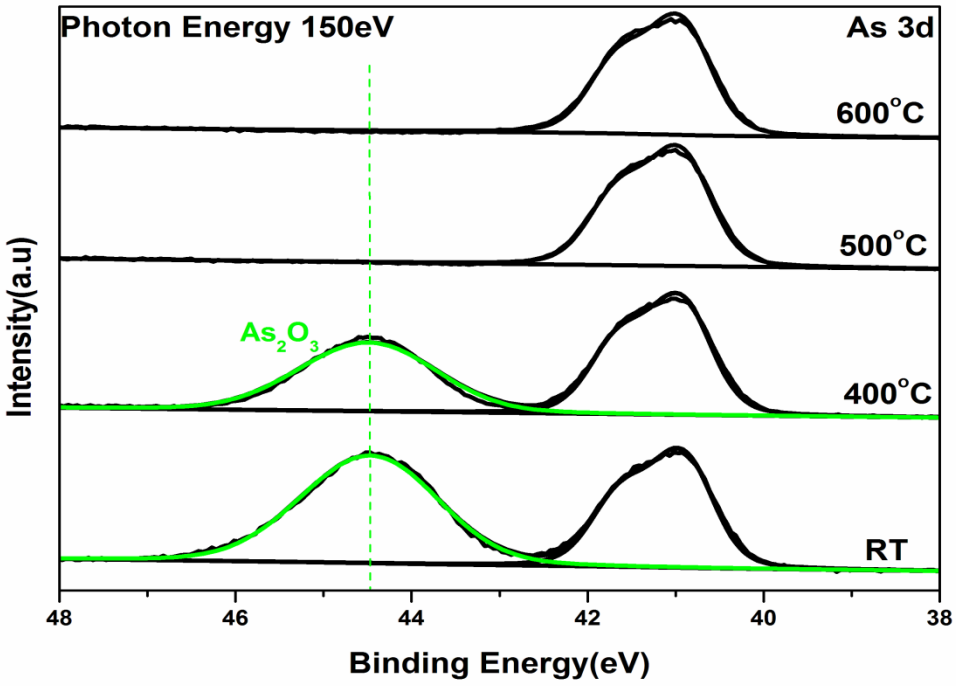

Figure 5.10: Curve fitted As 3d core level spectra acquired at 150 eV photon energy for HfO_2 deposited on native oxide covered InAs surface as a function of post deposition thermal anneals.

Annealing the sample at 400°C reduced the intensity of the As^{3+} state while subsequent annealing at 500°C completely attenuates the As^{3+} signal and results in an arsenic oxide free interface. This complete removal of interfacial arsenic oxide is consistent with the study reported by Trinh et al after the post deposition anneal of HfO_2/InAs structure at 500°C [11]. The corresponding In 4d/Hf 4f core level spectra taken at 69 eV for the HfO_2 deposited native oxide InAs surface and following post deposition annealing are shown in figure 5.11.

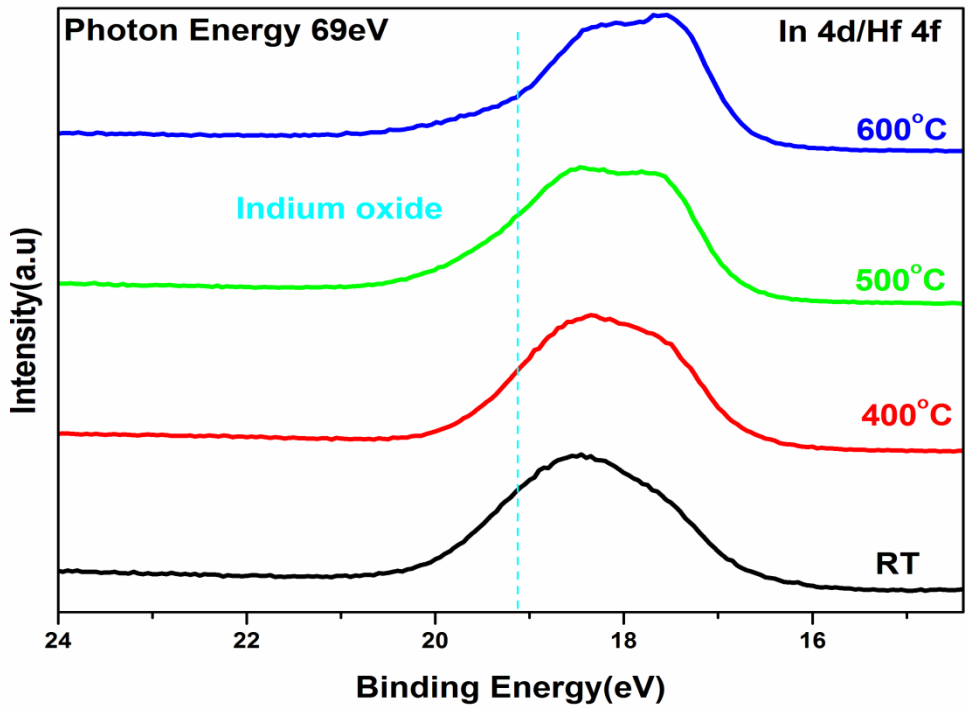

Figure 5.11: In 4d/Hf 4f core level spectra acquired at 69 eV photon energy for the HfO_2/InAs structure following post deposition anneals.

Because of similar binding energy, it is not possible to resolve the individual contributions of the In 4d and Hf 4f to the overall spectral profile, however, the reduction in intensity on the high binding energy side of the peak as a function of anneal is consistent with removal of In oxide components.

The O1s and Hf 4f/In4d core level spectra taken at 600 eV and 130 eV, respectively, for the HfO_2 deposited on native oxide covered InAs surface and for the successive vacuum anneals are shown in figure 5.12. Acquiring the composite Hf 4f/In4d core level at a photon energy of 130eV effectively suppresses the contribution from the In 4d to the extent that the Hf 4f signal dominates the spectrum. The In 4d sub shell photo-ionization cross-section of 0.2813 is much lesser than 6.626 for Hf 4f core level at 130 eV [31]. The binding energy difference between the O 1s and Hf 4f/In4d peaks was 513.2 eV consistent with a stoichiometric HfO_2

layer [32]. The high temperature annealing results in this energy separation changing by no more that ±0.2 eV indicating that the HfO_2 layer remains unchanged by the annealing cycles.

.

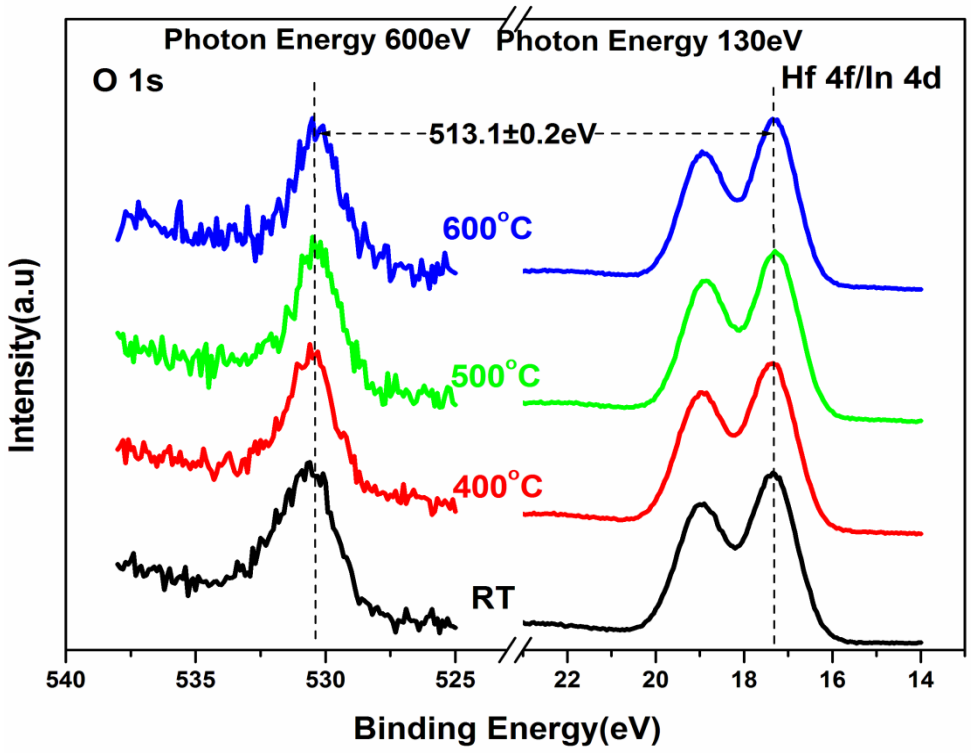

Figure 5.12: O 1s and Hf 4f/In4d core level spectra acquired at photon energies of 600 eV and 130 eV, respectively for the HfO_2/InAs structure and following subsequent anneals.

5.8 Thermal stability of HfO_2/S/InAs structure

The As 3d spectra acquired at 150 eV photon energy for the HfO_2 deposited on the sulphur passivated InAs surface are shown in figure 5.13 for the step wise annealing stages. The As 3d core level peak was curve fitted with a bulk component at 41 eV and higher binding shifted components at +3 eV (As-S) and +3.5 eV (As_2O_3) are consistent with the literature [18,20]. Subsequent annealing up to 500^{o}C results in the gradual attenuation of As-S and As_2O_3 signals, however, interfacial arsenic oxidation components are completely removed at 600^{o}C. This annealing approach is therefore an effective way of removing the interfacial

oxide which could impact on the electrical properties of the interface as previous studies reported that the arsenic oxide free Al_2O_3/InGaAs interface results in unpinning Fermi level behaviour [1]. The presence of interfacial As-S signal after the 500^{o}C anneal is in contrast with the complete attenuation of interfacial As-S after post deposition anneal of Al_2O_3/InGaAs structure in nitrogen ambient at 400^{o}C for 20 s [33].

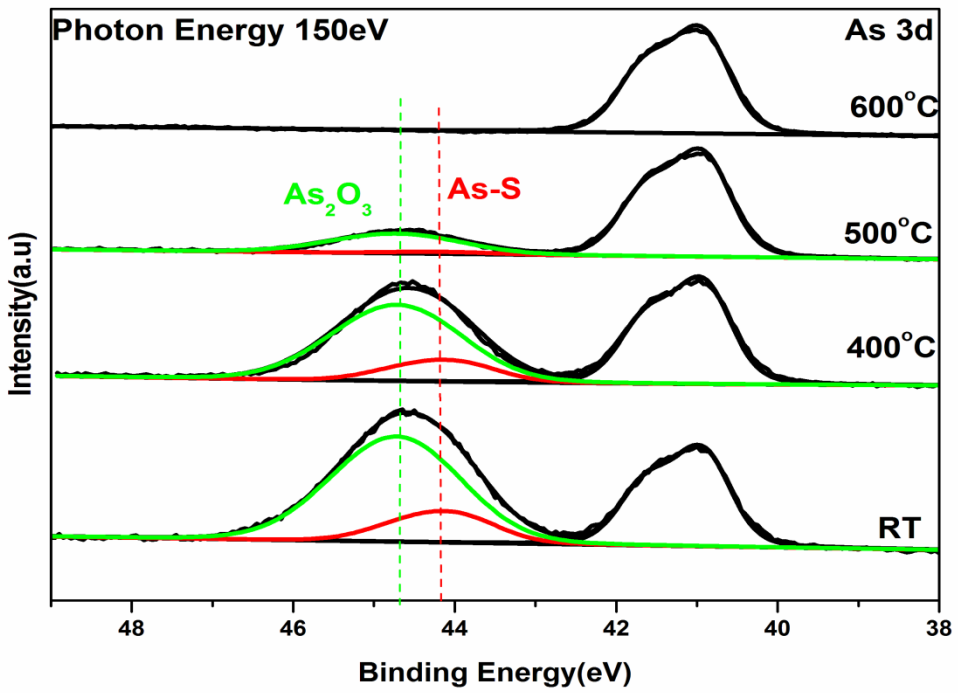

Figure 5.13: Peak fitted As 3d spectra acquired at 150 eV photon energy for the HfO_2 deposited on sulphur passivated InAs surface and following anneals up to 600^{o}C.

The In 4d/Hf 4f core level spectra of the HfO_2 deposited on sulphur passivated InAs surface following thermal anneals acquired at 69 eV are shown in figure 5.14. Again similar to the native oxide covered InAs surface, the interfacial indium components are substantially attenuated during the initial anneals however, even at 600^{o}C evidence of the presence of residual indium oxides can be observed from the high binding energy side of the core level.

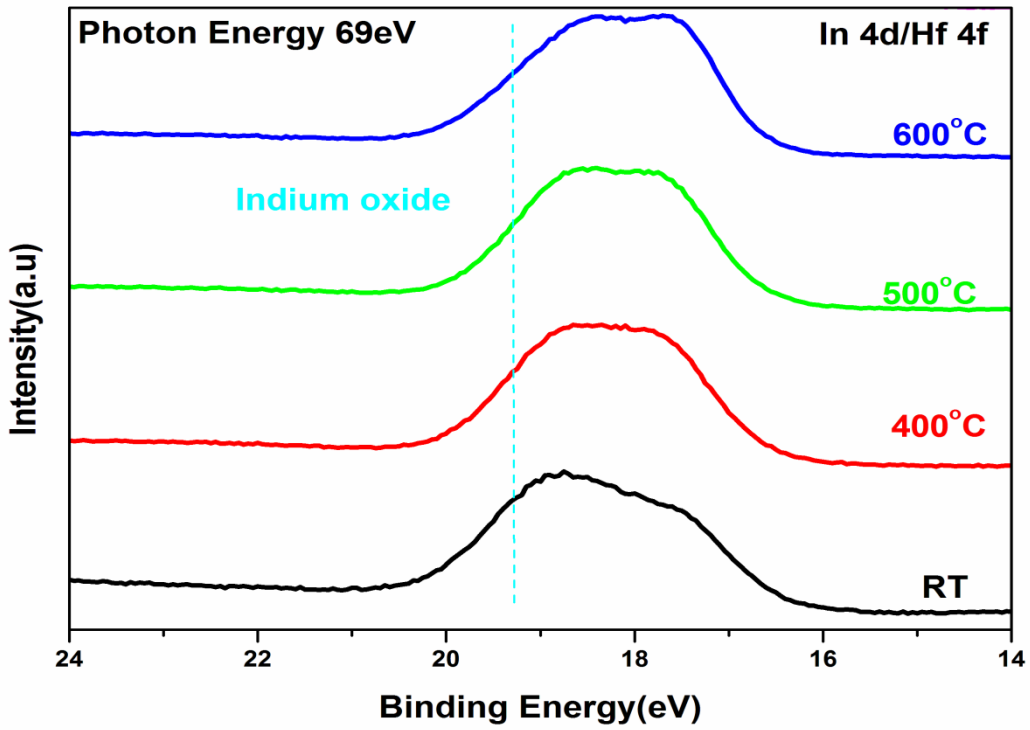

Figure 5.14: In 4d/Hf 4f core level spectra acquired at 69 eV photon energy for the HfO_2/S/InAs structure following post deposition anneals.

The S 2p spectra taken at 230eV are shown in figure 5.15 for the different vacuum anneals.

Annealing the sample up to 600°C results in the gradual attenuation of the sulphur signal,

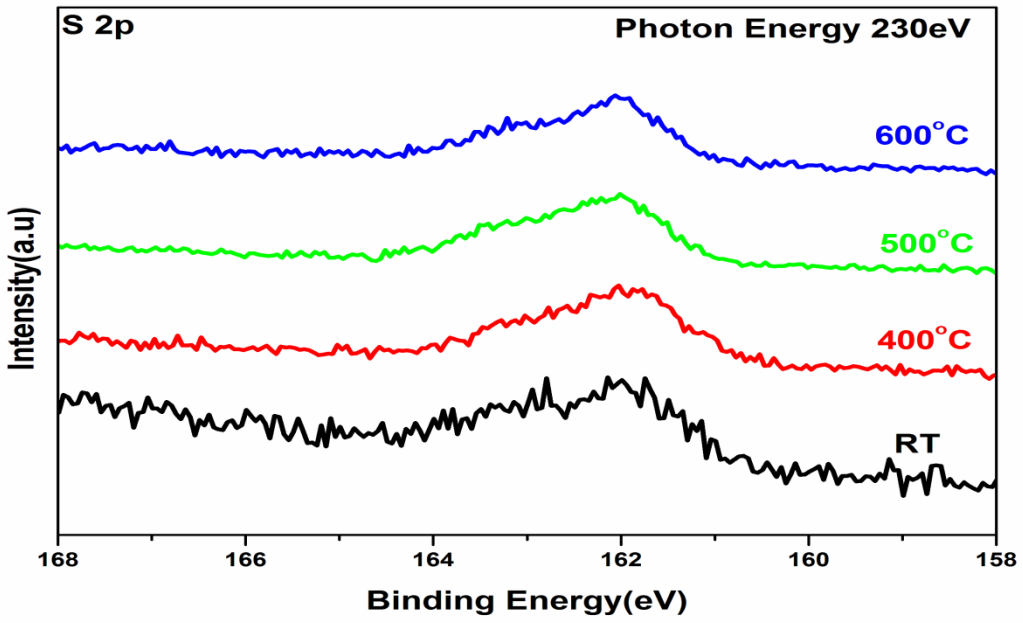

Figure 5.15: S 2p spectra acquired at 230 eV photon energy for the stepwise post annealing treatments.

however this was not completely attenuated which is in contrast with the complete removal of sulphur from the sulphur treated InAs at 430^{o}C [13] similarly in our previous study sulphur was stable up to 500^{o}C for the sulphur passivated InAs without any top high-κ layer. This suggests that the presence of a high-κ layer prevents the desorption of the sulphur from the interface, as previously reported.

5.9 Investigation interfacial oxide for the HfO_2/S/InAs and HfO_2/InAs structures

A comparison between the profile of the As 3d spectra for the sulphur passivated and the native oxide InAs surfaces before and after HfO_2 dielectric layer deposition is shown in figure 5.16. The change in the intensity of the As oxide signal between the native oxide and sulphur passivated surfaces indicates that prior to HfO_2 deposition on the sulphur passivated surface, there was no As oxide component.

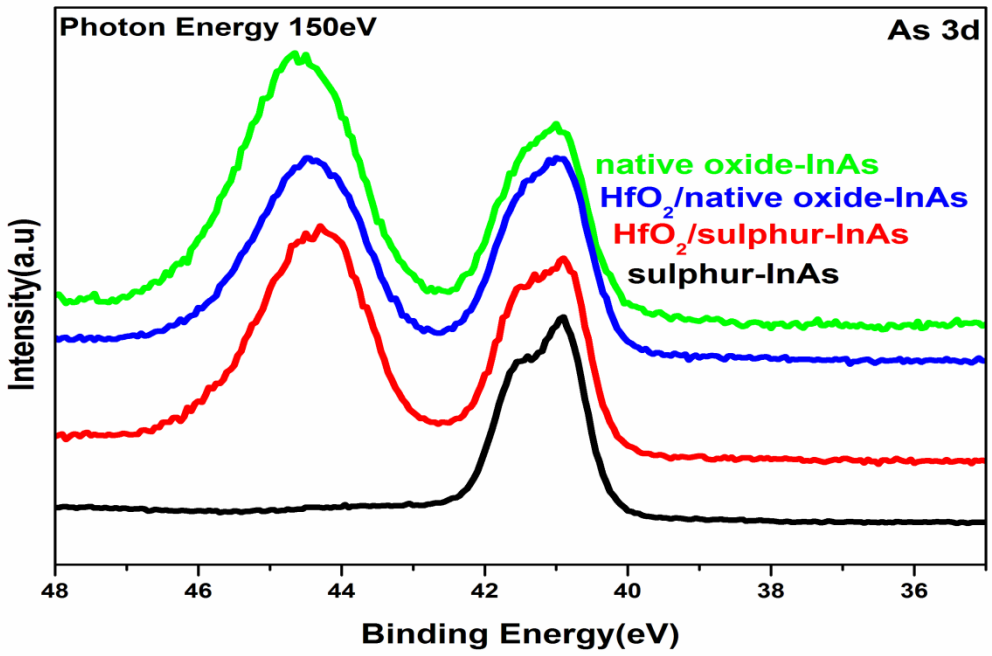

Figure 5.16: As 3d spectra for the sulphur passivated and native oxide covered InAs surface before and after high-κ deposition showing the presence of the interfacial As oxide.

The fact that the interfacial As oxide on both the native oxide and sulphur passivated InAs surfaces following HfO_2 deposition are equivalent in intensity would suggest that the oxide grew to a limiting thickness post deposition, possibly on exposure to ambient conditions [28]. However, the results of this study show that it is possible to effectively remove this interfacial As oxide by post deposition annealing, regardless of whether the InAs surface was subjected to a sulphur passivated treatment in advance of the HfO_2 deposition.

5.10 Energy band offset –HfO2/S/InAs structure

The valence band spectra taken at 69 eV for the sulphur passivated InAs surface before and after HfO_2 deposition are shown in figure 5.17.

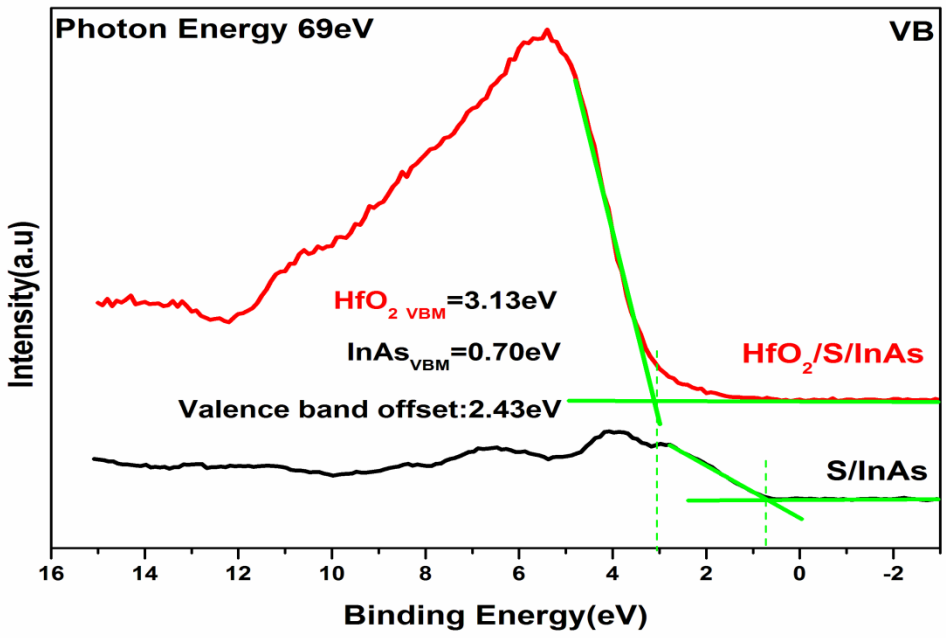

Figure 5.17: Valence band (VB) spectra taken for the sulphur passivated and HfO_2/S/InAs surface at 69eV photon energy. Approximated uncertainty in VBM extraction for both substrate and dielectric is ±0.1 eV.

The valence band maximum (VBM) of the HfO_2 layer was measured to be 3.13 eV below the Fermi level position and the VBM of the sulphur passivated InAs was 0.7 eV, both which were extracted using a linear interpolation method. The Fermi level position at 0.34 eV above

the conduction band minimum for the sulphur passivated InAs surface is consistent with previous studies [10,34]. A valence band offset of 2.43 eV was calculated from the energy difference between VBM of both the substrate and the dielectric layer. The conduction band offset of 2.91 eV was estimated from the following equation 5.3 by assuming an energy gap of 5.7 eV [35] for HfO_2.

$$\Delta E_C = E_g(HfO_2) - E_g(InAs) - \Delta E_V \qquad 5.3$$

The calculated conduction and valence band offsets of 2.91 eV and 2.43 eV are shown in figure 5.18 ensure sufficient barrier for carrier injection as suggested by Roberston [30].

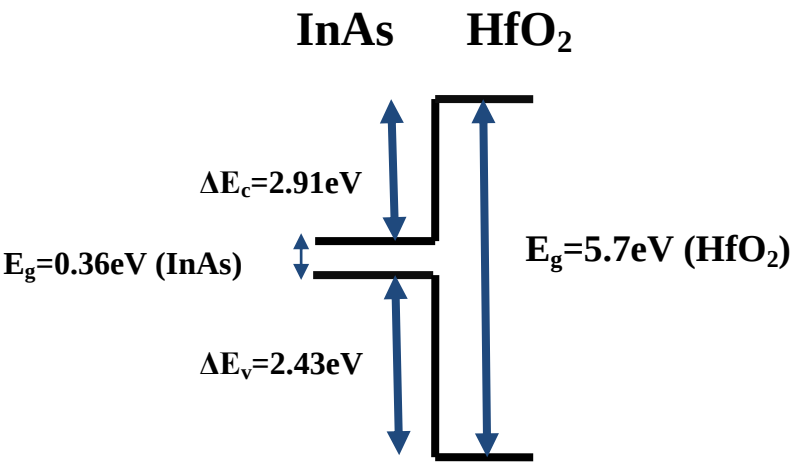

Figure 5.18: Schematic energy band diagram shows CB and VB offsets determined using photoemission spectroscopy measurements.

5.11 Conclusion

Thermal stability of Al_2O_3 and HfO_2 deposited on both sulphur and native oxide InAs surfaces as a function of post deposition anneal up to 600^{o}C were studied using synchrotron radiation based photoemission spectroscopy. The interfacial sulphur components of Al_2O_3 or HfO_2/InAs structure was thermally stable up to 600^{o}C whereas sulphur was completely removed at 600^{o}C from the sulphur treated InAs surface without any dielectric layer. These results show an effective way to substantially remove the interfacial oxide at 600^{o}C without

affecting dielectric stoichiometry which could have implications for the development of n-MOS device performance. The energy band offset estimated using photoemission measurements ensure effective barrier to inhibit carrier injection.

5.12 References

[1]. M. L. Huang, Y. C. Chang, C. H. Chang, Y. J. Lee, P. Chang, J. Kwo, T. B. Wu, and M. Hong Appl. Phys. Lett. 87, 252104 (2005).

[2]. Y. C. Chang, M. L. Huang, K. Y. Lee, Y. J. Lee, T. D. Lin, M. Hong, J. Kwo, T. S. Lay, C. C. Liao and K. Y. Cheng, Appl Phys. Lett. 92, 072901(2008).

[3]. V. Martinelli, L. Siller, M. Garzia Betti, C. Mariani, and U. del Pennino, Surf. Sci. 391, 73 (1997).

[4]. I. Aureli, V. Corradini, C. Mariani, E. Placidi, F. Arciprete, and A. Balzarotti, Surf. Sci. 576, 123 (2005)

[5]. Y. Lyadov, R. Akhvlediani, A. Hoffman, O. Klin, and E. Weiss J. Appl. Phys. 107, 053518 (2010)

[6]. C. -L. Chang, V. Shuttanadan, S. C. Singhal, and S. Ramanathan, Appl. Phys. Lett. 90, 203109 (2007)

[7]. G.R. Bell, N.S. Kaijaks, R.J. Dixon, C.F. McConville Surf Sci. 401 125–137(1998).

[8]. T. D. Veal and C. F. McConville, Appl. Phys. Lett. 77, 1665 (2000)

[9]. R. K. Chellappan, Z. Li, and G. Hughes. Appl. Surf. Sci. Volume 276, 609 (2013).

[10]. D.Y. Petrovykh, M. J. Yangb, L. J. Whitman. Surf. Sci. 523.3 231-240(2003).

[11]. H. Trinh, Y. Lin, H. Wang, C. Chang, K. Kakushima, H. Iwai, T. Kawanago, Y. Lin, C. Chen, Y. Wong, G. Huang, M. Hudait, and E.Y. Chang Appl. Phys. Exp. 5, no. 2 021104-021104(2012).

[12]. H. C. Lin, W. E. Wang, G. Brammertz, M. Meuris, M. Heyns, Microelec. Engg 86, 1554, (2009).

[13]. M. Katayama, M. Aono, H. Oigawa, Y. Nannichi, H. Sugahara and M. Oshima Jpn. J. Appl. Phys. 30 pp. L786-L789 (1991).

[14]. C. Weiland, P. Lysaght, J. Price, J. Huang, and J. C. Woicik, Appl. Phys. Lett.101, 061602, (2012).

[15]. O. Ceballos-Sanchez, A. Sanchez-Martinez, M. O. Vazquez-Lepe, T. Duong, R. Arroyave, F. Espinosa-Magaña, and A. Herrera-Gomez, J. Appl. Phys. 112, 053527, (2012).

[16]. E. Martinez, H. Grampeix, O. Desplats, A. Herrera-Gomez, O. Ceballos-Sanchez, J. Guerrero, K. Yckache, F. Martin Chemical Physics Letters, Vol. 539-540, pp. 139-143(2012).

[17]. T. Ishikawa and H. Ikoma Jpn. J. Appl. Phys. 31 pp. 3981-3987(1992).

[18]. M. Beerbom, T. Mayer, W. Jaegermann, D. R. Batchelor, and D. Schmeier, Anal. Bio. anal. Chem. 374, 650 (2002).

[19]. J. Yota and V. A. Burrows J. Vac. Sci. Technol. A 11, 1083 (1993)

[20]. C. J. Sandroff, M. S. Hegde, and C. C. Chang J. Vac. Sci. Technol. B 7, 841 (1989)

[21]. I. Konovalova and L. Makhova J. Appl. Phys. 103, 093721 (2008)

[22]. A. P. Kirk, M. Milojevic, J. Kim, and R. M. Wallace Appl. Phys. Lett. 96, 202905 (2010).

[23]. L. Lai, Jiun-Ting Chen, L Lou,C. Wu and C. Lee, Journal of The Electrochemical Society, 155,12,B1270, (2008)

[24]. C.L. Hinkle, E.M. Vogel, P.D. Ye and R.M. Wallace Curr. Opin. Solid State Mater. Sci. 15 188(2011).

[25]. R. Suri, D.J. Lichtenwalner and V.Misra Appl.Phys.Lett.92,243506(2008).

[26]. Chao-Ching Cheng, Chao-Hsin Chien, Guang-Li Luo, Jun-Cheng Liu, Chi-Chung Kei, Da-Ren Liu, Chien-Nan Hsiao, Chun-Hui Yang and Chun-Yen Chang J. Electrochem. Soc ,155, G208 (2008).

[27]. C. S.Yang, J.S. Kim, J.W. Choi, M.H.Kwon, Y. J. Kim, J. G. Choi, and Kim, G. T. J. Indust and Eng. Chem,6(3), 149-156, (2000).

[28]. R. Timm, A. Fian, M. Hjort, C. Thelander, E. Lind, J. N. Andersen, L.-E. Wernersson, and A. Mikkelsen, Appl. Phys. Lett. 97, 132904 (2010).

[29]. M. L. Huang, Y. C. Chang, Y. H. Chang, T. D. Lin, J. Kwo, and M. Hong Appl. Phys. Lett. 94, 052106 (2009)

[30]. J. Robertson, Eur. Phys. J. Appl. Phys. 28, 265–291 (2004).

[31]. J.J.Yeh and I.Lindau,Atomic data and nuclear data tables 32,1-55(1985).

[32]. K. Cherkaoui, S. Monaghan, M. A. Negara, M. Modreanu, P. K. Hurley, D. O'Connell, S. McDonnell, G. Hughes, S. Wright, R. C. Barklie, P. Bailey and T. C. Q. Noakes. Journal of Appl. Phys. 104, 064113(2008).

[33]. J.Hu and H. S. Philip Wong, J.Appl.Phys.111, 044105 (2012).

[34]. Y. Fukuda, S. Ichikawa, M. Shimomura, N. Sanada, Y. Suzuki, Vacuum. 67, 38 (2002).

[35]. M. Perego, G. Seguini and M. Fanciulli. Materials Science in Semiconductor Processing 11, 221-225(2008).

6 Analysis of interface preparation on $Al/Al_2O_3/Ge$ MOS capacitor characteristics

This chapter presents the effect of sulphur passivation on tuning chemical and electrical properties of metal/Al_2O_3/Ge MOS stacks and discusses the electrical and chemical impact of alcohol based sulphur passivation treatments on germanium MOS structures. The systematic electrical studies of post deposition annealing in oxygen are also presented.

6.1 Sulphur passivation with different pre-cleaning methods of $Al_2O_3/S/Ge$ gate stacks

The presence of native germanium oxides at the high-κ/Ge interface could result in interfacial defect states and an increase in the equivalent oxide thickness (EOT). Previous report suggests that the direct deposition of high-κ on germanium substrates without any passivation layers results in poor electrical characteristics due to the following issues

1. First principle study shows metal interaction of germanium substrate during high-κ deposition creates defect states at the Ge band gap [1].
2. Undesirable interfacial germanium oxide could pin the Fermi level in the band gap [2].
3. Diffusion of germanium into the high-κ material may form a pathway for high leakage current [3].
4. Intermixing of interfacial germanium oxide and the high-κ material can reduce the overall EOT of the device [4].

Therefore passivation of the germanium surface is one of the possible methods of avoiding the aforementioned issues. This chapter discusses the effectiveness of sulphur passivation on the electronic and chemical properties of germanium surfaces.

6.1.1 Gate stack preparations

The p-type native oxide germanium samples with a doping density of 4×10^{17} cm^{-3} were treated with following pre-cleaning methods.

1. HBr: HCl (10:1) for 4 mins, final HBr rinse.
2. NH_4OH (10%), H_2O_2 (6%), Methanol, water for 2 times, final NH_4OH rinse.
3. Native oxide germanium surface (reference sample).

Subsequently these substrates were passivated with sulphur using ammonium sulphide $(NH_4)_2S:H_2O$ (1:10) for 20 minutes at 70-80^oC with a final rinse in water and dried with N_2. Metal oxide semiconductor (MOS) device structures were fabricated by deposition Al_2O_3 (9 nm) using tri-methyl aluminium (TMA) and water as precursors at 250^oC substrate temperature on these treated surfaces. Aluminium metal (~ 100 nm) contacts diameter of ~ 355 µm were deposited using shadow mask on the front and subsequently the back contacts were made using the same metal. Finally, the samples were annealed in a forming gas ambient. A schematic diagram of sample preparation is shown in figure 6.1.

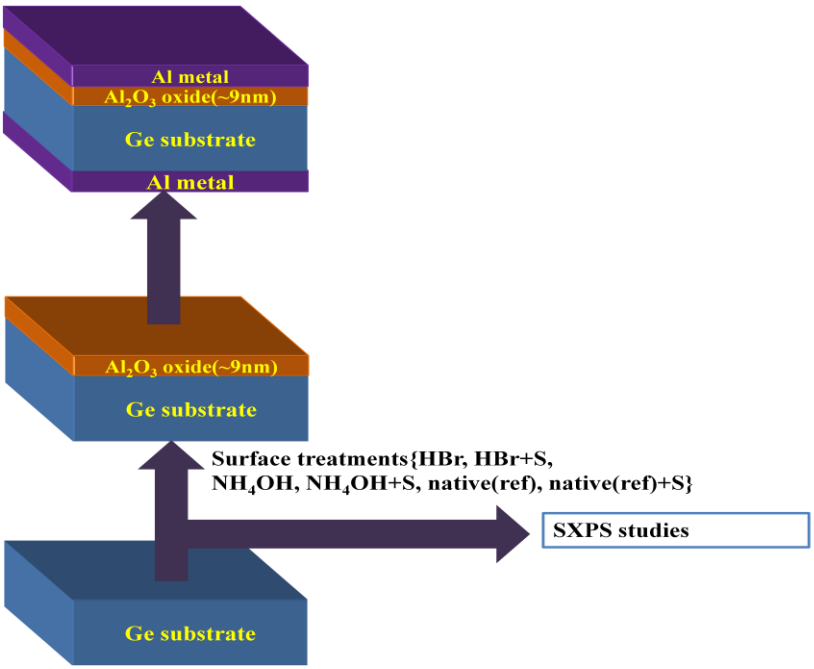

Figure 6.1: Schematic diagram showing MOS preparations.

6.1.2 SXPS studies of sulphur passivation of germanium surfaces

The Ge 3d spectra acquired at a photon energy of 130 eV for the native oxide covered germanium surface and as a function of thermal annealing is shown in figure 6.2 (a). The higher binding energy peak at 33.5 eV binding energy is attributed to germanium-oxygen interactions and these signals were not significantly attenuated in the annealing sequence up to 350^{o}C.

The equivalent Ge 3d spectra following the sulphur passivation of the native oxide covered germanium surface are shown in figure 6.2 (b). There is clear evidence that this treatment is effective at removing the native oxide signal and the higher binding energy signal is attributed to residual oxides and sulphur bonding interactions. Figure 6.2 (c) shows that the HBr treated results in almost complete removal of the residual oxides from the germanium surface which is consistent with previous studies [6]. The annealing of the Br passivated germanium surface at 350^{o}C shows a significant attenuation of the Br 3d signal acquired at 130eV photon energy as shown in figure 6.3. Previous studies have reported that the HBr treatment is effective at both removing oxides and preventing the germanium surface from re-oxidation even after 6 hours of exposure in air [7]. The Ge 3d spectra taken after sulphur passivation of this HBr treated germanium surface are shown in figure 6.2 (d). The intensity of higher binding signal was significantly attenuated by the bonding interaction of sulphur and germanium however Ge-S signal was thermally stable up to 350^{o}C. The absence of Ge-Br state was confirmed from the Br 3d peak after sulphur passivation. The Ge 3d spectra of the ammonium hydroxide based pre-cleaning treatment shown in figure 6.2 (e) indicate that it is not effective at completely removing the germanium oxides from the surface.

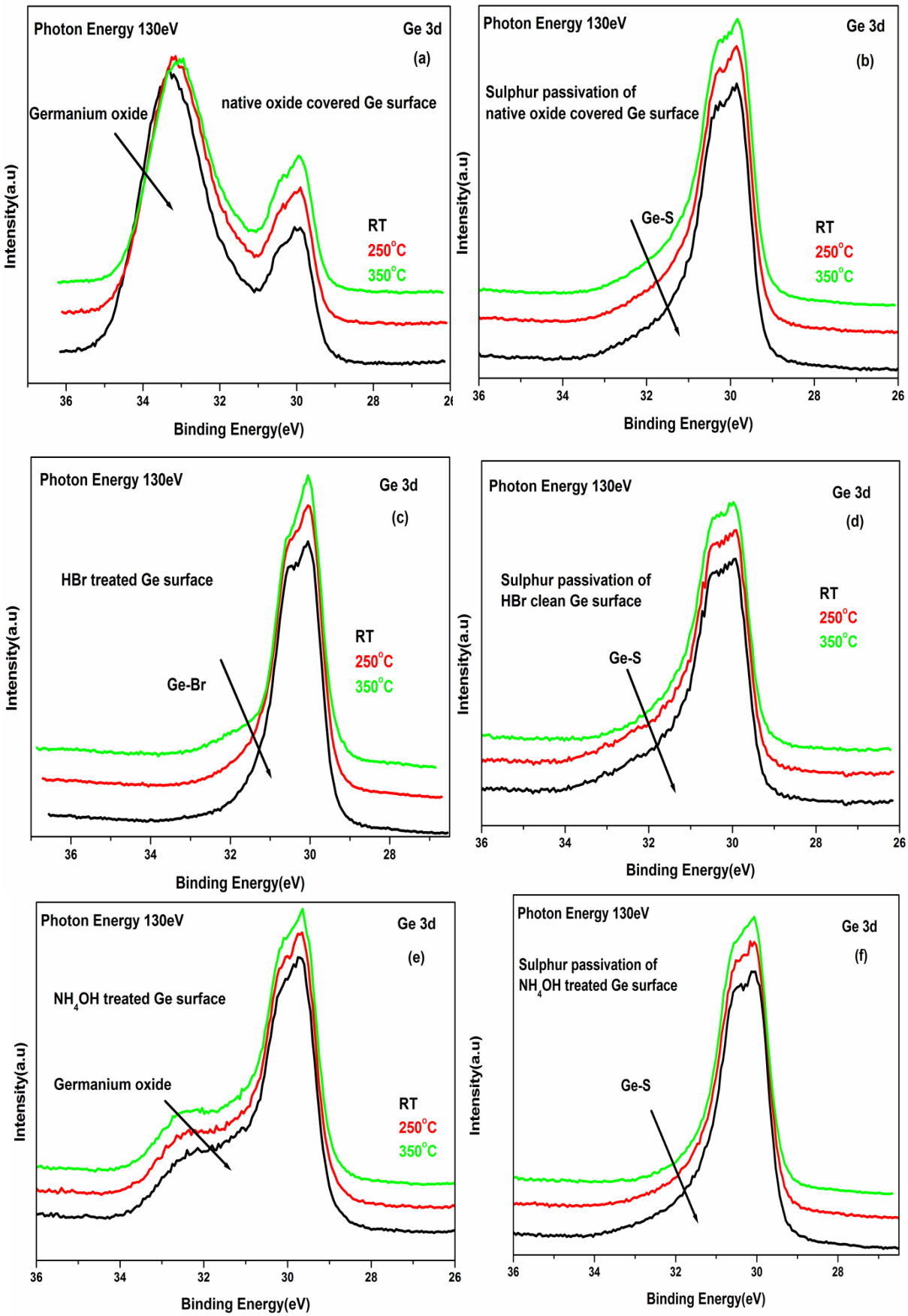

Figure 6.2: Ge 3d spectra for the (a) native oxide (b) sulphur passivation on native oxide Ge surface (c) HBr treated(d) Sulphur passivation on HBr treated Ge surface (e) NH_4OH treated and (f)sulphur passivation on NH_4OH pre treated Ge surface as a function of thermal anneal.

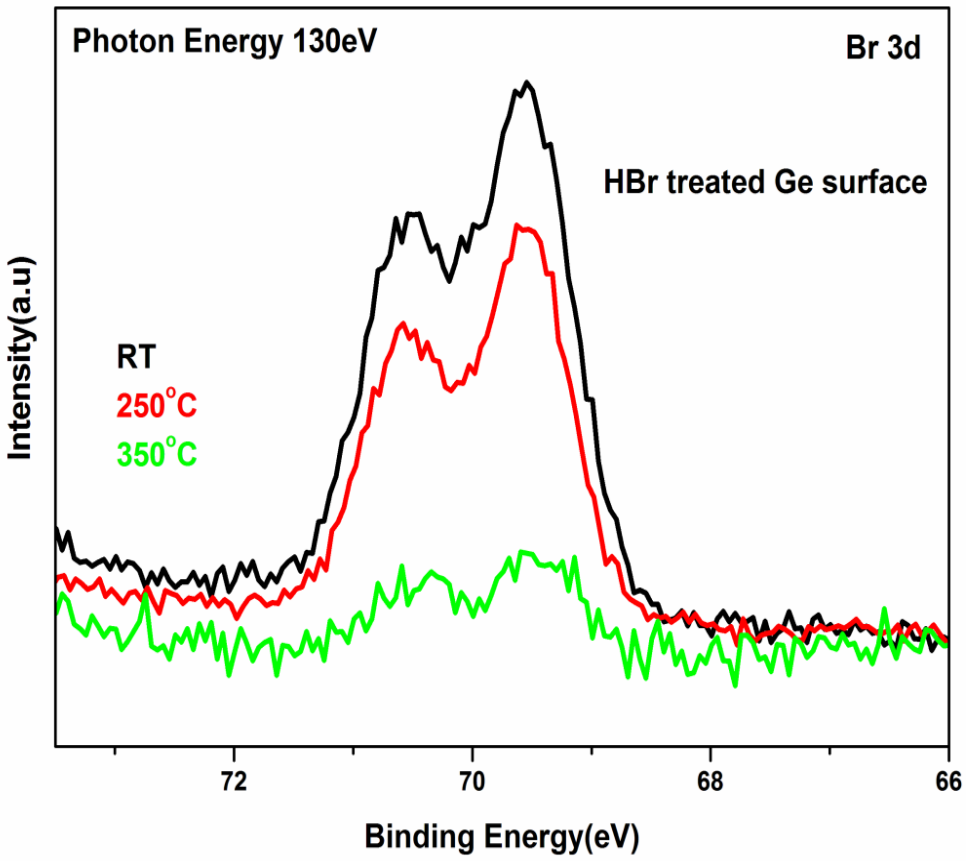

Figure 6.3: Br 3d spectra for the HBr pre-treated germanium surface.

The subsequent sulphur passivation of this surface shown in figure 6.2 (f) indicates that the residual oxide can be removed to produce a surface similar to the sulphur passivated native oxide sample.

The S 2p spectra acquired at a photon energy of 230 eV for the sulphur passivation of (a) the native oxide (b) HBr pre-clean and (c) NH_4OH treated germanium surfaces at successive anneals upto 350^{o}C are shown in figure 6.4. The S 2p spectra show similar attenuation with annealing irrespective of the pre-cleaning step suggesting that the different surfaces are similarly sulphur terminated.

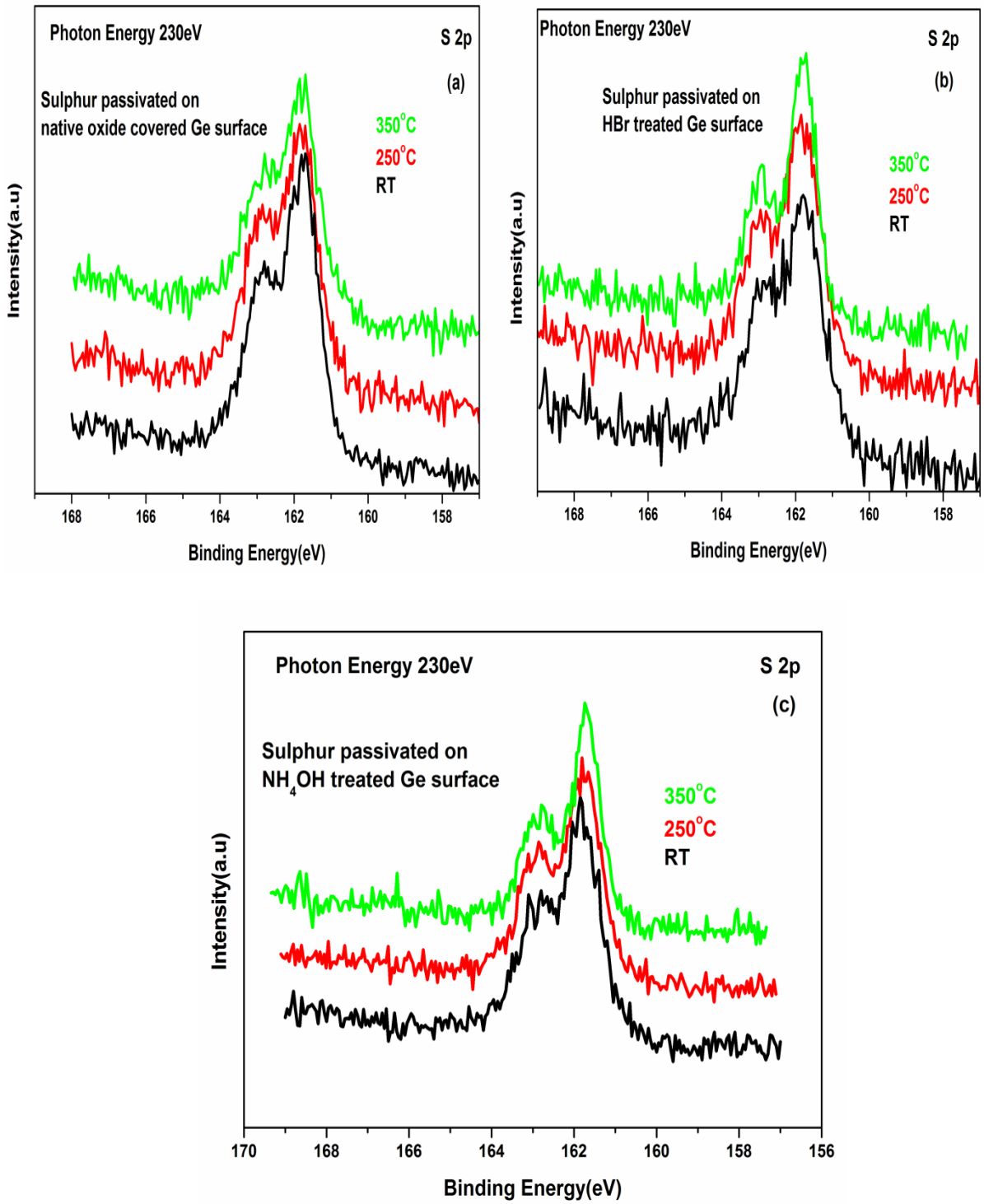

Figure 6.4: S 2p spectra for the various sulphur passivated (a) native oxide (b) HBr and (c) NH_4OH germanium samples as a function of thermal anneals.

The bidirectional capacitance-voltage (CV) measurements for a frequency of 1MHz for the Al_2O_3/Ge MOS capacitor structures are shown in figure 6.5 for (a) native oxide and following sulphur passivation (b) HBr treated and sulphur passivated and (c) NH_4OH treated and sulphur passivated.

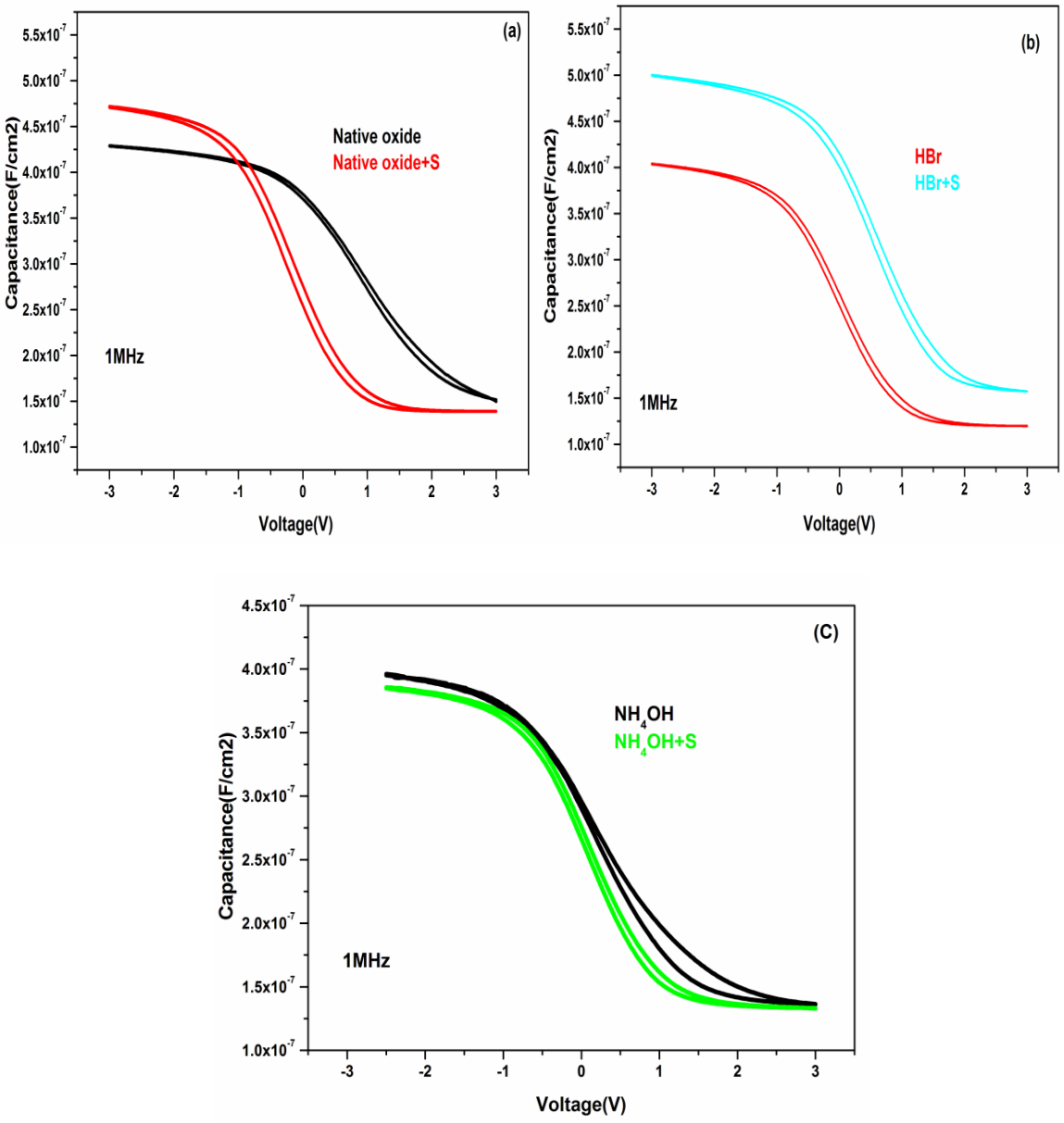

Figure 6.5: 1 MHz bi-directional CV Sweep for (a) native oxide and sulphur passivation on native oxide Ge surface (b) HBr treated and Sulphur passivated on HBr pretreated Ge surface (c) NH_4OH treated and Sulphur passivated on NH_4OH pretreated Ge surface.

The interfacial defect state density (D_{it}) for the MOS capacitors with and with out sulphur treatments are listed in table 6.1. The D_{it} density was significantly reduced with sulphur passivation suggesting the effectiveness of sulphur in saturating the defect states compare to unpassivated germanium samples.

Samples	Interfacial state density($eV^{-1}cm^{-2}$)
HBr	2.8×10^{12}
HBr+S	6.50×10^{11}
NH_4OH	3.7×10^{12}
NH_4OH+S	6.32×10^{11}
Native(ref)	8.81×10^{12}
Native(ref)+S	4.85×10^{11}

Table 6.1: Showing D_{it} extracted the various chemical treated Ge MOS stacks.

6.2 Alcohol based sulphur passivation

There are several reports which suggest that sulphur passivation is effective in improving the electrical properties of MOS devices [2,5]. The sulphur passivation is usually achieved on germanium by treating with an ammonium sulphide (10%) solution diluted with water (90% by volume).

Previous studies have suggested that the sulphur coverage of passivated gallium nitride surfaces could be varied by treating with ammonium sulphide solutions (10%) diluted in alcohols (90%) of different dielectric constants (methanol > ethanol > IPA > tert-butanol). This systematic study investigates the chemical and electrical impact of sulphur passivation of germanium using ammonium sulphide solutions (10%) diluted with alcohols (90%) such as methanol, ethanol, iso-propyl alcohol and tert-butanol at 60-70^{o}C for 20 minutes. Prior to sulphur passivation, the germanium surfaces were pre-cleaned with cyclic rinses of NH_4OH, H_2O_2, methanol and water. Rinsing the germanium surface in NH_4OH [8] has been reported

to minimize carbon and oxide contaminants while the subsequent rinse in H_2O_2 solution results in oxidation of the surface which is removed by the final methanol ,water and NH_4OH rinses. MOS structures were fabricated by depositing Al_2O_3 (~ 9 nm) by ALD on the sulphur treated surfaces followed by subsequent front and back side Al (~ 100 nm) metallization. The S 2p spectra at 230 eV measured for the sulphur passivated germanium samples with various alcohols are shown in figure 6.6.

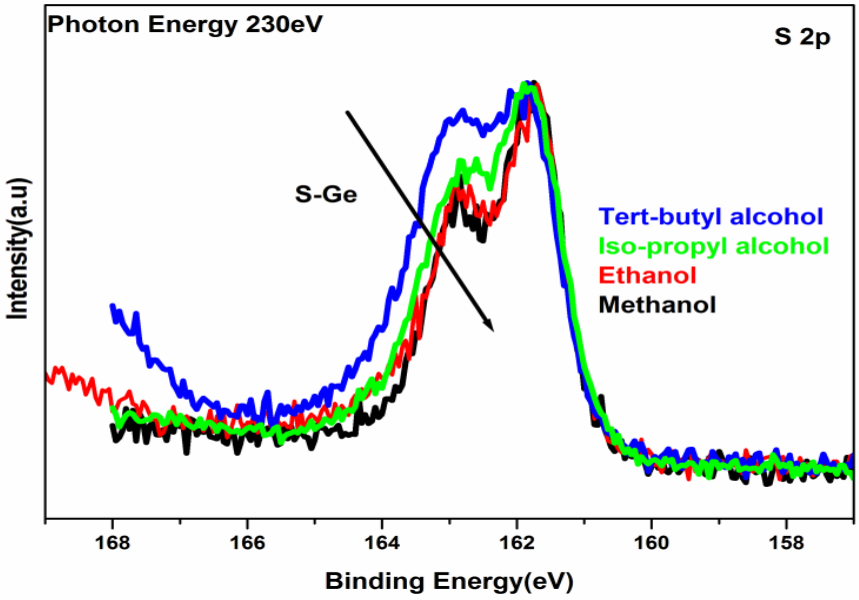

Figure 6.6: S 2p peak shows sulphur passivation of germanium surfaces by ammonium sulphide diluted as function of alcohols.

The increased intensity of the signal on the higher binding energy side of the S 2p peak with decreasing dielectric constant of the alcohol is attributed to the presence of a second chemical state of sulphur bonded to the germanium surface consistent with previous studies [10].

The Ge 3d spectra acquired at 130 eV for the respective alcohol based sulphur passivations are shown in figure 6.7. The higher binding energy component attributed to sulphur bonding interactions shows the same trend as that displayed by the S 2p signal in that as the dielectric constant of the alcohol reduces, so does the sulphur bonding interaction.

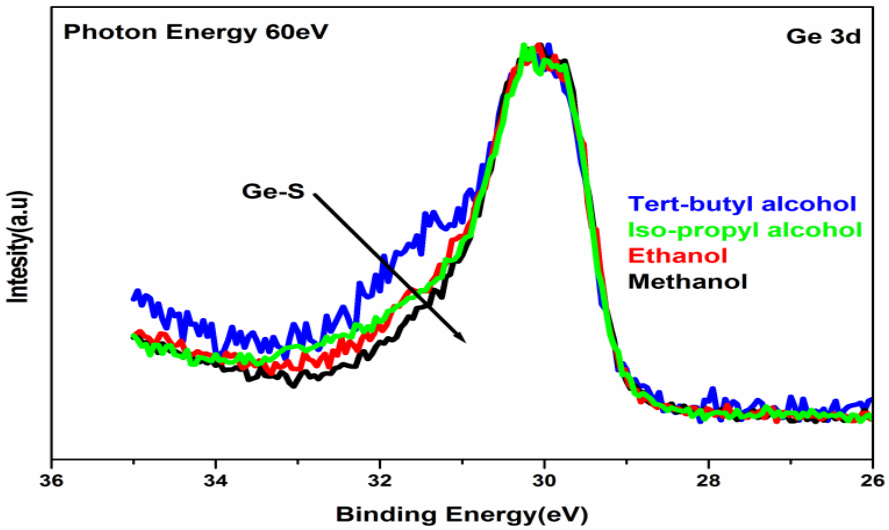

Figure 6.7: Ge 3d peak taken at 60 eV for the sulphur passivated germanium samples as a function of various alcohols.

The 1 MHz bi-directional CV measured on the MOS capacitors fabricated on these sulphur passivated germanium surfaces are shown in figure 6.8.

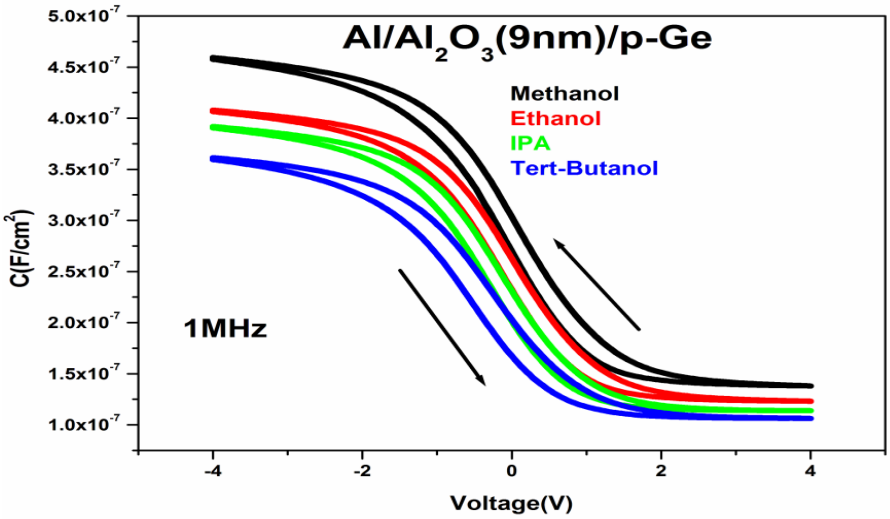

Figure 6.8: 1 MHz CV Sweep for the sulphur passivated Ge-MOS stacks as function of alcohols.

There is a clear trend in the C_{max} values of capacitance with the alcohol dielectric constant matching the systematic changes seen in the XPS studies, however the origin of these changes are not obvious and require further investigation. The estimated D_{it} for the sulphur passivated germanium surface using conductance method was approximately 5E11 eV^{-1} cm^{-2}.

6.3 Post deposition annealing in oxygen ambient

Several surface passivation procedures such as sulphur [5] and rare-earth oxides passivations [11], Si interlayer [12], nitridation [13,14] plasma [16] and thermal oxidation [17] treatments have been studied to perfect the dielectric-semiconductor interface in terms of minimizing the interface state density. Recently high performance Ge-MOSFET device performance has been demonstrated with a thermally grown GeO_2 passivation layer [18]. However a major issue in the thermal growth of a GeO_2 layer is the desorption of GeO species at temperatures > 420^oC from the surface which may lead to high defect state densities [19,20]. To address this issue, it has been proposed that a high pressure high temperature oxidation process can be used to control the GeO volatilization by reducing the vapour pressure of GeO at the GeO_2 surface [11]. The thickness of the germanium oxide layer can be controlled by tuning the parameters such as processing time, temperature and oxygen pressure [21]. However, direct deposition of ALD high-κ layer on GeO_2/Ge structure might chemically affect the GeO_2 layer and create large interfacial defect state densities. A plasma based post oxidation treatment process has been shown to result in the growth of a thin GeO_x layer at the Al_2O_3/Ge interface with the alumina limiting the GeO_x thickness [15,16]. Therefore this study examines the electrical and chemical impact due to high pressure post oxygen treatment on the Al_2O_3/Ge interfaces. The re-growth of oxide on germanium surfaces is reported to vary with surface cleaning methods. However, the presence of sulphur in the interfacial GeO_x layer can reduce the concentration of interface defect states. The chemical treatments of germanium samples are as follows

1. HF:H_2O (1:10) for 2 mins then final water rinse.
2. HBr:HCl (10:1) for 4 mins, final HBr rinse.
3. Native oxide germanium sample (reference).

These samples were then sulphur passivated using a standard ammonium sulphide treatment. The samples were then loaded simultaneously into the ALD reactor and ~ 1 nm of Al_2O_3 was deposited (9 cycles of TMA and water precursors) at a substrate temperature of

250°C. Following this ALD growth, these samples were exposed to high pressure oxygen (8 Torr) at 375°C for 10 minutes in the ALD reactor before the subsequent growth of 9 nm of Al_2O_3 without air exposure. MOS capacitor structures were fabricated by the thermal deposition of ~ 100 nm of Al through a shadow mask of diameter 355 µm and a similar thickness of Al was deposited as a back contact. The process flow diagram shown in figure 6.9 schematically illustrates the fabrication steps from initial stage of surface preparations to metallization of the devices.

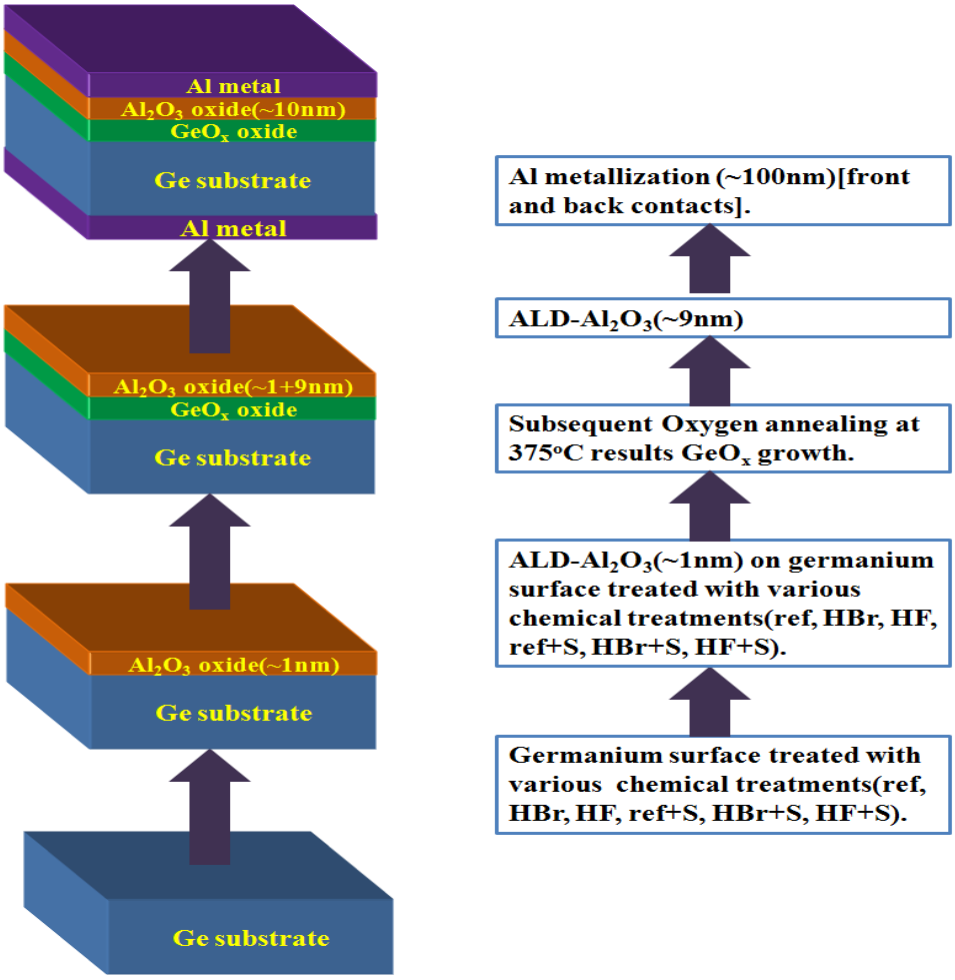

Figure 6.9: Schematic representation of sample preparations.

Figure 6.10 shows the Ge 3d XPS spectra for the post oxygen annealed Al_2O_3/Ge samples with and without sulphur treatments. The sulphur treated germanium samples were curve fitted with bulk and germanium oxide ($GeO_x(S)$) component, with the sulphur inside the bracket indicating the presence of sulphur on germanium surface whereas for the other

samples the peaks were fitted with bulk peak and a single germanium oxide component. The binding energy difference of ~ 2.5 eV between the substrate Ge signal and the germanium oxide component for each treatment is indicative of the formation of a GeO_x interfacial layer where x<2 (references of chemical shifts of different Ge oxides).

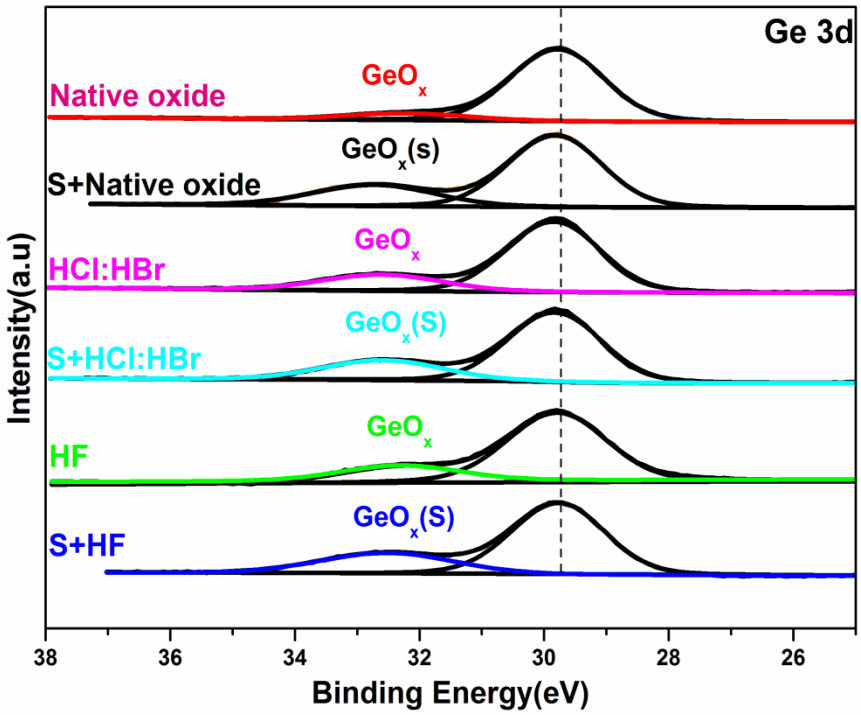

Figure 6.10: Ge 3d spectra for variety of chemically treated surface before Al_2O_3 deposition followed by oxygen annealing.

The thickness of these interlayer oxide component can be calculated using equation 1[17].

$$x = \lambda_f \cos\theta \ln\left(1 + \frac{1}{Q}\right) \qquad 6.1$$

Where $Q = \left(\frac{I_{s,x}}{I_{f,x}}\right) \times \left(\frac{I_{f,\infty}}{I_{s,o}}\right)$,$\theta$ is the emission angle and λ_f is the attenuation constant. In order to estimate the thickness x, the intensities of substrate to thin oxide photoemission peak

$\left(\frac{I_{s,x}}{I_{f,x}}\right)$ and the absolute photoemission peak intensities of the substrate (atomically clean surface) to oxide (infinitely thick layer) $\left(\frac{I_{f,\infty}}{I_{s,o}}\right)$ has to be known. By taking the ratio of $\left(\frac{I_{s,x}}{I_{f,x}}\right)$ for two photoemission peaks i.e. Ge 3d and Ge 2p, the common absolute intensities will cancel out. The overall general observation is that the thickness of the interfacial GeO_x oxide layer (~ 2 nm) which forms is effectively independent of the different surface preparations with the exception of the untreated native oxide sample what has a thinner oxide layer. This range of interlayer thicknesses have been reported to exhibit low D_{it} for the post plasma oxidation germanium samples with an Al_2O_3 dielectric [15, 16]. Houssa et al. studied the GeO_2 and GeO_x species, and reported that while a higher concentration of lower oxidation states exists for thinner GeO_2 layers, this might not result in defects in the band gap [22]. They also suggested that good electrical properties could be expected from thin GeO_x layers formed by the post oxygen annealing treatments. The electrical properties for these structures were studied using CV and GV measurements. Figure 6.11 (a) shows normalized 1 MHz bi-directional CV profiles for the untreated and sulphur passivated samples.

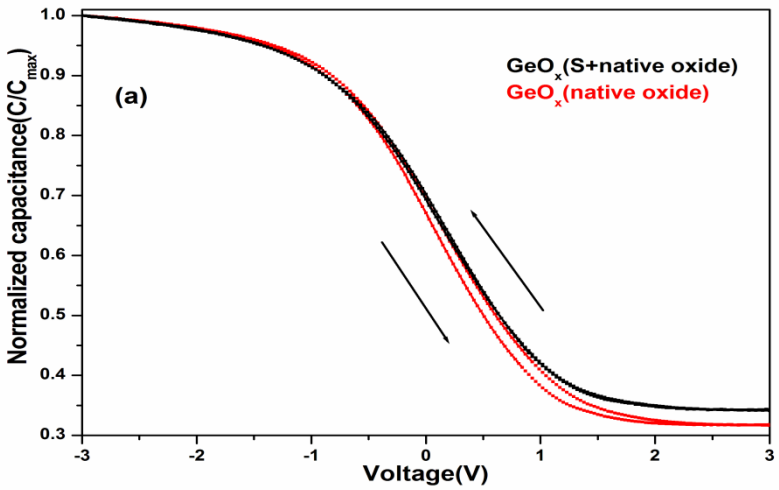

Figure 6.11: (a) 1 MHz bidirectional CV sweep for GeO_x (native oxide) and GeO_x (S+Native oxide) samples.

The charge trapping sites present at the dielectric layer results in hysteresis during the bidirectional CV sweeps. Hysteresis of 90 mV was observed for the native oxide sample which reduced to 20 mV following sulphur passivation. The density of slow traps can be estimated using the equation 6.2.

$$N_{st} = \frac{C_{ox}\,\Delta V_{fb}}{q} \qquad 6.2$$

Where C_{ox} is the oxide capacitance, ΔV_{fb} is the hysteresis voltage offset at the flat band capacitance, and q is the electron charge. The density of slow traps calculated for the native oxide surface as 2.4×10^{11} cm^{-2} decreased to 3.6×10^{10} cm^{-2} with the presence of sulphur. The fixed oxide charges present in the bulk dielectric and near to the dielectric semiconductor interface can be extracted from the equation 3.

$$N_{fixed} = (-V_{fb} + W_{ms})\frac{C_{ox}}{q} \qquad 6.3$$

Where V_{fb} is the flat-band voltage calculated from the experimental and theoretical CVs, Wms is the work function difference between semiconductor and metal, C_{ox} is the oxide capacitance and q is the electron charge. Recent theoretical and experimental studies on the origin of fixed oxide charge at the Al_2O_3/III-V interface suggest that Al and O dangling bonds play a major role [23]. The negative fixed charge density of 3.5×10^{12} cm^{-2} for native oxide sample slightly reduced to 2.3×10^{12} cm^{-2} following sulphur treatment. Weber et al [24] reported that O dangling bond states were present below the Fermi level and nearer to the Al_2O_3 valence band edge and Al dangling bond states were present above the Fermi level and nearer to the Al_2O_3 conduction band edge using first-principles calculation studies. This suggests that O and Al dangling bond states will be negatively and positively charged in the Al_2O_3 dielectric film. Both samples exhibited negative fixed charge density attributed to excess oxygen at the dielectric semiconductor interface caused by the oxygen treatment on the Al_2O_3/Ge structures. The density of interface states was ~ 8×10^{11} cm^{-2}/eV for both

samples as estimated using the conductance method. Figure 6.11(b) shows 1MHz bi-directional CV sweep for GeO_x (HF) layer on the HF treated sample and GeO_x (HF+S) layer on the sulphur passivation sample.

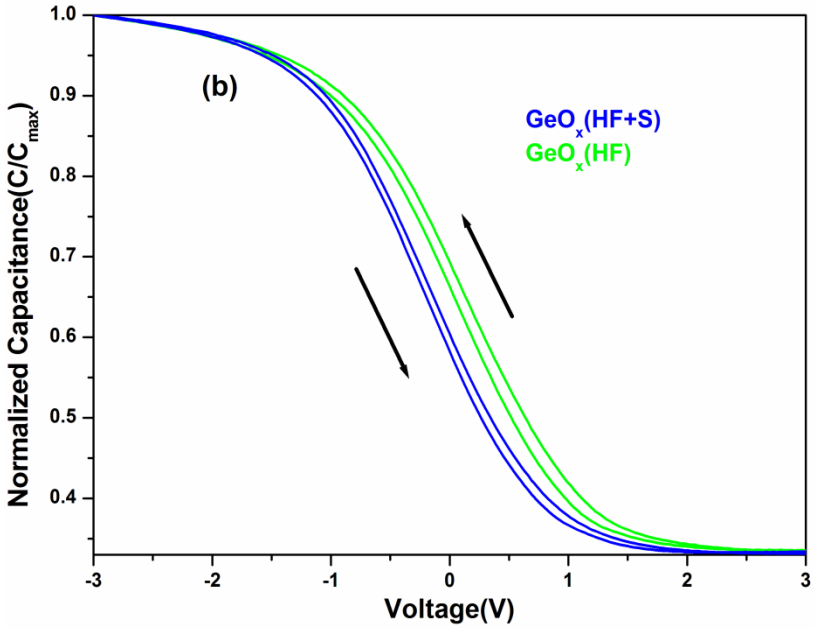

Figure 6.11: (b) 1 MHz bi-directional CV curve for the GeO_x (HF) and GeO_x (S+ HF) samples.

The hysteresis of 90mv for the GeO_x (HF) interlayer sample was reduced to 60mv for the GeO_x (HF+S) layer grown on the sulphur passivated surface. Hysteresis has been observed for both samples implying the presence of slow traps. The density of slow traps was estimated as 1.8×10^{11} cm^{-2} for GeO_x (HF) sample which only slightly reduced to 1.2×10^{11} cm^{-2} for the GeO_x (HF+S) sample. Similarly negative fixed charge density (2.72×10^{12} cm^{-2}) and D_{it} of (8×10^{11} cm^{-2}/eV) for GeO_x sample were again slightly reduced to 2×10^{12} cm^{-2},4.5×10^{11} cm^{-2}/eV, respectively, for the GeO_x(S) sample.

Dual sweep 1 MHz normalized CV profiles shown in figure 6.11(c) for GeO_x (HCl:HBr) layer and GeO_x (HCl:HBr+S) display no significant change in either hysteresis (< 90 mv) or trapped charge density (2.4×10^{11} cm^{-2}).

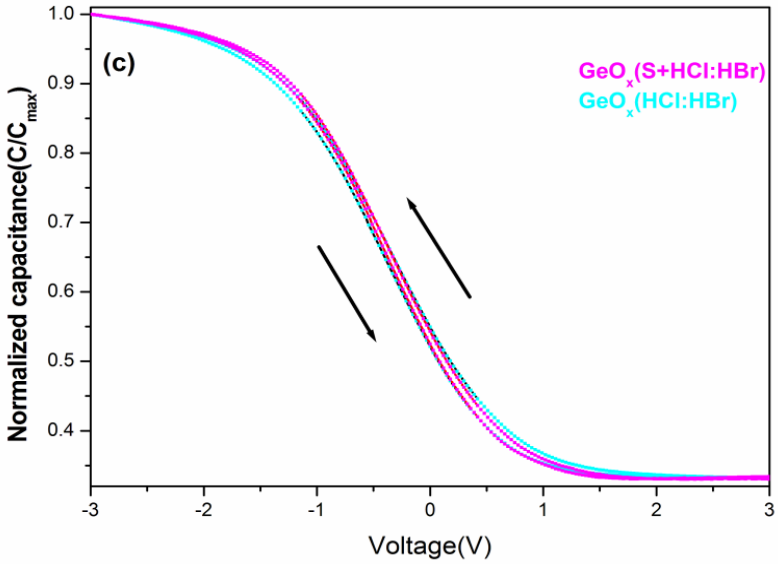

Figure 6.11: (c) 1 MHz bi-directional CV profile for the GeO_x (HCl:HBr) and GeO_x (S+ HCl:HBr) samples.

The negative fixed charge density of 2.2×10^{12} cm^{-2} for GeO_x (HCl:HBr) reduced to 1.7×10^{12} cm^{-2} for the GeO_x (HCl:HBr+S) sample and a similar trend was also seen in the extracted D_{it} as 4.5×10^{11} cm^{-2}/eV GeO_x (HCl:HBr+S) sample and 7.7×10^{11} cm^{-2}/eV for GeO_x (HCl:HBr) again suggest sulphur passivation reduces interfacial defect state densities.

6.4 Conclusion

Investigation of sulphur passivation on germanium surface results in the removal of the native oxides and the reduction of D_{it}. The sulphur passivation achieved by diluting ammonium sulphide in various alcohols shows an increase in sulphur coverage of germanium surfaces which were reflected in increased capacitance in the CV measurements. The post deposition oxygen annealing of sulphur passivated samples results in interfacial GeO_x(s) formation which was investigated by XPS measurements. These interfacial layers result in a

general trend causing a reduction in the negative fixed charge density and the density of interface states for sulphur passivated surfaces compared with unpassivated surfaces.

6.5 References

[1]. M. Houssa, G. Pourtois, M. Caymax, M. Meuris, M. M. Heyns, Surface Science 602, L25-L28 (2008).

[2]. Y. Kamata, Materials Today 11, 30-38 (2008).

[3]. N. Lu, W. Bai, A. Ramirez, C. Mouli, A. Ritenour, M. L. Lee, D. Antoniadis, D. L. Kwong, Applied Physics Letters 87, 051922 (2005).

[4]. C. Chao-Ching, C.Chao-Hsin, L.Guang-Li, L.Jun-Cheng, K.Chi-Chung, L.Da-Ren, H.Chien-Nan, Y.Chun-Hui, C.Chun-Yen, Journal of The Electrochemical Society 155, G203-G208 (2008).

[5]. M.M. Frank, S. J. Koester, M. Copel, J.A. Ott, V. K. Paruchuri, H. Shang and R. Loesing Appl.Phys .Letts.89, 112905 (2006).

[6]. A. Delabie, D. P. Brunco, T. Conard,P. Favia, H. Bender, A. Franquet, S. Sioncke, W. Vandervorst, S. V. Elshocht, M. Heyns, M. Meuris, E. Kim, P. C. McIntyre, K. C. Saraswat, J. M. LeBeau, J. Cagnon, S. Stemmer, W. Tsaie, Journal of The ElectrochemicalSociety,155(12)H937-H944(2008).

[7]. S. Sun, Y. Sun, Z. Liu, D.-I.Lee, P. Pianetta, Appl. Phys. Lett, 89, 231925 (2006).

[8]. H. Seo, K. B. Chung, J. P. Long, G. Lucovsky, Journal of The Electrochemical Society, 156(11)H813-H817(2009).

[9]. R.K. Chellappan, D.R. Gajulo, D.W. McNeil, G. Hughes (submitted Applied surface science).

[10]. V.N Bessolovy, M.V. Lebedevy, N. MinhBinhz, M. Friedrich, D.R.T. Zahn Semicond. Sci. Technol. 13,611–614(1998).

[11]. C. H. Lee, T. Tabata, T. Nishimura, K. Nagashio, K. Kita, and A. Toriumi, Appl. Phys. Express, 2, 071404 (2009).

[12]. N. Wu, Q. Zhang, C. Zhu, D.S.H. Chan, A. Du, N. Balasubramanian, M. F. Li, J. Sin and D.L Kwong, IEEE Electron Device Lett. 25 631(2004).

[13]. T. Maeda, T. Yasuda, M. Nishizawa and S. Takagi Appl. Phys. Lett. 85 3181(2004)

[14]. N. Wu, Q. Zhang, C. Zhu, C. C. Yeo, S. J. Whang, D. S. H. Chan, M. F. Li and B. J. Cho Appl. Phys. Lett. 84, 3741 (2004).

[15]. R. Zhang, T. Iwasaki, N. Taoka, M. Takenaka, and S. Takagi, Appl. Phys. Lett. 98, 112902 (2011).

[16]. R. Zhang, T. Iwasaki, N. Taoka, M. Takenaka, and S. Takagi IEEE Trans. Electron Devices 59, 335 (2012).

[17]. S.N.A. Murad, P. T. Baine, D. W. McNeill, S. J. N. Mitchell, B. M. Armstrong, M. Modreanu, G. Hughes, R. K. Chellappan. Solid-State Electronics Volume 78, Pages136–140 (2012).

[18]. Y. Nakakita, R. Nakane, T. Sasada, H. Matsubara, M. Takenaka, and S. Takagi, IEDM Tech. Dig, pp. 877–880 (2008).

[19]. K. Prabhakaran, F. Maeda, Y. Watanabe, and T. Ogino: Appl. Phys.Lett. 76, 2244 (2000).

[20]. K. Kita, S. Suzuki, H. Nomura, T. Takahashi, T. Nishimura, and A. Toriumi, Jpn J. Appl. Phys. 47,pp. 2349–2353, (2008).

[21]. M. Caymax, G. Eneman, F. Bellenger, C. Merckling, A. Delabie, G. Wang, R. Loo, E. Simoen, J. Mitard, B. De Jaeger, G. Hellings, K. De Meyer, M. Meuris, M. Heyns, IEEE International Electron Devices Meeting (IEDM), 461 (2009).

[22]. M. Houssa, G. Pourtois, M. Caymax, M. Meuris, M. M. Heyns, V. V. Afanas'ev, A. Stesmans, Appl. Phys. Lett, 93, 161909 (2008).

[23]. B.Shin, J. R. Weber, R. D. Long, P. K. Hurley, C. G. V. Walle, P. C. McIntyre. Appl. Phys. Lett. 96, 152908 (2010).

[24]. J. R. Weber, A. Janotti, and C. G. Van de Walle, Microelectron. Eng. 86, 1756 (2009)

7 Conclusions and Future work

7.1 Conclusions

The objective of this study was to find a compatible method to limit or prevent interfacial oxide growth on both high mobility Ge and InAs substrates prior to or during high-κ deposition, in view of simplifying the fabrication process of future CMOS devices.

MgO deposition on atomically clean germanium surface resulted in interface oxide formation whereas no oxidation states were observed for the selenium treated germanium surface indicating the effectiveness of this interlayer at producing an abrupt MgO/Ge (100) interface. However the same selenium passivation on InAs surface was not successful at preventing interfacial oxide growth.

A comparison study of thermal annealing and atomic hydrogen cleaning of native oxide covered InAs surfaces was investigated. Annealing native oxide InAs surface up to 450^{o}C showed a reduction in the intensity of the In and As oxides, however this anneal was not sufficient to produce an oxide and carbon free surface. Exposure to a beam of atomic hydrogen at 360^{o}C resulted in the removal of both native oxides and surface carbon contamination producing a clean In rich surface.

A systematic approach to prepare oxide free dielectric-semiconductor interfaces was also studied. High temperature post deposition annealing treatment of high-κ materials deposited on germanium and InAs substrates resulted substantial reduction of interfacial oxides without affecting the stoichiometry of the dielectric materials. Energy band offsets were also estimated for these structures using photoemission measurements.

The electrical and chemical properties of sulphur passivated germanium surfaces with various pre-cleaning chemical solutions were studied by fabricating Ge based MOS capacitors. The tunning of electrical and chemical characteristics on MOS capacitors was achieved by alcohol based sulphur passivation. The post deposition oxygen annealing treatment of Ge MOS

stacks prepared using various chemical treatments showed an improvement in the electrical properties.

7.2 Future work

Suggested extensions of this thesis are proposed below.

- Optimization of wet chemical selenous acid based selenium passivation on both germanium and InAs surfaces. Fabrication of MOS capacitor using the optimized selenium passivation method would help to understand the electrical and chemical impact of selenium passivation.

- Argon ion bombardment followed by annealing is the common method to prepare atomically clean germanium surface. However this treatment could induce damage on the surfaces. The atomic hydrogen cleaning of InAs surface was demonstrated in this thesis thus repeating the same treatment on germanium could produce oxide and carbon free surface.

- The presence of oxide contaminants on InAs surfaces are reported to have a greater influence on Fermi level pinning behaviour. The removal of these contaminants using atomic hydrogen treatment is shown in this study. Studying the electrical properties of InAs MOS caps prepared using this surface treatment would help to understand the relation between surface contaminants and the Fermi level pinning mechanism.

- In-situ selenium passivation of InAs surface was not successful at preventing interfacial oxide whereas for the germanium surface this passivation was successfully prevented the surface from oxidation. Repeating the experiment on both surfaces with sulphur passivation instead of selenium would help determine whether the elements from same group (VI) has similar chemical properties.

- Alcohol based sulphur passivation on germanium surfaces resulted in an increase of sulphur coverage as a function of dielectric constant of alcohols. The similar experiment could be repeated on InAs surfaces to test the consistency of the variation of sulphur coverage with alcohol dielectric constant.